Internet of Underwater Things: Enabling Technologies of Underwater Communications and Hybrid Networking

by

Debing Wei

A dissertation submitted to the Department of Electrical and Computer Engineering,

Cullen College of Engineering

in partial fulfillment of the requirements for the degree of

Doctor of Philosophy

in Electrical and Computer Engineering

Chair of Committee: Miao Pan

Committee Member: Aaron T. Becker

Committee Member: Aijun Song

Committee Member: Gangbing Song

Committee Member: Jiefu Chen

University of Houston

May 2021

ACKNOWLEDGMENTS

This work would not have been accomplished, without the collaboration of many individuals.

I am first indebted to my thesis supervisor, Prof. Miao Pan, who supported my work and provided superior intellectual challenges. This work would not have been accomplished without his support, without the energy that he dedicated, both as a mentor and as a friend.

I am grateful to my friends as well as collaborators from UH, especially to Chaoxian Qi, Li Yan, and Chengpei Huang. We spend a lot of time together on the discussions and experiments for our underwater projects. Without their help, it won't be easy for me to complete this work.

I also feel that I owe a big thank you to the administrative staff of the ECE department, and especially to Kelly King.

To my parents and sisters I owe the most. This work would not have been possible without their continuous support and love. This thesis is dedicated to them, who have been the main source of my strength throughout this challenging period of my life.

ABSTRACT

The Internet of Underwater Things (IoUT) is an ideal intelligent approach for ocean exploration in the new era of IoT, which mainly relies on underwater acoustic communications (UAC) for the interconnections among underwater devices. However, two inherent drawbacks of UAC make it insufficient for some communication requirements. First, it cannot support latency-sensitive applications such as accurate synchronization due to the long propagation delay. The second one is the limited bandwidth available for long-range communications. To find an alternative communication solution, two different underwater communication paradigms are investigated in this dissertation, namely underwater magnetic induction (MI) wireless communications and stress wave communications. For the MI alternative that does not have latency issues, we focus on the integration of MI technology with autonomous underwater vehicles (AUVs). A ferrite-assisted geometry-conformal MI antenna was proposed to fit for AUVs with a metallic body that maintains their fluid-dynamic efficiency. A concise physical layer was designed for the robust MI channel. For long-range underwater communications, we turn to stress waves using offshore pipelines for a possible solution. The established stress wave channel model reveals that the frequency-dependent attenuation can be ignored, which tells us the available bandwidth will not be affected by the communication range. Zero-forcing equalization and OFDM modulation were utilized to tackle the dispersion and reverberation interference under different circumstances. An underwater wireless communication testbed was established based on software-defined radio (SDR) and universal software radio peripheral (USRP) to verify the communication feasibility of both the MI and the stress wave. Finally, a power-efficient underwater AUV data collection strategy was designed, which can significantly prolong the network lifetime by using hybrid networking with both underwater acoustic and MI wireless communications.

TABLE OF CONTENTS

LIST OF TABLES

LIST OF FIGURES

1 Introduction

Oceans cover more than 70% of the earth surface, provide valuable resources (*e.g.*, crude oil, natural gas, and various minerals such as manganese, copper, nickel, iron, cobalt), generate oxygen, absorb greenhouse gases, keep climate change in check, determine weather patterns and temperatures, and serve as highways for sea-borne international trade. The quantity of organisms that live in oceans far exceeds those that habitat the land. By 2030, the value of the global ocean-based economy is estimated between USD 3-6 trillion per year [72]. Surprisingly, we actually know less about the ocean than some extra terrestrial bodies. For example, we have mapped the entire Martian surface, while we have explored less than 10% ocean floor, underneath which billions of dollars of natural resources are "sleeping". The Hubble telescope allows us to see up to 13 billion light years away, while acoustic seismic sensors anchored on the ocean floor cannot reliably transmit their collected information back to the ocean surface several kilometers away.

To facilitate the ocean exploration, the concept of Internet of Things (IoT) has been extended to ocean bodies, which leads to the idea of Internet of Underwater Things (IoUT). IoUT was first introduced in 2012 [23]. It is defined as a world-wide network of smart interconnected underwater objects with a digital entity. The interconnected objects include various types of sensors, buoys, autonomous underwater vehicles (AUVs), autonomous surface vehicles (ASVs), and offshore infrastructures, *etc.* The major components of an IoUT system are shown in Fig. 1.

1.1 Essential components in IoUT

1.1.1 Underwater Sensor Network

Obviously, sensors are the most essential components, since the key objective of IoUT is to bring sensing data to the surface. To explore the ocean, different types of sensors [115] may be deployed in the underwater environments, which may include conductivity–temperature–depth system (CTD), acoustic Doppler current profilers (ADCPs), oxygen

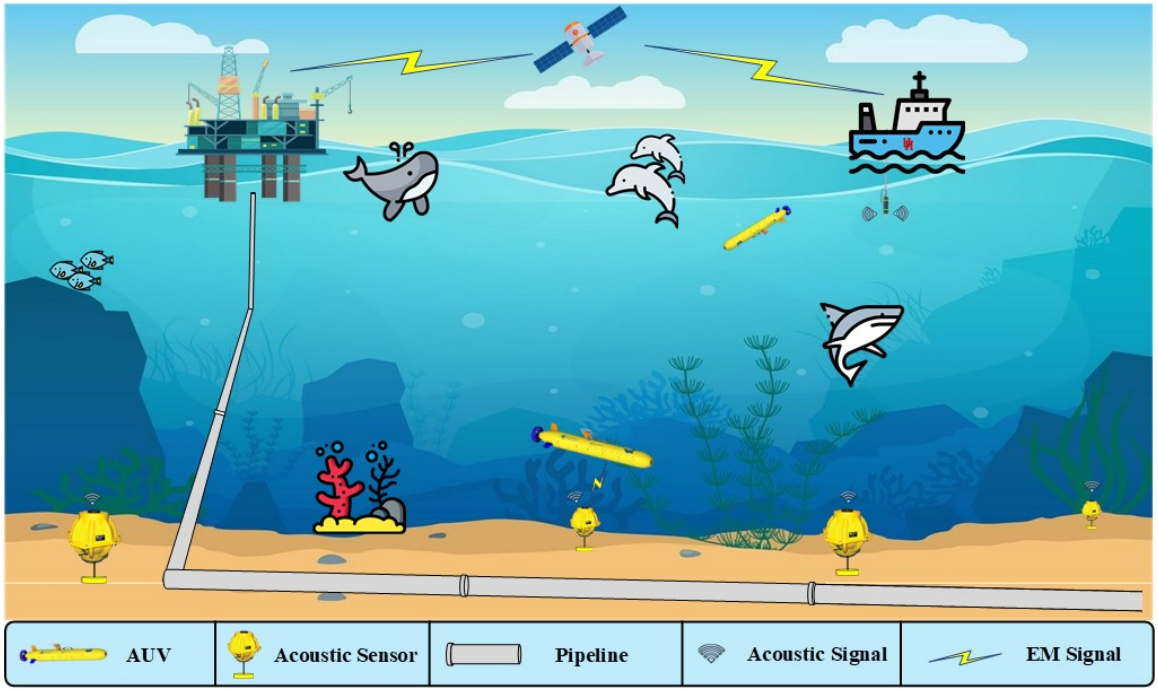

Figure 1: Overview of IoUT.

content detectors (OCD), ammonia nitrogen detectors (AND), phosphorus content detectors (PCD), *etc.* The wireless interconnection of these sensors form a underwater wireless sensor network (UWSN). In UWSNs, sensors, also known as nodes, can not only sense environments, such as the water quality, pressure, temperature, metal, and chemical and biological elements, but also relay and forward data. The sensing data need to be transferred to the essential components on the surface, known as sink(s) which can be buoys, ships, or ASVs. Typically, UWSNs forward data to the sinks through acoustic channels. Sinks will forward the data to the onshore monitoring center through radio channels.

1.1.2 AUV

AUVs are unmanned, self-propelled vehicles typically deployed from a surface vessel, and can operate independently of that vessel for periods of a few hours to several days [111]. Most are torpedo-shaped, but some have a more complex configuration allowing them to move more slowly and across complex terrain. AUVs are capable of carrying a variety of

sensor payloads. Since AUVs can follow a pre-programmed course through the water, they are well suited for seabed mapping and subbottom profiling [66].

Depending on their pressure resistance, existing AUVs can operate in water depths of up to 6000 m [111]. The typical moving speed is around 2 m/s [18]. Since AUVs can easily get access to the underwater sensor nodes, they can be introduced into UWSNs as data mules to collect the data from sensor nodes [117, 38, 52, 51, 27, 120]. With the assistance of AUVs, the lifetime of UWSNs can be significantly extended [106], since sensor nodes do not need to transmit data via power hungry long acoustic links.

1.1.3 Offshore Pipelines

Offshore pipelines are considered to be the most efficient and effective modes of transport for carbon products [35]. Owing to the escalating demand for oil and gas, thousands of miles of offshore pipelines have been deployed all over the world. Taking the Gulf of Mexico as an example, over 44,000 miles of pipelines have been deployed during the last century [47]. The State of the Coast website boasts of the US National Oceanic and Atmospheric Administration (NOAA), "If placed end to end, the oil and gas pipelines in the Gulf of Mexico could wrap around the Earth's equator.". The lifespan of the offshore pipeline is around 40 years. However, a large portion of offshore pipelines is out of service. For example, there are more than 18,000 miles of "out of service" pipelines in the Gulf of Mexico [47].

Inadequate monitoring and maintenance of this critical infrastructure may lead to ruinous economic loss and environmental disasters. Take BP's "Deepwater Horizon" incident as an example. In this event, damaged subsea infrastructure leaked more than 200 million gallons of oil into the Gulf. Eleven workers died, and 17 were injured. Penn State University further reported the deaths of 6,104 birds, 609 sea turtles, and 100 marine mammals. More than 1,000 miles of shoreline were fouled. Furthermore, as part of the process of breaking up the spill with chemical dispersants, more than 2 million gallons of toxic chemicals were sprayed into the Gulf. The long-term impacts of these dispersants on marine wildlife have yet to be determined. Unfortunately, BP's "Deepwater Horizon" was only one

of thousands of oil accidents in the Gulf of Mexico as shown in Fig. 2. The severity of such

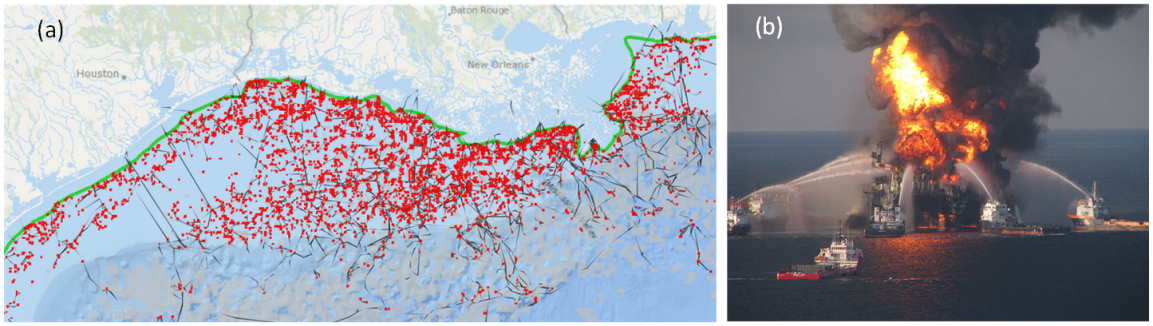

Figure 2: (a) Offshore pipeline accident in the Golf of Mexico [25]. (b) Deepwater Horizon drilling explosion in April 2010 [75].

accidents and their economic and environmental consequences highlights the need for structural health monitoring (SHM) for subsea infrastructure, in particular, offshore pipelines. Unlike onshore pipelines, offshore pipelines constantly face a harsh submarine environment containing multiple threats that increase risk of damage (*e.g.*, weld defects, corrosion pits, cracks, buckling, leakage) and undermine safe operation [35, 41, 45]. A study by DNV (Det Norske Veritas) shows that the frequency of failure for various types of offshore pipeline structures ranges from 6.8×10^{-6} to 4.5×10^{-3} per km year [21]. A recent report from the Bureau of Ocean Energy Management stated from 1964 to 2013, a total of 514 offshore pipeline-related oil spills were recorded, 20 of which involved spills greater than 1000 bbl of oil [6]. A twofold challenge that forms the bottleneck for SHM of offshore pipelines is (i) the attenuating effects of the subsea environment and (ii) the difficulty of monitored/sensed information delivery from the ocean floor to the surface without deploying massive amounts of cables.

1.2 IoUT Applications

Leveraging the collected data, IoUT can support different kinds of subsea applications which can be categorized into five different types [48] as shown in Fig. 3.

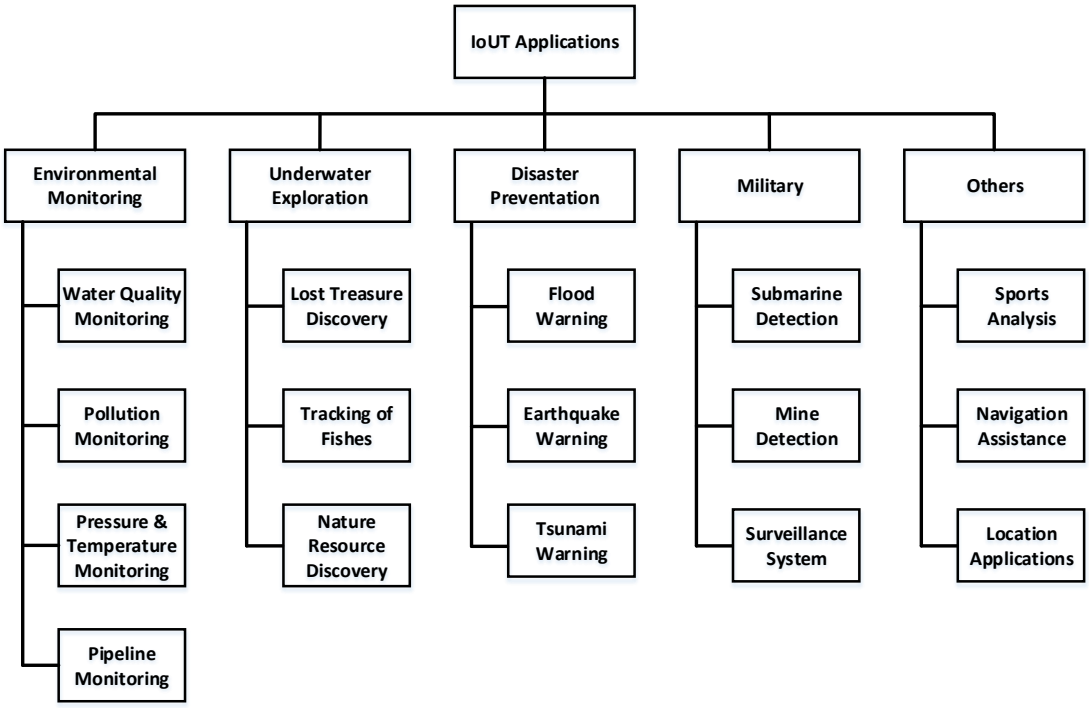

Figure 3: The IoUT applications [48].

1.2.1 Environmental Monitoring

One of the significant applications of IoUT is environmental monitoring, including water quality monitoring [69], thermal pollution monitoring, pressure monitoring, and temperature monitoring [4], chemical and biological pollution monitoring [50], *etc.* In recent years, offshore structure health monitoring [81] has become a hot topic, which can be well achieved through IoUT. Specifically, by installing wireless sensors along the pipeline, the operation conditions can be continuously monitored. The data collected by sensors is transmitted through the sensor network towards the sink, which forwards it to the onshore monitoring center. Based on the sensor data, the long term behavior can be predicted, maintenance can be scheduled accordingly and hence the pipeline remaining life can be extended.

1.2.2 Underwater Exploration

Thanks to the advancement of marine autonomous technology, AUVs have greatly facilitate our ability to explore underwater. AUVs provide opportunities for data acquisition in parts of the ocean previously inaccessible to vessel-based instruments, *e.g.*, beneath ice sheets in polar region, and improve the spacial and temporal resolutions of a broad spectrum of marine measurements. Specifically, the vessel-mounted multi-beam echo sounder (MBES) provides a regional base map with a spatial resolution of 10s to 100 s of meters, while the AUV MBES can provide detailed maps with a spacial resolution of 0.5-5 m [111].

AUVs also play a significant role in underwater lost-treasure discovery. The most famous early example is the discovery of the Titanic in 1985 [16]. Up to now, we still rely on AUVs in the search for the missing Malaysia Airlines Flight MH370 on April 14, 2014. IoUT can also be applied to fish tracking and underwater natural resource discovery, such as minerals [93], metals, and coral reefs [7].

1.2.3 Disaster Prevention

The disaster prevention applications are one of the most crucial IoUT applications. For example, the Japanese nuclear accident, Fukushima Daiichi nuclear disaster, was initiated primarily by the tsunami following the Tohoku earthquake on March 11, 2011. To provide applications for prevention of such disasters, IoUT is widely expected to detect flood [65], earthquake [54], tsunami [12] underwater, and to offer early warning services.

1.2.4 Military

The military often reflects the ability of a country to defend itself against any form of attack, including underwater attack. IoUT is required for defense purposes, and can be applied to submarine detection [64], underwater mine detection [49], and underwater surveillance systems [14]. These applications have great potential for future naval forces.

1.2.5 Others

With the advancements in UWSNs, an increasing number of IoUT applications are becoming attractive, such as sports [63], navigation [104], and localization [32] applications. Localization applications are particularly challenging yet very valuable. Specifically, in the real world, identifying the location underwater is challenging because Global Positioning System (GPS) cannot work in underwater environments. Imagine, for example, that underwater sensors could be used as location reference points, and thus could provide swimmers, divers, ships, and underwater vehicles with valuable location information.

1.3 Challenges

The most significant different between IoUT and territorial IoT is the water medium. Every underwater electrical device needs to be waterproof, and deal with high pressure if deployed in the deep ocean. The major difficulty posed by the water medium is that it makes it difficult to get access to the underwater things. Therefore, the deployment and maintenance of the IoUT is much more difficult and expensive than the territorial IoT, which also implies that the IoUT must be able to manage its own operation without human interventions. For this purpose, the IoUT must be robust, resilient, and self-sustainable.

Besides the hard accessibility, it is also extremely difficult to establish reliable connections among underwater things. Cable connections are costly and unreliable. No objects in the water are guaranteed to remain static. Any unpredictable movements or marine creature intrusions can easily break the cables. One broken electric cable has a great chance to bring down the whole network due to the conductive sea water.

However, establishing reliable wireless links among underwater things is also extremely challenging. Almost all territorial wireless communication technologies cannot work in underwater environments, including cellular communications, WiFi, Bluetooth, Zigbee, *etc.*, due to the conductive sea water. The main reason behind this is that radio frequency (RF) signals attenuate extremely fast in conductive sea water, approximately 54 dB per wavelength depending on the conductivity. Additionally, the propagation speed of EM

waves in the water is no longer light speed. The conductive sea water gradually slow down the propagation of RF signals as the operation frequency goes down. For example, the propagation speed at 100 kHz is around 500 km/s which is approximately 600 times slower than the speed of light in a vacuum. The more detailed analysis can be found in Chapter 3.

Since RF is not an option, people naturally turn into acoustics for wireless solutions. Acoustic waves do propagate well in the water medium with less attenuation than RF. The potential underwater acoustic communication range is up to thousands of kilometers. However, the available channel bandwidth becomes narrower as the transmission range goes further due to frequency-dependent attenuation. For example, the practical bandwidth is around 50 kHz at 100 m, while at 5 kHz the range increases to 10 km. Furthermore, the propagation speed of acoustic wave in the water is only around 1500 m/s. Such a low propagation speed not only results in long communication delay but also poor channel conditions, because the slow propagation speed suffers from strong Doppler-effect, and the long propagation delay ends up with severe inter symbol interference (ISI). A more detailed analysis of underwater acoustic communications is shown in Chapter 2.

Power supplying is another big challenge for underwater devices. Typically, underwater devices are more power hungry, since they need more power to fight water resistance. Also, high transmission power is required for establishing communication links to ensure coverage. While the power requirement for the operation of IoUT is huge, power sources that are available for IoUT are limited. Almost every underwater electronic equipment needs to be powered by batteries. One of the key issues with these is that batteries are difficult to replace and recharge underwater. However, most of the IoUT applications require the network components to operate for long periods (years or decades) after they are deployed, *e.g.*, environmental monitoring applications and disaster prevention applications. Therefore, power efficiency is critical for practical IoUT applications.

1.4 Thesis Outline

The contributions of this thesis can be summarized as follows: Briefly, we are looking for power efficient wireless communication solutions for IoUT. We first turn to magnetic induction (MI) for possible solutions in Chapter 3. The MI channel modeling was completed and the potential communication performances are revealed including achievable communication range, available bandwidth, and channel capacity. To evaluate the communication performances, an underwater MI wireless communication testbed was established, and several experiments were performed in the underwater environments.

In Chapter 4 we introduce a brand new underwater communication paradigm, named "stress wave communications", which utilizes acoustic wave guides along offshore pipelines to transmit information. We show that the stress wave channel is so stable that it can be regarded as a deterministic channel. Therefore, much more reliable communication performances can be achieved. Furthermore, since the stress wave only propagates along the pipeline, a secure data link can be established. We set up a stress wave communication testbed. Both lab experiments and subsea tests were performed to prove the feasibility.

Considering the advantages and disadvantages of different underwater wireless communication technologies, the combination of them might provide promising solutions to different IoUT applications. To this purpose, we propose an underwater hybrid network combing MI and acoustic communications in Chapter 5. We study the power efficient data collection strategies for AUVs in the proposed hybrid network. The optimal AUV data collection strategy is formulated as a mix integer linear programming problem. Furthermore, two algorithms are proposed to solve it. The numerical evaluation results show that the proposed AUV-assisted MI acoustic hybrid network is much more power efficient and has much longer lifetime compared to traditional Underwater Wireless Acoustic Sensor Networks (UW-ASNs).

2 State-of-the-Art of Underwater Communications

The realization of the idea of IoUT relies on the advance of underwater communications. Since only acoustic waves can travel over long distances in the water medium, underwater acoustic communications (UAC) have became the main focus of both academia researches and industry solutions in the past few decades. Therefore, the state of the art of underwater communications is determined by the development of underwater acoustic communications.

2.1 Underwater Acoustic Channel

The achievable communication performances, *e.g.*, data rate, bit error rate (BER), and communications range, are determined by the acoustic channel which is the propagation properties of acoustic waves in the water medium. The acoustic wave is actually a pressure wave, and it can potentially propagate over hundreds of kilometers depending on the operation frequencies. Higher frequency acoustic waves attenuate faster than lower frequency waves, which results in limited bandwidth available for long range underwater acoustic communications. Acoustic waves are also featured by low propagation speed, around 1500 m/s, which results in a severe Doppler effect. Also, the variable speed at different depth causes ray bending, which is the main reason of deep water multipath propagation. In shallow water, reflections from the sea surface and the bottom are the main principle mechanism of multipath formation. All these physical properties make underwater acoustic communications extremely challenging.

2.1.1 Path Loss and Bandwidth

The acoustic transmission loss contains two main components, namely geometry spreading loss and absorption loss. The geometry spreading loss is caused by the spreading of acoustic energy, which can be expressed in dB as $k \cdot 10 \log(d)$, where d is the transmission distance (km), and k is the spreading factor. It depends only on the propagation range and frequency independent. The spreading factor k is equal to 1 for omidirectional cylindrical spreading (typically for shallow water), and 2 for spherical spreading (typically for deep

water).

The absorption loss is caused by the conversion of pressure waves into heat. It can be expressed as $d \cdot \alpha(f)$, where $\alpha(f)$ is the absorption coefficient. The absorption loss is highly related to the stress wave frequency. Hence, the absorption coefficient $\alpha(f)$ (dB/km) is frequency dependent, which can be approximated by Thorp's formula [67, 77] as a function of f (kHz)

$$\alpha(f) = \frac{0.11}{1+\frac{1}{f^2}} + \frac{44}{1+\frac{4100}{f^2}} + 2.75 \times 10^{-4} f^2 + 0.003. \tag{1}$$

As shown in Fig. 4, the absorption coefficient is proportional to the operation frequency. As transmission range increases, the available bandwidth linearly decreases.

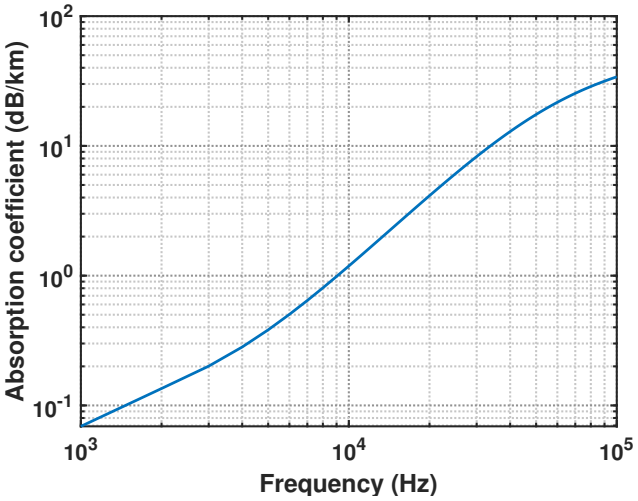

Figure 4: Thorp's absorption coefficient as a function of frequency.

Combining geometry loss and absorption loss, Urick's model of acoustic transmission loss $L(d, f)$ in dB is obtained as a function of frequency f (kHz) and transmission range d (km) as

$$10 \log L(d, f) = k \cdot 10 \log(d \times 10^3) + d \cdot \alpha(f) + A, \tag{2}$$

where A is a constant in dB called transmission anomaly representing other factors [67]. Based on the frequency dependent transmission loss, the available bandwidth for different UAC ranges were approximated as shown in Table 1.

Table 1: Available bandwidth for different UAC ranges [2, 67].

Range (km)	Bandwidth (kHz)
1000	<1
10-100	2-5
1-10	10
0.1-1	20-50
<0.1	>100

2.1.2 Multipath Fading

The multipath formation is governed by two effects. In the shallow water, it is mainly due to the reflection at the ocean surface, bottom, and any objects. In the deep water, it is mainly caused by the refraction due to the temperature, pressure, and salinity difference of the sea water at different depth. These two mechanisms are well explained in [96] as shown in Fig. 5. The underwater acoustic propagation speed can be estimated by [102]

$$1449.05+4.57T-0.0521T^2+0.00023T^3+(1.33-0.0126T+0.000009T^2)\cdot(S-35)+16.3z+0.18z^2, \tag{3}$$

where T is the temperature in ℃, S is the salinity in g/kg, and z is the depth in km. The propagation speed varies between 1450 m/s to 1540 m/s [67].

Examples of underwater acoustic channel response at different distances are shown in Fig. 6, which show that the delay spread ranges from 10ms at 1km to 60 ms at 9 km. Such a long delay spread can cause strong inter symbol interference (ISI) and make it difficult to realize reliable data transmissions.

2.1.3 Time Variability

Due to the fast variation of ocean environments, *e.g.*, rough ocean surface, the propagation paths between the transmitter and receiver will keep changing. Therefore, the underwater acoustic channel can be regarded as a fast fading channel. This can also be verified from Fig. 6 because the power of each path fluctuates. It is shown in [77, 57, 116, 101] that the pathloss or channel gain may follow the log-normal distribution, considering that each

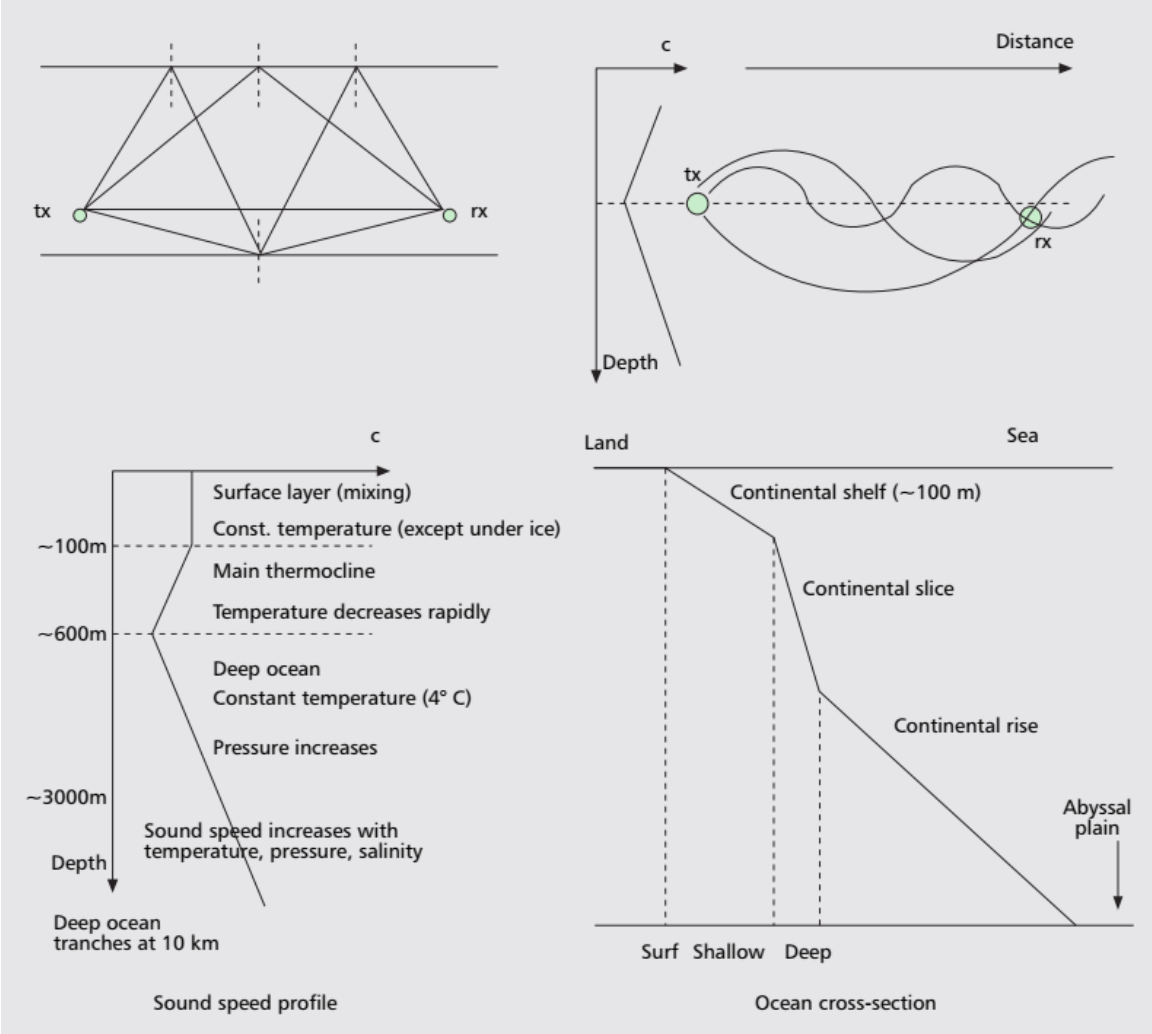

Figure 5: Multipath formation in shallow and deep water taken from [96].

path length follows the Gaussian distribution. For small scale fading caused by the rough ocean surface, experimental studies show both Rician [92] and Rayleigh [15] phenomena. The coherence time of UAC channel is on the order of 100 ms [94].

2.1.4 Doppler Effects

Due to the low propagation speed of acoustic wave (1500 m/s), the motion induced Doppler distortion could be extreme. The Doppler shift ratio is defined as $\mu = \frac{v}{c}$, where c is the acoustic wave propagation speed, and v is the relative transmitter-receiver velocity.

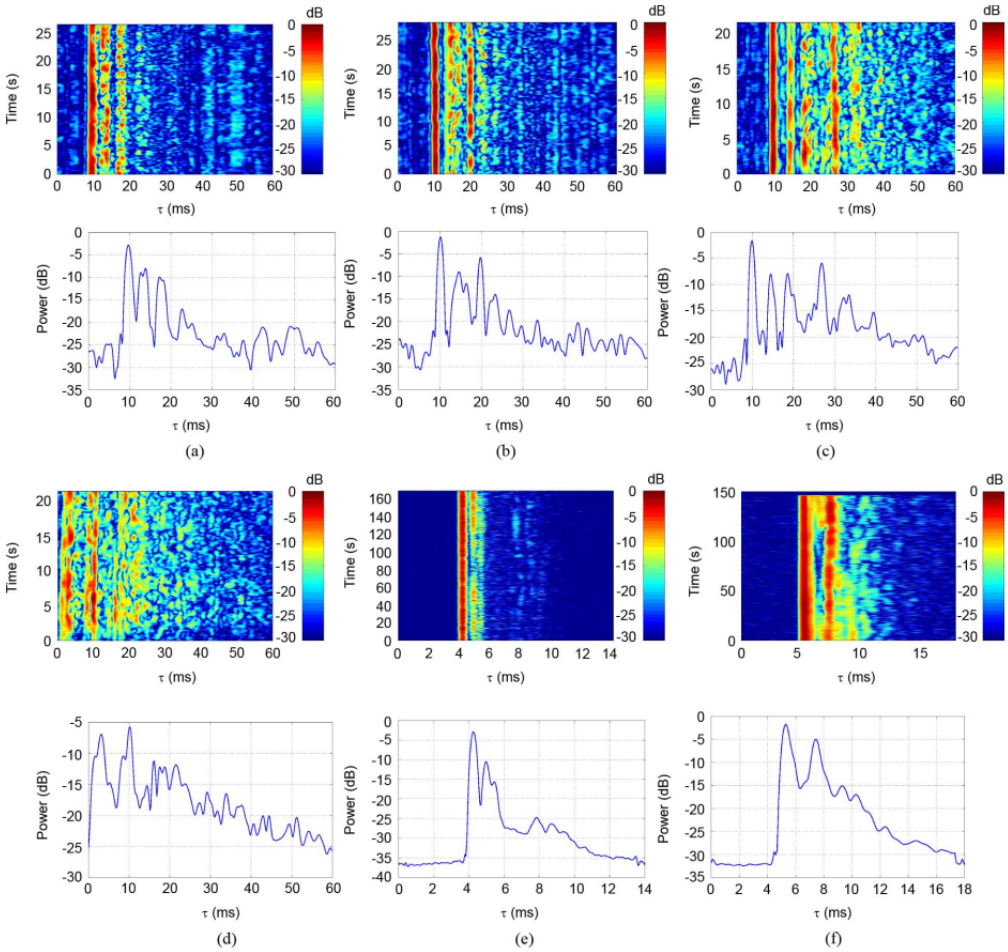

Figure 6: Examples of measured acoustic channel responses and power profiles. (a) Med. Sea: d = 1 km. (b) Med. Sea: d = 2.5 km. (c) Med. Sea: d = 5 km. (d) Med. Sea: d = 9 km. (e) Atl. Ocean: d = 1 km, f_c = 17.5 kHz. (f) Atl. Ocean: d = 2 km, f_c = 11.2 kHz taken from [92].

Considering the low propagation speed of acoustic wave, The Doppler shift ratio μ could be extremely large, in the order of 10^{-3} [94]. Such a significant Doppler effect can lead to severe inter-carrier interference (ICI) for an orthogonal-frequency-division-multiplexing (OFDM) transmission.

There are four main approaches to estimate the Doppler shift [19]. The first one is applying a bank of match filters (MFs). Each MF corresponds to a specific Doppler shift ratio. After the received symbol passes through the MFs, the one with the closest Doppler shift ratio outputs the highest energy. Obviously, the accuracy depends on the number of

MFs. However, increasing the number of MFs will also increase the complexity. Therefore, this approach may not be suitable for real-time applications. The most straightforward approach is by measuring the Doppler-frequency offset. But precisely estimating the frequency of received signal requires of high sampling rate, which increases complexity. The most commonly used approach is directly measuring the symbol duration, which can be obtained by measuring the time-difference-of-arrival (TDoA) between two received symbols. This can be achieved by detecting the cyclic prefix (CP) of an OFDM symbol through the correlation operation. TDoA can also be measured by transmitting an Doppler-insensitive preamble before the data package and a postamble after the data package [105].

2.1.5 Background Noise

There are a lot of acoustic noise sources that can contribute to the noise floor of an acoustic channel including wind, tide, ships, biological sources, *etc.* The expressions of the noise power spectrum densities (PSD) relative to frequency f (kHz) in dB re μ Pa per Hz of four different types of noises are summarized in [67] as follows:

$$10\log N_t(f) = 17 - 30\log f, \tag{4a}$$

$$10\log N_s(f) = 40 + 20(s-5) + 26\log f - 60\log(f+0.03), \tag{4b}$$

$$10\log N_w(f) = 50 + w^{1/2} + 20\log f - 40\log(f+0.4), \tag{4c}$$

and

$$10\log N_{th}(f) = -15 + 20\log f, \tag{4d}$$

where N_t, N_s, N_w, N_{th} stand for turbulence, shipping, wind, and thermal noise, respectively. In N_s, parameter s indicates the intensity of shipping activities on the surface, ranged from 0 to 1. Parameter w in N_w denotes the wind speed in m/s. The total noise PSD is

$$N(f) = N_t(f) + N_s(f) + N_w(f) + N_{th}(f). \tag{5}$$

The noise power level of different sources are shown in Fig. 7.

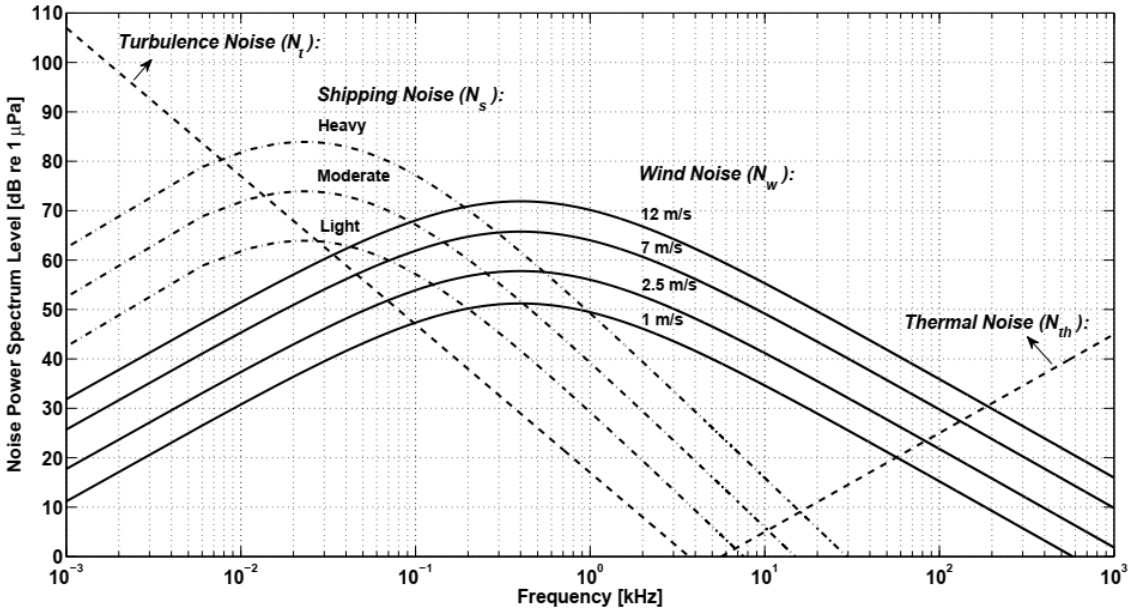

Figure 7: Underwater noise power level in dB re μ Pa per Hz taken from [67].

2.2 Underwater Acoustic Physical Layer (PHY)

Duo to the complex underwater acoustic channels featured by limited bandwidth, rapid channel variation, strong multipath, severe Doppler effects, and plenty of noise sources, it is extremely challenging to design a robust and reliable acoustic PHY layer that can support relative high transmission rate. From the perspective of PHY layer, there are two specific challenges raised by the complex acoustic channel, namely, severe ISI which may last for hundreds of symbols, and difficulty in synchronization especially for synchronizing the carrier phase.

2.2.1 Coherence and Non-coherence Modulation

The simplest way to design a reliable acoustic PHY layer is based on frequency-shift keying (FSK) and performing non-coherence FSK demodulation on the receiver side [28, 13, 82]. The advantage of this solution is that it does not require carrier synchronization,

hence it can avoid the impact of Doppler effects and rapid channel variations. However, a significant guard time interval needs to be inserted between the adjacent symbols to avoid ISI. Therefore, the bandwidth efficiency is relatively low and does not exceed 0.5 bps/Hz [94].

If the acoustic channel is relatively stable such as vertical links or short horizontal links, much more bandwidth efficient modulation schemes, such as phase-shift keying (PSK) and quadrature amplitude modulation (QAM), can be utilized to achieve high-speed data transmissions. The successful demodulation of PSK and QAM symtols relies on the recovery of the carrier phase on the receiver side, so this is also known as coherent modulation system. Different phase-shift keying (DPSK) is one of the most robust and popular choices among various PSK and QAM modulation schemes, since it encodes binaries bits into the phase difference between adjacent symbols instead of absolute fixed phase references. A 4-DPSK system capable of achieving 16 kbps over 6500 m is shown in [99].

Channel equalization must be performed to combat the ISI for coherent modulation system. Considering the long delay spread and rapid variations of acoustic channels, the adaptive decision feed-back equalizers (DFE) would be a good choice [89, 100]. Strong forward error correction (FEC) channel coding must be carried out to reduce the BER. The output of FEC can be used as a feedback to the DFE to adjust the tap coefficients. Such a idea of turbo equalization is very suitable for underwater acoustic channels [73, 88].

2.2.2 Spread Spectrum Transmission

Spread spectrum transmission has gained more and more attentions to the underwater acoustic communication community in recent years [70, 17, 86, 87]. The key property of spread spectrum signals is that they can be easily detected against the background noise, even if the signal power is lower than the noise floor. The advantages are obvious. First, it allows for low power acoustic transmission, which is good for power efficiency and significantly important for IoUT applications. Second, since signal power is lower than the noise floor, secure acoustic links can be established. Third, the low transmission power can

significantly reduce the impact to the marine mammal, *e.g.*, dolphins, therefore, it can be regarded as bio-friendly.

The linear frequency modulated (LMF), a.k.a. chirp, signal is Doppler and multipath insensitive, so it is a good spread spectrum signal candidate for robust underwater acoustic communications, which has been adopted in [70]. The LMF modulation scheme is shown in Fig. 8. In order to obtain a sufficient spreading process gain, the symbol duration cannot be very short, so the corresponding data rate is relatively low (<1 kbps).

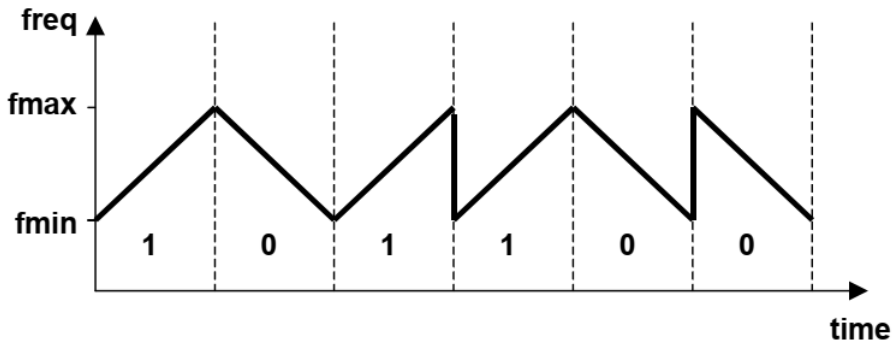

Figure 8: LFM modulation scheme [70].

2.2.3 Multi-Carrier Modulation

Long delay spread due to the multipath of the underwater acoustic channel is one of the main reasons for slow-speed data rates, since significant guard time must be inserted to mitigate the ISI. Only if the symbol duration is longer than the guard time is it possible to achieve high bandwidth efficiency. Long symbol duration implies narrow bandwidth for single carrier, therefore, only multi-carrier modulations can achieve high-speed transmission for underwater acoustic communications. The OFDM technique featured by computational efficient FFT-based processing have been widely adopted for many wireless communication systems including WiFi and 4G/LTE and 5G NR. The OFDM experiments in [95] achieved 30 kbps for 24 kHz bandwidth over the distance of 2.5 km in shallow water.

The major challenge in applying OFDM for underwater acoustic communications is

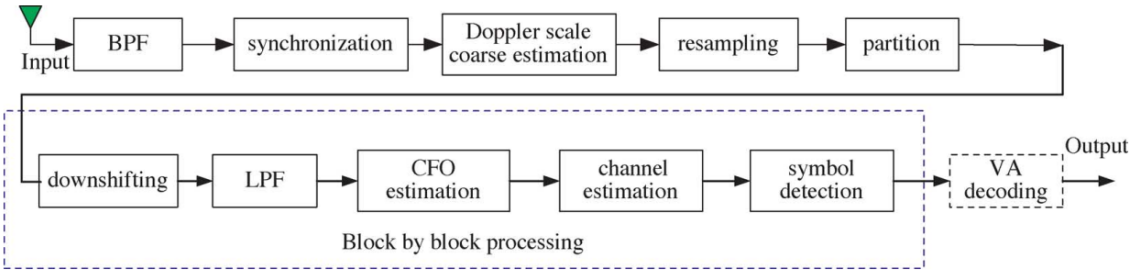

Figure 9: Underwater acoustic OFDM receiver diagram [60].

dealing with ICI caused by the severe Doppler effects. The typical block diagram of acoustic OFDM receiver is shown in Fig. 9. The coarse Doppler shift can be compensated by resampling [84, 10]. The fine Doppler shift can be compensated through carrier frequency offset (CFO ϵ) elimination between the transmitter and the receiver. The optimal CFO $\hat{\epsilon}$ can be found by minimizing the FFT output on null subcarriers as shown in [114] by

$$\hat{\epsilon} = \underset{\epsilon}{\operatorname{argmin}}\, J(\epsilon), \tag{6}$$

where $J(\epsilon)$ is the energy of the null subcarriers.

3 Underwater MI Wireless Communications

MI communication is considered to be a great alternative in harsh environments like underground and underwater [3, 97]. The main reasons behind this can be summarized as follows. First, unlike RF communications, MI technology only relies on the near field component of the magnetic field to transfer information. Since the permeability of most mediums are almost the same, MI channel conditions are much more stable in comparison to RF or acoustic channels. Second, since MI systems work under relatively low frequencies (less than 100 kHz), signal attenuation is much slower in comparison to RF signals. Third, in comparison with acoustic signals which typically propagate around 1.5 km/s, the propagation speed of MI signals is much faster (>100 times). This means that the MI communications do not suffer from latency issues and can support high accurate time synchronization for some underwater applications. Fourth, the antenna for MI system are simple wire coils, which are economic compared to the transducers needed for acoustic systems. Finally, coil antennas can be designed in many shapes and in any size, unlike RF antennas where the antenna size is determined by the operating frequencies.

MI wireless communication was first recognized by its security feature in [9] in 2004. It has been pointed out that the magnetic field of a magnetic dipole exhibits a $\frac{1}{r^3}$ dependence on distance r in the near zone. Such a strong attenuation can be utilized to create a private personal communication bubble area and permit frequency reuse. Since then, MI wireless communications have found their applications in wireless body area networks (WBANs) and the Internet of Things (IoT) [74].

André *et al.* use two self-resonant coils to light up a 60 W light-bulb wirelessly over distances in excess of 2 meters in 2007 [55]. This work not only motivates research works on magnetic resonant wireless power transfer (WPT) but also inspires people to apply MI technique for wireless communications, especially in harsh environments, i.e., underwater and underground, where the traditional RF-based wireless communications are not applicable. Theoretical MI channel models have been thoroughly studied based on its equivalent

circuit model when the MI signal propagates in the air [58], underground [97] and underwater [22, 30, 31, 108]. To summarize these works, the coupling between two coils can be equivalent to a transformer. When a voltage source is applied on the transmitter coil, the induced voltage on the receiver coil can be easily obtained by solving the equivalent transformer circuit. However, all of the aforementioned works assume that the transmitter and receiver coils are loosely coupled, which means the operational resonant frequency is the same as the self-resonant frequency of the transmitter and receiver coils.

In strongly-coupled region, where the transmitting and receiving coils are close enough, the system resonant frequency will be affected by the interaction between two coils. This phenomenon is regarded as frequency splitting [37]. Kisong *et al.* proposed a frequency-tracking scheme to compensate for frequency splitting and optimize the MI channel capacity in strongly-coupled regions [58]. However, alternating the operating frequency will complicate the overall system design. Hong *et al.* utilized frequency splitting phenomena to realize multi-channel MI wireless communication in a extremely close distance (a few centimeters) [71].

The transmission range of an MI wireless communication system with only one transmission and one receiving coil is typically within several meters, which is determined by the coil parameters such as coil size and coil quality factor. Fortunately, the MI transmission range can be extended by employing multiple relay coils between the transmitter and the receiver. These relay coils form a waveguide structure [83]. When the magnetic fields propagate through each relay coil, the field strength is enhanced. Therefore, the transmission range can be significantly enlarged by the waveguide method. However, the more relay coils employed, the more complicated the system would be. The theoretical analysis of MI waveguide based wireless sensor networks can be found in [29, 30, 98]. Nevertheless, the practical network performances require further verification. Another practical issue related to underwater MI wavegide is that it is hard to maintain a static position of a relay coil and may require intense labor work to deploy them in the underwater environments. In [109],

we leverage the mobility of AUV to realize short range underwater MI wireless communications. According to [78], the sub-meter localization accuracy can be achieved in the underwater environments. Recap that the transmission range of underwater MI wireless communication can be larger than 1 meter. Since the transmission range is no longer an issue, we do not need to apply the MI waveguide method and the overall system design can be simplified.

Field tests for underwater MI wireless communications especially in subsea environments are difficult considering the waterproofing issues and alignment issues between two loop antennas. Fortunately, we still can find some experiment results in the literature. Eugenio *et al.* measured the attenuation of EM waves generated by loop antennas at different frequencies (10 kHz to 1 MHz) and distances (2 m to 6 m) subsea [43]. Wang *et al.* demonstrated a 4-kBaud QPSK MI link in a circular seawater pool with operational frequency at 22.5 kHz and transmission distance at 0.75 m [107]. Niaz *et al.* proposed an MI transceiver design based on On-Off Keying(OOK) with data rate at 512 bps, which achieved a data transmission over 34 m both in air and underwater (freshwater) [1].

3.1 Underwater MI Channel Analysis

Fig. 10 illustrates the working principle of an MI wireless communication system with one transmitter and receiver coil. The excitation current I_t of the Tx coil was modulated by the data needed to be transmitted, which will produce a modulated magnetic field H. The corresponding magnetic flux Φ on the receiver side will induce voltage E_r in the Rx coil. The transmitted data can be recovered by demodulating the induced voltage signal E_r.

The successful demodulation of the received signal is determined by the signal to noise ratio (SNR) of E_r. The typical ambient noise power spectrum density is 140 dbm/Hz. Therefore, the maximum transmission range of an MI wireless communication system can be estimated by analyzing the attenuation of the magnetic field of a current loop a.k.a magnetic dipole in the underwater environments.

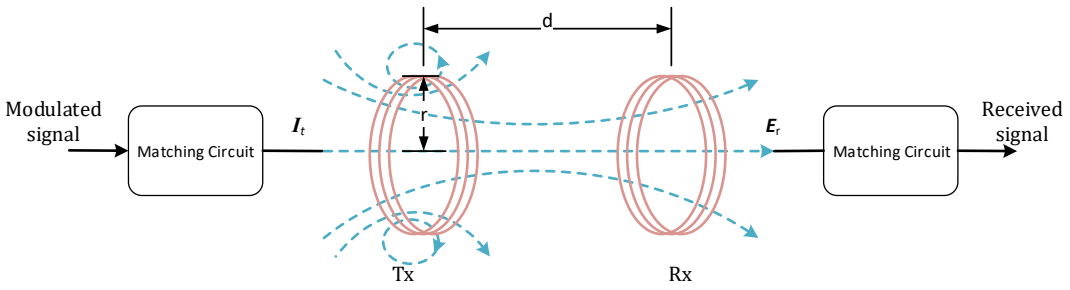

Figure 10: Working principle of an MI wireless communication system.

3.1.1 Propagation of Underwater EM Waves

The phaser expression of magnetic field components in the spherical coordinate system of a magnetic dipole with radius a are as follows [8]:

$$H_r = j\frac{ka^2 I_0 \cos\theta}{2r^2}\left[1+\frac{1}{jkr}\right]e^{-jkr}, \tag{7a}$$

$$H_\theta = -\frac{(ka)^2 I_0 \sin\theta}{4r}\left[1+\frac{1}{jkr}-\frac{1}{(kr)^2}\right]e^{-jkr}, \tag{7b}$$

$$E_\phi = \eta\frac{(ka)^2 I_0 \sin\theta}{4r}\left[1+\frac{1}{jkr}\right]e^{-jkr}, \tag{7c}$$

and

$$H_\phi = E_r = E_\theta = 0, \tag{7d}$$

where $k = \omega\sqrt{\mu\epsilon_c}$ is the wave number, $\omega = 2\pi f$ is the angular frequency, $\mu = \mu_0\mu_r$ is the medium permeability, $\eta = \sqrt{\frac{\mu}{\epsilon_c}}$ is the intrinsic impedance, $\epsilon_c = \epsilon_0\epsilon_r - j\frac{\sigma}{\omega}$ is the medium permittivity, σ is the conductivity of the medium, and I_0 is the magnitude of the excitation current.

Typically, the conductivity of sea water is $\sigma = 4$ S/m, thereby $\frac{\sigma}{\omega} \gg \epsilon_r\epsilon_0$ when the frequency of EM wave is under GHz, and sea water can be regarded as a good conductor. So the propagation constant $\gamma = jk = \alpha + j\beta$ can be approximated by $\alpha = \beta \cong \sqrt{\pi\mu f\sigma}$. The propagation attenuation coefficient can be expressed in dB as $\alpha_{dB} = 20\log_{10}(e)\alpha = 8.686\alpha$.

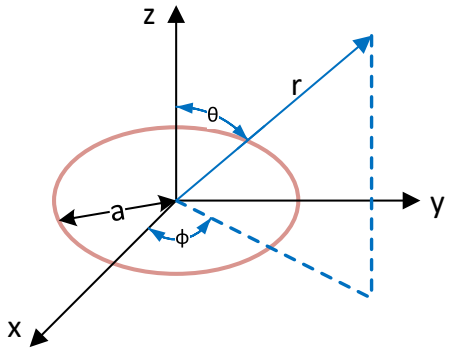

Figure 11: Geometry for circular loop.

The phase velocity of EM wave underwater is $v_p = \frac{\omega}{\beta} = \sqrt{\frac{2\omega}{\mu\sigma}}$. The dispersion curve and attenuation curve are shown in Fig. 12 and Fig. 13 respectively. The wavelength of underwater EM wave with different frequency is shown in Fig. 14.

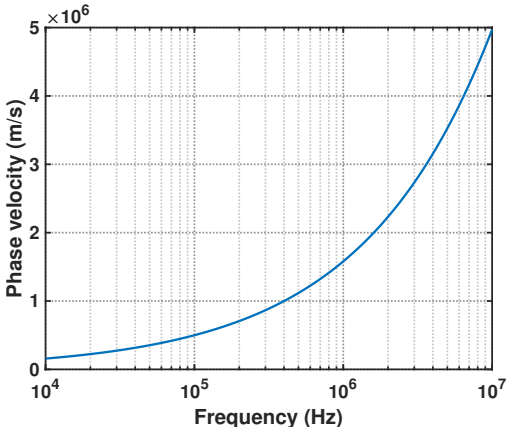

Figure 12: Propagation velocity of underwater EM wave.

Fig. 12 shows that the propagation speed of EM wave subsea is frequency dependent and much lower than the speed of light in the air. For example, the subsea EM wave with $f = 100$ kHz can only propagate at 500 km/s.

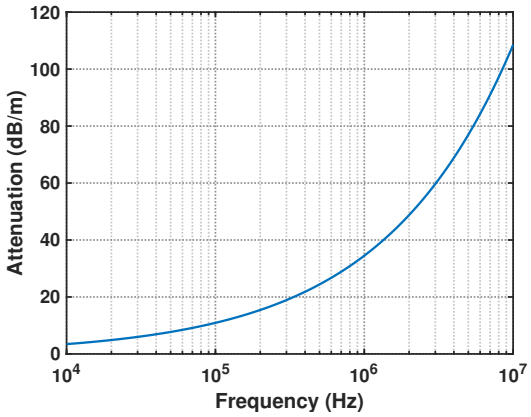

Figure 13: Attenuation of underwater EM wave.

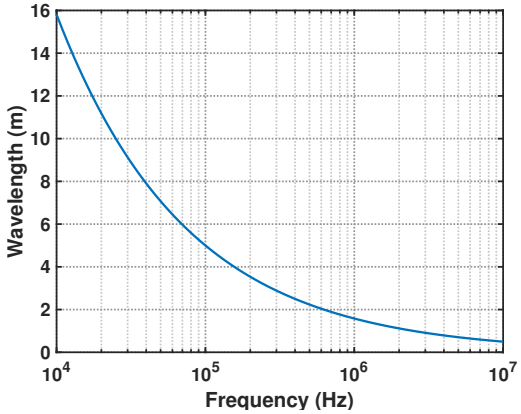

Figure 14: Wavelength of underwater EM wave.

As shown in Fig. 13, the attenuation of underwater EM wave signal is frequency dependent. The 3 dB bandwidth can be estimated by

$$W \approx \frac{3}{\frac{\mathrm{d}\alpha_{dB}}{\mathrm{d}f}} = \frac{6\sqrt{f}}{8.686\sqrt{\pi\mu\sigma}}. \tag{8}$$

The available bandwidth under different carrier frequency is shown in Fig. 15.

Caused by the medium loss, the path loss of a subsea wireless channel is greater than 54 dB/λ, which does not include the geometry spreading loss. Therefore, the practical subsea EM wireless communication can only be realized within the near field region (2λ).

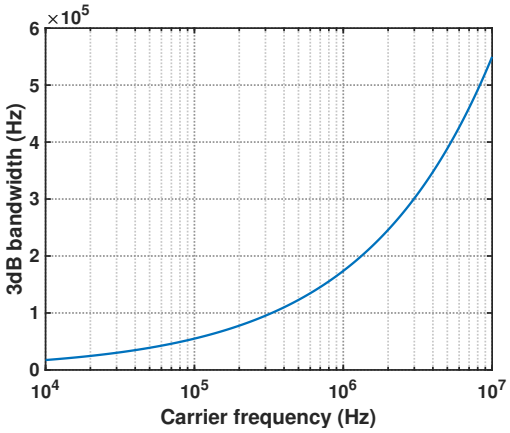

Figure 15: Available bandwidth of subsea wireless channel.

Another key feature of the EM wave subsea is that the wavelength is extremely small as shown in Fig. 14. For example, λ (@20 kHz) $\approx$ 10 m, and λ (@100 kHz) $\approx$ 5 m. Short wavelength implies that the lumped-parameter model is not accurate enough for analyzing the wireless channel between two coil antennas. Especially for the subsea MI channel modeling, the equivalent circuit model based on mutual inductance between two coils is valid only if $f < 100$ kHz, and $r < 1$ m.

The magnetic field strength of H_r, and H_θ within the range of twice wavelength are shown in Fig. 16. It shows that $H_\theta > H_r$ if $r > 0.2\lambda$. Therefore, the coplanar alignment is much better than the coaxial alignment when the communication range is larger than 0.2λ.

3.1.2 Dispersion Impacts to the Underwater Wireless Channel

From previous analysis we know that H_θ is the dominant magnetic field component that will carry the modulated information for subsea wireless communications. Duo to the dispersion of subsea EM wave as shown in Fig. 12, the subsea wireless channel works like a non-linear phase filter. The phase shift between two frequencies can be estimated by

$$\Delta\theta = \frac{2\pi}{\lambda_2}(v_1 - v_2)\frac{r}{v_1} = \beta_2 r(1 - \sqrt{\frac{f_2}{f_1}}). \tag{9}$$

The phase distortion at the range of 2λ is $\Delta\theta = 4\pi(1 - \sqrt{\frac{f_2}{f_1}})$, which is so significant

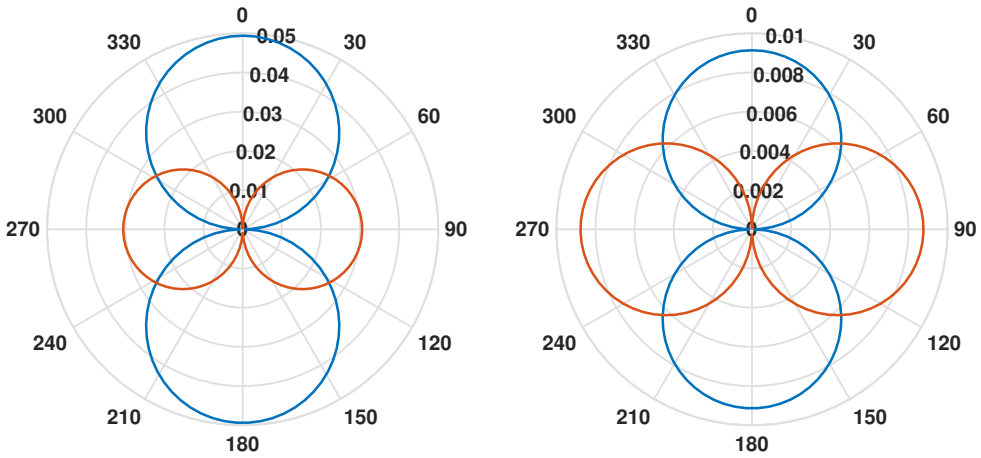

(a) r = 0.1λ (b) r = 0.2λ

(c) r = λ (d) r = 2λ

Figure 16: Magnetic field strength of a coil antenna within the range of 2λ.

that it can not be ignored. For example, the maximum phase distortion of frequency band from 80 kHz to 120 kHz is around 0.7 π. Therefore, delay equalization must be performed in the subsea EM wireless communications, which can be achieved by applying the all-pass filter as shown bellow.

3.1.3 Underwater Near-Field MI Wireless Channel Modeling

If $\beta r \ll 1$ or $r \ll \frac{\lambda}{2\pi}$, the fields within this region are regarded as near-fields. From Fig. 16(a), we know that H_r becomes the dominant field component under such conditions, which can be simplified as

$$H_r = \frac{a^2 I_0 \cos\theta}{2r^3}. \tag{10}$$

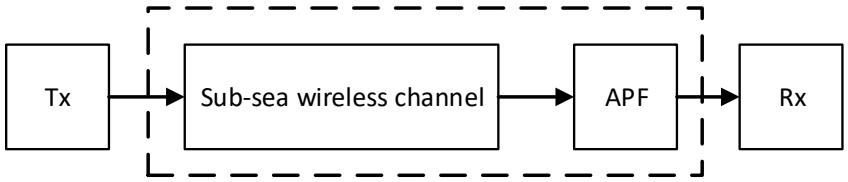

Figure 17: Delay equalization for the dispersive subsea wireless channel.

The propagation delay can be neglected, giving rise to the name of "magneto-quasistatic". Only under quasistatic conditions can we use equivalent circuit model for analyzing the near-field MI wireless channel. The radius of near-field region in subsea environments is extremely short, which is shown in Fig. 18. Theoretically, the near-field MI channel model is only valid for the spectrum under 50 kHz and transmission range within 1 m in the subsea environments. However, the near-field region for fresh water can be extend to 9 m within the spectrum under 100 kHz.

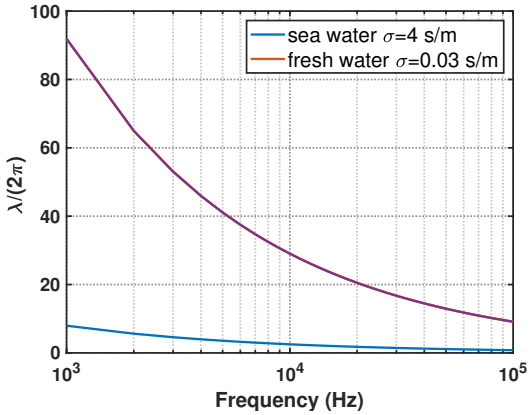

Figure 18: Radius of underwater near-field region with different frequencies.

Mutual Inductance and Coupling Coefficient. Under quasistatic conditions, the MI channel can be modeled by a mutual inductance between the Tx and Rx coils as $M = k\sqrt{L_1 L_2}$, where L represents the self inductance of coil and k is the coupling coefficient used to quantify the magnetic flux associate with the receiver. Suppose the Tx and Rx coil

are identical and co-axially aligned, then $M = kL$. The expressions for M and L are given as follows:

$$M = \frac{N_2\Phi}{I_1} = \frac{2\pi a N_1 E_\phi N_2}{-j\omega I_1} \tag{11}$$

and

$$L = \mu a N^2 \left(\ln \frac{8a}{r_w} - 2 \right). \tag{12}$$

Where r_w is the wire radius and E_ϕ is the electric field component in (7). Under quasistatic condition, $E_\phi = \frac{\eta\mu a^2 I_1 \sin\theta}{4r^2}$. After simplification, the maximum coupling coefficient between a pair of coils with coaxial alignment is

$$k = \frac{\pi a^2 \sin\theta}{2r^2 \left(\ln \frac{8a}{r_w} - 2 \right)}. \tag{13}$$

The coupling coefficient between two coils with $a = 0.1$ m is shown in Fig. 19. It shows that coupling coefficient is quite sensitive to the distance.

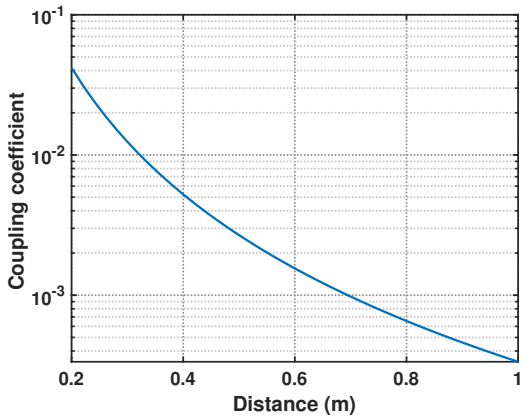

Figure 19: Maximum magnetic coupling between two coils within the near-field region.

Equivalent Circuit Model. Based on the mutual inductance model of the MI channel, the equivalent circuit model of an MI wireless communication system from the receiver point of view is shown in Fig. 20. Where v_i is the induced voltage on the receiving coil, Z_r is the total intrinsic impedance of the receiving coil, and Z_t^{refl} is the reflected impedance

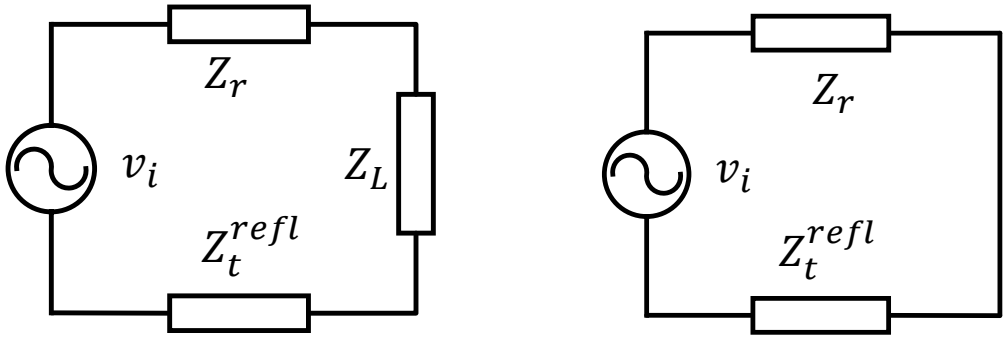

(a) Matching-Load Model (b) Free-Load Model

Figure 20: Equivalent circuit model on the receiver side.

from the transmitter side. Z_L is the introduced matching impedance.

Typically, in order to maximize the received power consumed by Z_L, the load impedance is designed to be equal to the complex conjugate of the overall output impedance on the receiving side, *i.e.*, $Z_L = (Z_t^{refl} + Z_r)^*$. However, the maximum power consumption on the receiver side may not be equivalent to the strongest received MI signals. On the contrary, such a setup may degrade the signal strength. Our first goal is to determine the optimal Z_L for the best MI communication performances.

The key idea behind the "Matching-load" model is to optimize the active power consumed by the load resistance such that the traditional path loss model can be applied. However, for a RLC resonant circuit with high quality factor, most of the energy is resonating between the inductor and the capacitor. This type of the power is the reactive power since it is not actually consumed. Very small amount of power is consumed by the resistor which is the active power. The traditional path loss model is based on the active power. Therefore, it may not be good enough to characterize the MI channel, since most the power would be the reactive power in a RLC resonant circuit.

In order to find out the best configuration of an MI receiver, let us first take a look at a typical MI front-end design on the receiver side, which is shown in Fig. 21. Three voltage signals, including resistor voltage v_R, inductor voltage v_L, and capacitor voltage v_C from the coil antenna can be selected as the input signal to the MI front-end. Obviously, we want to pick the one with the maximum amplitude as our input signal. When an RLC circuit

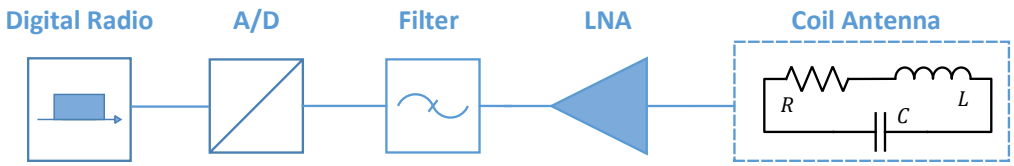

Figure 21: MI front end block diagram.

working under resonant conditions, we have the following amplitude relationship,

$$|v_C| = |v_L| = Q\,|v_R| = Q\,|v_i|\,, \tag{14}$$

where $Q = \frac{\omega L}{R}$ is the quality factor of the MI receiver and ω is the angular frequency. Equation (14) indicates that the capacitor voltage or the inductance voltage is Q times stronger than the induced voltage. Hence both of them can be selected as the MI input signal. Considering the inductor and the resistor are coupled together as a coil, the capacitor voltage would be the best choice from the circuit design point of view.

Equation (14) also suggests that the MI receiver sensitivity is determined by the receiver quality factor Q. Introducing resistors into MI receiver circuit will decrease the quality factor Q and may consequently degrade the MI system performance. If we want to maximize SNR, we need to maximize Q, which can be achieved by setting $Z_L = \Im(Z_t^{refl} + Z_r)$. Since we do not introduce any resistance into the receiving circuit, we named it as "Free-load" model.

However, high Q is not always a good thing because the available bandwidth is inverse proportional to Q. Therefore, investigating the available bandwidth of an MI system and its relationship with Q is important. Since the system bandwidth is highly related to the resonant conditions. We first analyze different resonant situations.

Resonant Analysis for an MI System. It is well known that there are two basic ways to form a resonant circuit, namely, the parallel-resonant circuit and series-resonant circuit. These two resonant circuits have different sensitivity to the frequency-splitting phenomenon when the coupling coefficient is changed.

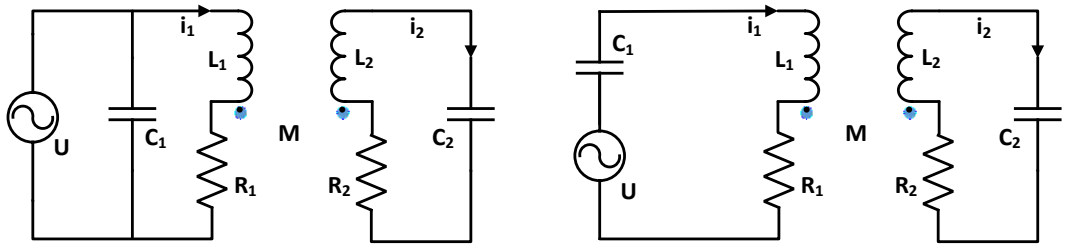

(a) Matching-Load Model (b) Free-Load Model

Figure 22: MI resonant circuit model.

Prallel-Resonant. The parallel-resonant circuit is shown in Fig. 22 (a). Based on the Kirchhoff' s Voltage Law (KVL), we can obtain the following:

$$(j\omega L_1 + R_1)I_1 - j\omega M I_2 = U \tag{15a}$$

and

$$-j\omega M I_1 + (j\omega L_2 + R_2 + \frac{1}{j\omega c_2})I_2 = 0. \tag{15b}$$

Considering $r \ll \omega L$, we can ignore the resistant component when analyzing the steady state solution of the circuit. Also, when analyzing the resonant condition we can ignore the resistant impact. Therefore, by substituting (15b) into (15a), we have

$$(j\omega\frac{L_2}{M} - j\omega\frac{M}{L_1} + \frac{R_2}{M} + \frac{1}{j\omega M C_2})I_2 = \frac{U}{L_1}. \tag{16}$$

The resonant frequency can be obtained by setting the imaginary part of (16) to zero and we get

$$(\frac{L_2}{M} - \frac{M}{L_1})MC_2 = \frac{1}{\omega^2}. \tag{17}$$

Therefore, due to the mutual coupling between the transmitter and receiver coils, the resonant frequency will be affected by the coupling coefficient k as

$$\omega = \frac{\omega_2}{\sqrt{1-k^2}}, \tag{18}$$

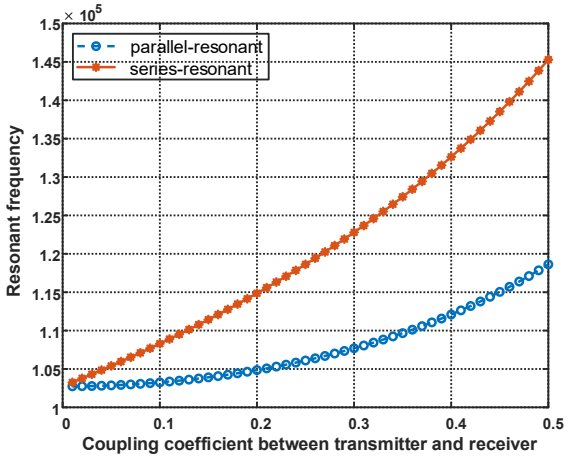

Figure 23: MI resonant frequency under different coupling conditions with $L_1 = L_2 = 400\mu H$, $R_1 = R_2 = 4\Omega$, and $C_1 = C_2 = 6nF$.

where $\omega_2 = \frac{1}{L_2 C_2}$ is the self-resonant frequency of the receiving coil. Fig. 23 reveals the resonant frequency deviation under different coupling coefficients between the transmitter and the receiver.

Series-Resonant. The series-resonant circuit is shown in Fig. 22(b), where the excitation voltage source U is in series with matched capacitor C_1 and transmitter coil L_1, R_1. The KVL equations are as follows:

$$(j\omega L_1 + \frac{1}{j\omega C_1} + R_1)I_1 + j\omega M I_2 = U \tag{19a}$$

and

$$j\omega M I_1 + (j\omega L_2 + \frac{1}{j\omega C_2} + R_2)I_2 = 0. \tag{19b}$$

If we consider the lossless situation, the following relationship should be satisfied under resonant conditions:

$$j\omega L_1 I_1 + \frac{1}{j\omega C_1} I_1 + j\omega M I_2 = 0 \tag{20a}$$

and

$$j\omega L_2 I_2 + \frac{1}{j\omega C_2} I_2 + j\omega M I_1 = 0. \tag{20b}$$

Rearranging (20) in matrix form, we have

$$\begin{bmatrix} L_1C_1 & MC_1 \\ MC_2 & L_2C_2 \end{bmatrix} \begin{bmatrix} I_1 \\ I_2 \end{bmatrix} = \frac{1}{\omega^2} \begin{bmatrix} I_1 \\ I_2 \end{bmatrix}. \tag{21}$$

By solving the eigenvalue of the coefficient matrix of (21), we obtain the resonant frequencies as

$$\omega = \frac{\omega_0}{\sqrt{1 \pm k}}, \tag{22}$$

where $\omega_0 = \frac{1}{\sqrt{L_2C_2}} = \frac{1}{\sqrt{L_1C_1}}$, which is the self-resonant frequency of the receiving and transmitting coils. The corresponding eigenvectors to each eigenvalue are

$$\begin{bmatrix} I_1 \\ I_2 \end{bmatrix} = \begin{bmatrix} 1 \\ -1 \end{bmatrix}, \begin{bmatrix} 1 \\ 1 \end{bmatrix}. \tag{23}$$

The resonant frequencies for series-resonant configuration under different coupling coefficients are also plotted in Fig. 23. It needs to be pointed out that we only plot the larger one to compare with the parallel-resonant configuration. Since in most of the situation $k < 0.1$, the resonant frequency of parallel-resonant configuration can be regarded as constant. While for series-resonant configuration the resonant frequency experiences significant fluctuation.

The frequency responses of two resonant MI system are shown in Fig. 24. The coupling coefficient will strongly affect the amplitude of the parallel-resonant system, while merely has influence to the 3 dB bandwidth. The impacts of coupling coefficient to the series-resonant system are similar to the parallel-resonant system in the loosely coupled region ($k < \frac{1}{Q}$), while significantly different from the parallel-resonant system in the strong-coupled region ($k > \frac{1}{Q}$).

The reasons can be summarized as follows:

- For parallel-resonant system, since the excitation source is in parallel with the coil, the excitation current I_1 is determined by $j\omega(L + M)$, so $\frac{\Delta I}{I} \propto k$. Therefore, the

parallel-resonant system can be regarded as the loosely coupled system.

- For series-resonant system, the excitation current I_1 is determined by $r+j\omega M$. Hence, $\frac{\Delta I}{I} \propto Qk$. When $Qk \approx 1$, the two coils are strongly coupled and the frequency-splitting phenomenon occurs.

Dynamic Bandwidth. As shown in Fig. 24, the system bandwidth in loosely-coupled region can be regarded as constant. While in strong-coupled region, the coupling coefficient k has strong impact to the available bandwidth.

3dB Bandwidth for Parallel-Resonant MI System. The parallel-resonant system can be regarded as loosely coupled system for most MI application scenarios. Considering $R \ll \omega L$ and ignore the coupling term, (15) can be safely simplified as follows:

$$j\omega L_1 I_1 = U, \tag{24a}$$

and

$$j\omega M I_1 = (j\omega L_2 + R_2 + \frac{1}{j\omega c_2})I_2. \tag{24b}$$

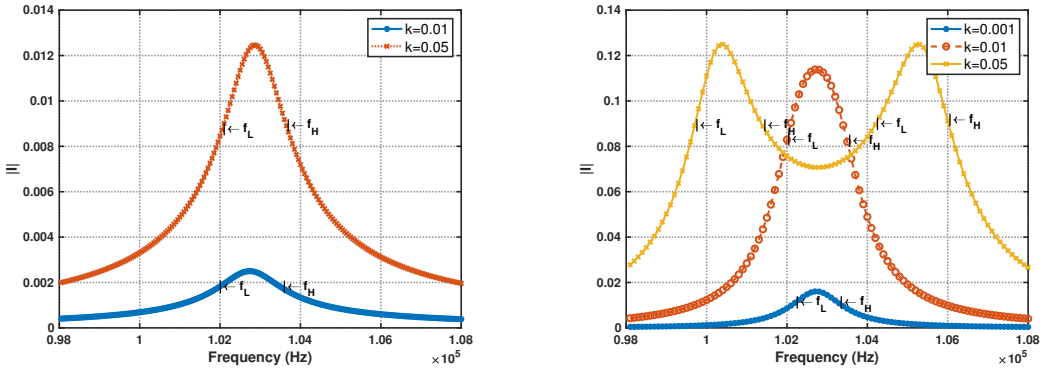

(a) Parallel-resonant MI system (b) Series-resonant MI system

Figure 24: Frequency response of MI systeml.

Substitute (24b) into (24a) we have

$$\frac{M}{L}u = (j\omega L_2 + R_2 + \frac{1}{j\omega c_2})I_2. \tag{25}$$

Therefore, parallel-resonant MI system is equivalent to a R-L-C resonator whose bandwidth B is determined by the resonant frequency $f_r = \sqrt{\frac{1}{L_2C_2}}$ and Quality factor $Q = \frac{2\pi f_r L_2}{R_2}$ as

$$B = \frac{f_r}{Q}. \tag{26}$$

The derivation is as follows:

$$I(f_l) = \frac{I(f_r)}{\sqrt{2}} \Rightarrow \frac{1}{\omega_l C} - \omega_l L = R \Rightarrow \omega_l = -\frac{R}{2L} + \sqrt{(\frac{R}{2L})^2 + \frac{1}{LC}} \tag{27a}$$

and

$$I(f_h) = \frac{I(f_r)}{\sqrt{2}} \Rightarrow \frac{1}{\omega_h C} - \omega_h L = -R \Rightarrow \omega_h = \frac{R}{2L} + \sqrt{(\frac{R}{2L})^2 + \frac{1}{LC}}. \tag{27b}$$

Subtracting (27a) from (27b) then we have $\omega_h - \omega_l = \frac{R}{L}$.

3dB Bandwidth for Loosely-Coupled Series-Resonant MI System. By eliminating the mutual inductance in Fig. 22, we have the following equivalent circuit model as shown in Fig. 25. For loosely-coupled condition $M \ll R$ or $k \ll \frac{1}{Q}$, the two circuit-loop can be regarded as independent. So, we can simplify (19) by ignore the coupling term as follows:

$$(j\omega L_1 + \frac{1}{j\omega C_1} + R_1)I_1 = U \tag{28a}$$

and

$$j\omega M I_1 - (j\omega L_2 + \frac{1}{j\omega C_2} + R_2)I_2 = 0. \tag{28b}$$

Substitute (28b) into (28a) we have

$$j\omega MU = \sqrt{R_1^2 + (\omega L_1 - \frac{1}{\omega C_1})^2}\sqrt{R_2^2 + (\omega L_2 - \frac{1}{\omega C_2})^2}I_2. \tag{29}$$

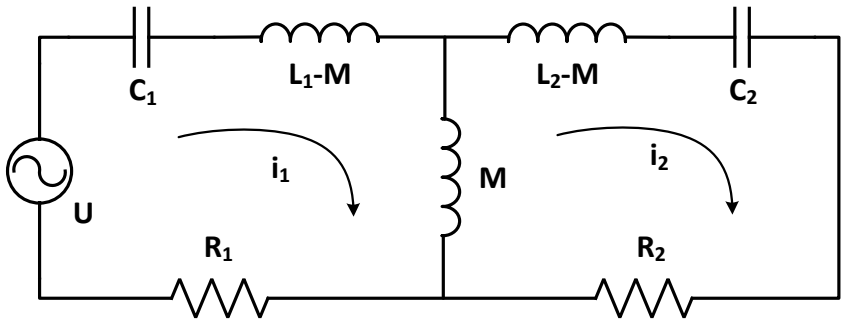

Figure 25: Series-resonant MI circuit model.

Since $\omega L - \frac{1}{\omega C} \approx 2L(\omega - \omega_r)$, 3dB bandwidth $\Delta\omega = \omega_h - \omega_l = 2\pi B$ should satisfy

$$\frac{\omega_r}{\sqrt{2}R_1R_2} = \frac{\omega_r + \frac{\Delta\omega}{2}}{\sqrt{R_1^2 + (L_1\Delta\omega)^2}\sqrt{R_2^2 + (L_2\Delta\omega)^2}}. \tag{30}$$

Suppose $\Delta\omega \ll \omega_r$, $R_1 = R_2 = R$ and $L_1 = L_2 = L$ then we can solve the 3 dB bandwidth by

$$B = \sqrt{\sqrt{2} - 1}\frac{R}{2\pi L} = 0.64\frac{f_r}{Q}. \tag{31}$$

Now it is time to define the concept of loosely-coupled. The key idea behinds loosely-coupled is $RI_1 \gg \omega MI_2$, such that (28) holds. Since $\omega MI_1 = RI_2$, the loosely-coupled condition should be $R \gg \omega M = k\omega L$. In practice, 3 times is good enough so, the loosely-coupled condition can be $k \leq \frac{1}{3Q}$.

3dB Bandwidth for Strong-Coupled Series-Resonant MI System. The received signal at the self-resonant frequency $\omega_0 = \sqrt{\frac{1}{LC}}$ can be obtained by solving the following equations:

$$j\omega MI_2 + RI_1 = U \tag{32a}$$

and

$$j\omega MI_1 + RI_2 = 0, \tag{32b}$$

which yields

$$I_2^{\omega_0} = \frac{U}{jR(Qk + \frac{1}{Qk})}. \tag{33}$$

So, $I_{2,max}^{\omega_0} = \frac{U}{2R}$ when $Qk = 1$.

The general solution of I_1 and I_2 should satisfy

$$(j(Z \pm \omega M) + R)(I_1 \pm I_2) = U, \tag{34}$$

where $Z = \omega L - \frac{1}{\omega C}$. Therefore, under resonant condition $Z_r \pm \omega_r M = 0$. For $Z_r = -\omega_r M$, we have the following:

$$R(I_1 + I_2) = U \tag{35a}$$

and

$$j\omega_r M(I_2 - I_1) = RI_2. \tag{35b}$$

The vectogram of (35) is shown in Fig. 26.

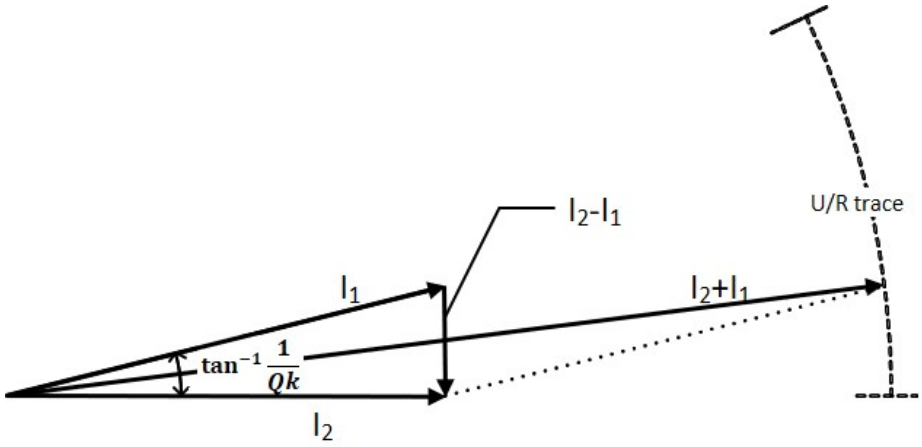

Figure 26: Vectogram of series-resonant MI system at resnant frequency $\frac{\omega_0}{\sqrt{1+k}}$.

Considering strong-coupled condition $Qk > 1$, $I_2 \approx I_1$, then we have $I_2 \approx I_1 \approx \frac{U}{2R}$. Similarly, for $\omega_r = \frac{\omega_0}{\sqrt{1-k}}$, we have $I_2 \approx -I_1 \approx \frac{U}{2R}$. Therefore, we can further simplify Fig. 25 into Fig. 27. The lower cut-off frequency ω_l can be determined by

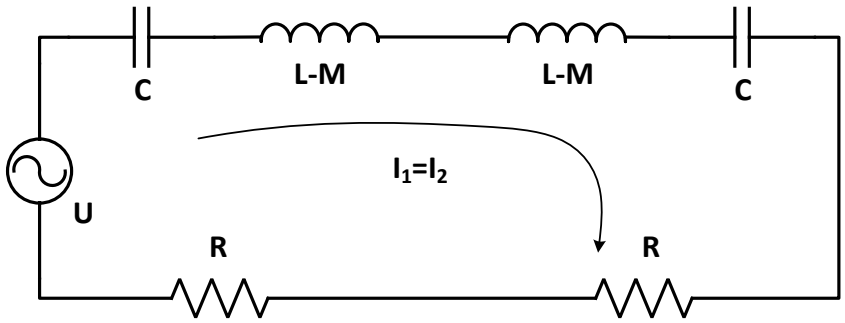

Figure 27: Strong-coupled series-resonant MI circuit model within 3 dB bandwidth.

$$4L(1-k)(\omega_r - \omega_l) = 2R, \tag{36}$$

where $\omega_r = \frac{\omega_0}{\sqrt{1+k}}$, and $\omega_l = \omega_r - \frac{R}{2(1-k)L}$. Similarly, the upper cut-off frequency $\omega_u = \frac{\omega_0}{\sqrt{1-k}} + \frac{R}{2(1-k)L}$. The physics behind (36) is that the maximum current at the resonant frequency point is determined by the pure resistance $2R$. At the cut-off frequency of 3 dB bandwidth, the impedance is $2(j\omega(L-M) - \frac{1}{j\omega C} + R) = 2(j2(1-k)L\Delta\omega + R)$.

If $I_2^{\omega_0} > \frac{U}{2\sqrt{2}R}$, the 3dB bandwidth will include whole frequency band between the two resonant frequencies, which imply that $k \leq \frac{2\sqrt{2}}{Q}$. Finally, the 3dB bandwidth can be estimated by

$$B = (\frac{1}{Q} + \sqrt{1+k} - \sqrt{1-k})f_0 \approx (\frac{1}{Q} + k)f_0. \tag{37}$$

Near-Field MI Channel Capacity. The practical coupling coefficient for near-field underwater MI wireless communication is $k \ll 10^{-2}$ according to the results of Fig. 19. Also, the normal quality factor of a coil is less than 100. Therefore, the coupling condition of the underwater wireless communication system with one transmitting and receiving coil antenna can be regarded as loosely-coupled. The received MI signal is

$$U_c = \frac{\omega M U}{R^2}\frac{1}{\omega C} = kQ^2U. \tag{38}$$

Hence, the pathloss of underwater near-field MI channel is

$$PL = 20\log_{10}(kQ^2). \tag{39}$$

Recall that the available bandwidth $B = 0.64\frac{f_r}{Q}$, and channel capacity $C = B\log_2(SNR+1)$. The optimum Q for maximum channel capacity can be determined by solving the following optimization equation,

$$\begin{aligned} \max_{Q} \quad & C = 0.64\frac{f_r}{Q}\log_2(\frac{P_T}{P_N}k^2Q^4 + 1) \\ \text{s.t.} \quad & 1 \le Q \le 100, \\ & \frac{f}{Q} \le (\sqrt{2}-1)f. \end{aligned} \tag{40}$$

Where P_T is the transmission power and P_N is the noise power. (40) can be solved by $\frac{\mathrm{d}C}{\mathrm{d}Q} = 0$, which yields

$$Q_{opt} = \sqrt[4]{(2^{\frac{4}{\ln 2}} - 1)\frac{P_N}{P_T k^2}} \tag{41a}$$

and

$$C_{max} = 0.64\frac{f_r}{Q_{opt}}\log_2(\frac{P_T}{P_N}k^2Q_{opt}^4 + 1). \tag{41b}$$

The MI channel capacity with one transmitting antenna and one receiving antenna at resonant frequency of 100 kHz is shown Fig. 28.

3.2 Underwater MI Communication Realization

3.2.1 System Block Diagram

The system block diagram of the underwater MI testbed is shown in Fig. 29. Two coil antennas are submerged in a water tank. One coil is driven by the modulated voltage signal through a coaxial cable and generates magnetic fields. Correspondingly, a voltage signal will be induced in the receiving coil antenna, which will be fed into a matched circuit also through a coaxial cable.

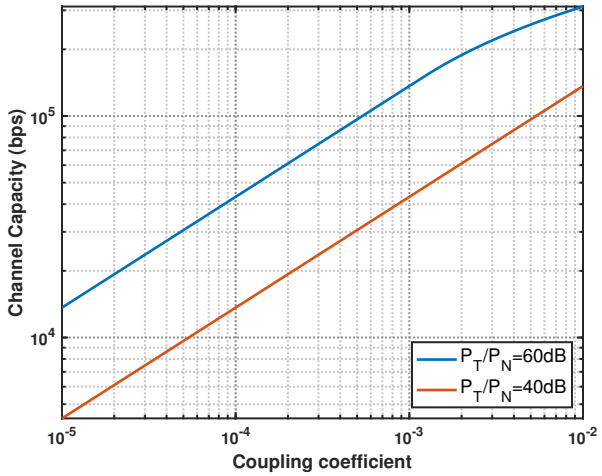

Figure 28: Near-field MI channel capacity with $f_r = 100$ kHz.

The matched circuit is designed to tune the appropriate resonant frequency and maintained an appropriate quality factor Q of the RLC resonator. On the transmitter side, a power amplifier is needed to drive the coil. On the receiver side, a low noise amplifier is needed to amplify the received signal.

The USRPs here are responsible for digital up conversion (DUC) and digital down conversion (DDC) as well as DAC and ADC. DUC convert the complex-valued baseband signal to a real-value passband signal which can be transmitted over an antenna. DDC on the other hand convert the pass-band signal sampled from antenna to the complex-valued baseband signal. Since the bandwidth of baseband signal (typical few kHz) is much smaller

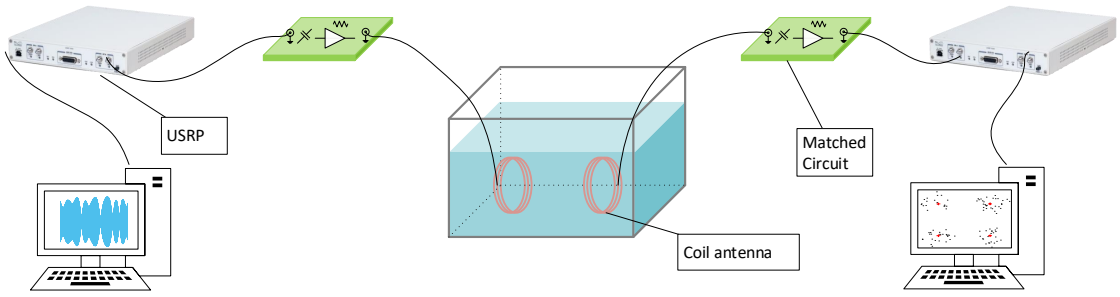

Figure 29: Overview of underwater MI testbed.

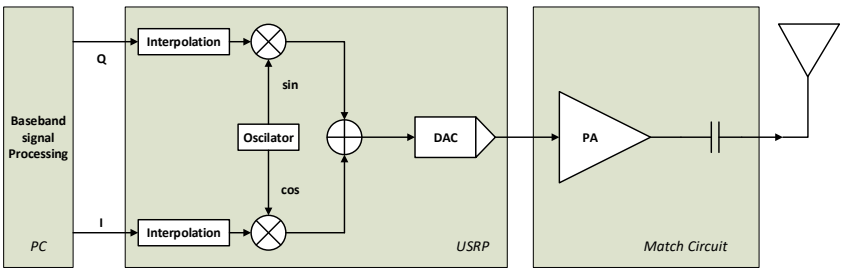

(a) Transmitter

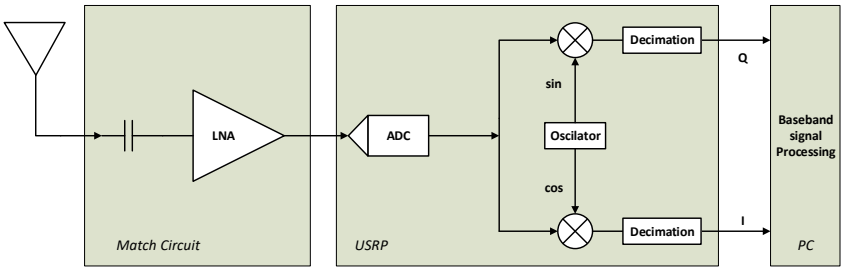

(b) Receiver

Figure 30: Function blocks of USRP and match circuit.

compared with the operation frequency (hundreds of kHz), the interpolation is required when converting from baseband to passband. Similarly, when converting from passband to baseband decimation is needed. The function block diagram of an USRP is shown in Fig. 30.

3.2.2 Coil Antenna

The most commonly used coil antennas are also known as loop antennas. Two commercial off-the-shelf loop antennas are shown in Fig. 31. The impedance of a loop antenna is

(a) (b)

Figure 31: Commercial off-the-shelf loop antennas.

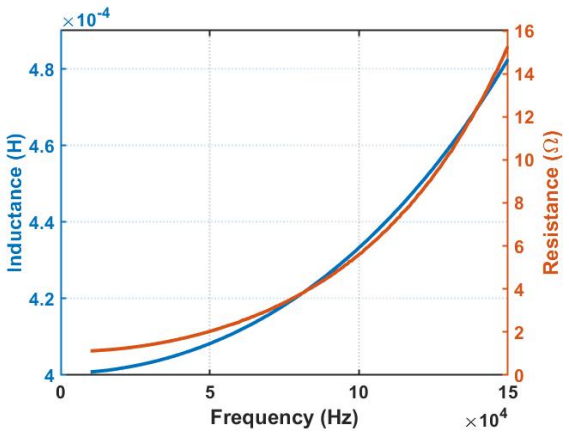

Figure 32: Impedance of the coil antenna.

shown in Fig. 32. It shows that the resistance of the coil antenna will increase significantly as the increasing of the operation frequency, which is mainly due to the skin effect.

Ferrite Assisted Geometry-Conformal Coil Antenna In some applications, the installation of coil antenna may be difficult. For example, the installation on an AUV faces two challenges. First, we do not want the coil antenna destroying the fluid dynamic features of AUV as shown in Fig. 33. Second, we need to overcome the shielding effect of the metallic body of AUV. To tackle these problems, we design a ferrite assisted geometry-conformal MI antenna which is directly wrapped along the surface of an AUV. The antenna prototype is shown in Fig. 34.

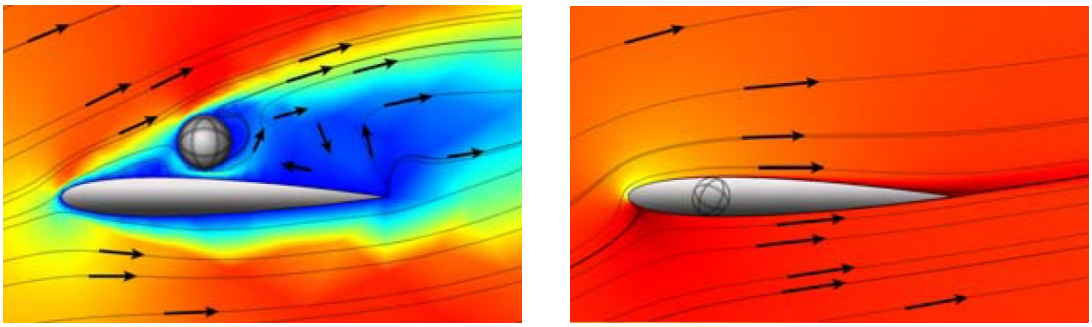

(a) AUV with a conventional triaxial antenna (b) AUV with geometry-conformal antenna

Figure 33: Velocity fields of flows around an AUV with different coil antennas.

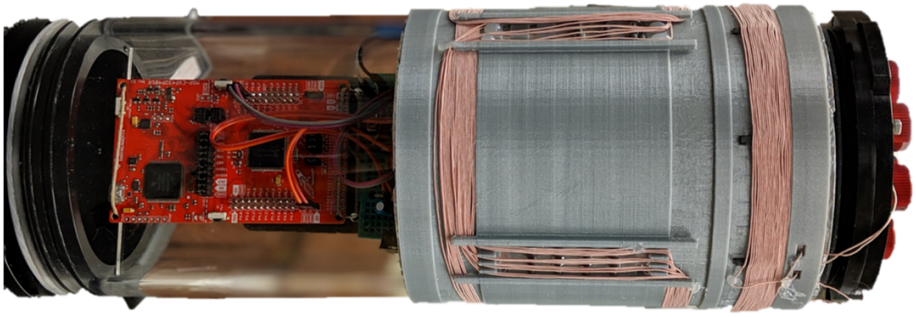

Figure 34: Geometry-conformal MI antenna prototype.

Although the geometry-conformal antenna design is good for fluid dynamic efficiency, it can not directly be used for transmitting or receiving MI signals, because the metallic surface of an AUV will generate opposite image currents to cancel MI signals. Fortunately, ferrite materials with high magnetic permeability can help to overcome such a problem. As shown in [112], ferrite materials have been used to solve a similar problem on oil pipes for wireless power transfer. A COMSOL simulation model of the designed ferrite-assisted geometry-conformal MI antenna is shown in Fig. 35.

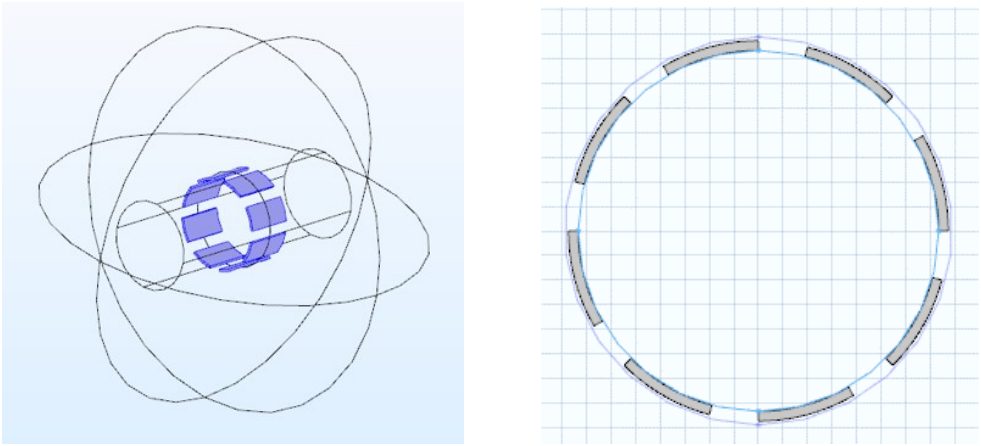

(a) Model overview (b) Ferrite material coverage

Figure 35: Ferrite assisted conformal MI antenna simulation model.

The generated magnetic field strength of the proposed antenna is shown in Fig. 36. It is shown that by applying ferrite materials between the coil and metallic surface, the magnetic

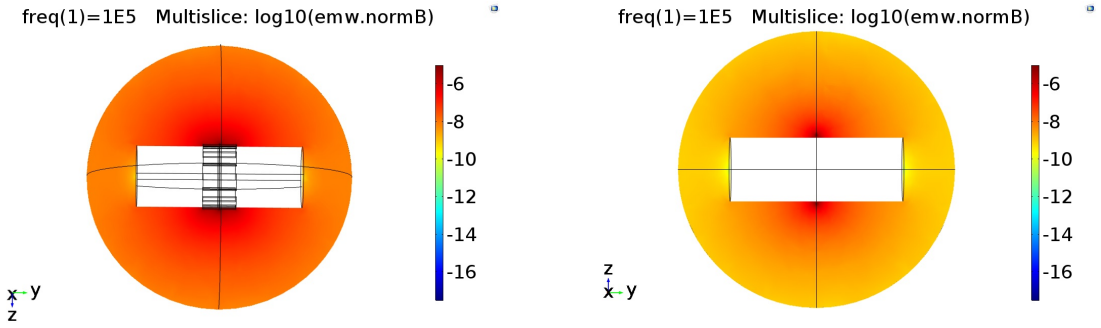

(a) With ferrite

(b) Withoug ferrite

Figure 36: Magnetic field strength of conformal antenna with and without ferrite materials. Dark color means strong intensity.

field can be significantly enhanced.

The impacts of the ferrite permeability and the coverage area of the ferrite materials are shown in Fig. 37 and Fig. 38, respectively. Fig. 37 shows that higher permeability results in a stronger magnetic field but not in a linear form. In Fig. 38, the magnetic field intensity is measured under different coverage angles from 5 to 45 degrees with $\mu_r = 300$. Here, we refer to an angle to present the ferrite coverage area as shown in Fig. 35(b). Eight pieces of ferrite sheet were equally attached on an cylindrical surface. Hence, The ferrite coverage ratio can be measured by an angle (e.g. 45 degree represents fully coverage). It is shown that, the full coverage can achieve the best antenna gain, nearly 20db enhancement compared to the situation without ferrite materials. But for economical considerations, 25 degree is a good choice, which can achieve more than 18db improvement with only 55% ferrite material usage.

3.2.3 Matched Circuit

One of the key functions of the matched circuit is to scale up the received MI signal to a proper range such that the SNR of the received signal can be guaranteed within a proper scale. Theoretically, if the transmission power is fixed, the system SNR is determined by the ambient noise power. However, for a practical MI system, the SNR is mainly determined by the matched circuit. The reasons are as follows. First, for MI communications, the

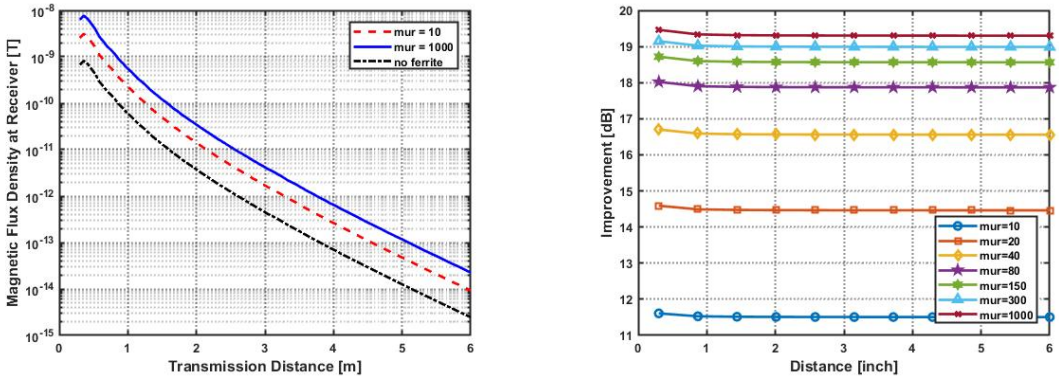

(a) (b)

Figure 37: The impact of ferrite permeability to the magnetic field.

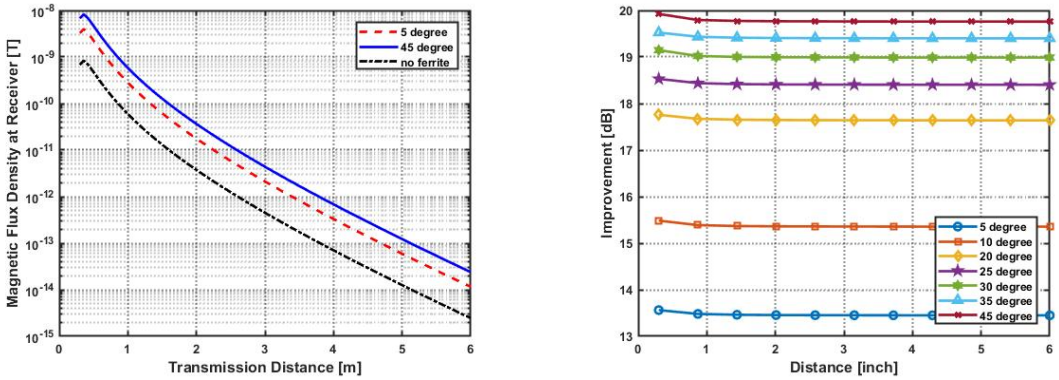

(a) (b)

Figure 38: The impact of ferrite coverage to the magnetic field.

available bandwidth is limited, typically tens of kHz. Suppose the noise spectrum density is -140 dBm/Hz, then the noise power would less than -90 dBm. Second, the path loss of underwater MI channel is at least 54 dB/λ. Considering that the MI communication range is within the distance of a wavelength, the received signal power would be grater than -50 dBm if the transmission power is 10 dBm. Therefore, the expected SNR of the MI communication system can greater than 40 dB.

However, the previous analysis assumed that the MI system has the infinitesimal sampling sensitivity level. Obviously, that is not the case for a practical system. First of all, the sampling sensitivity of an ADC is limited. For example, the ADC in the USRP is 14 bits with the input voltage within 3 V. thus the sampling sensitivity is no more than 0.18 mV,

Table 2: MI testbed parameters.

Parameter	Value	Description
f	102.7 kHz	Operation frequency
k_{opt}	10^{-6}	Optimal coupling coefficient point
g	10	Voltage gain of LNA
Q_{opt}	16.2	Optimal quality factor
U_T	0.5 V	Tx voltage amplitude
U_R	1.3 mV	Rx voltage amplitude
U_N	0.18 mV	Noise amplitude
$SNR_{k=10^{-6}}$	17 dB	Signal to noise ratio
B	4.06 kHz	3dB bandwidth
L	400 μH	Coil inductance
L	4 Ω	Coil resistance
C	6 nF	Resonant capacitor

which can be regarded as the noise floor of the practical MI testbed system. Suppose the amplitude of the transmitter input voltage is 1 V, and we want to optimize MI performance at $k = 1e^{-6}$. Based on (38) and (41) we can obtain the optimal system parameters for the matched circuit as shown in Table 2. The matched circuit design is shown in Fig. 39.

3.2.4 MI Transceiver Design

The symbol rate of the MI transceiver is set to 4k sps which is determined by the available bandwidth. Considering the minimum SNR is 17 dB, we choose 16 QAM as our modulation scheme. The sampling rate of ADC is 100 M samples per second which is too sufficient for the low frequency MI communication system. In order to lower the computation complexity, we set the decimation factor to 250, which makes the baseband

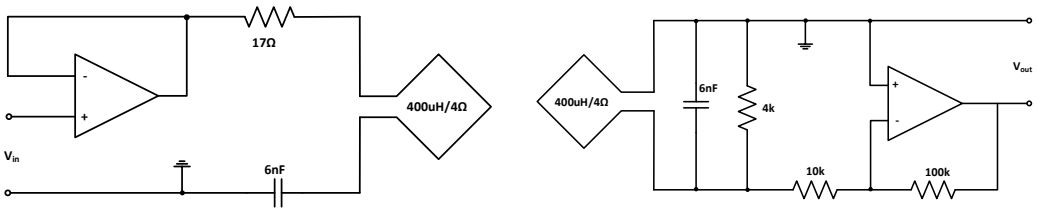

(a) Tx (b) Rx

Figure 39: Matched circuit design for MI testbed.

sample rate to 40 k. Therefore, each symbol will have 10 samples. Suppose each data frame have 200 symbols. The parameters of MI transceiver are summarized in Table 3.

Table 3: MI transceiver parameters.

Parameter	Value	Description
Symbol rate	4 k	samples per symbol
Sampling rate	100 M	samples per second
Decimation factor	250	
Samples per symbol	10	
Frame size	200	symbols per frame
Raw frame size	2020	samples per frame
Slide window	10	samples
Modulation scheme	16 QAM	
Carrier frequency	102.7 kHz	

The first step for the receiver is to detect the valid data frame. Only when the received signal power passes the threshold the following signal is regarded as a valid data frame. The frame size is 2000 samples. A slide window of 10 samples (1 symbol) is used to detect the signal power and the raw frame data has the size of 2020 samples. The overall frame detection procedure is shown in Fig. 40. The received output baseband waveform is shown in Fig. 41.

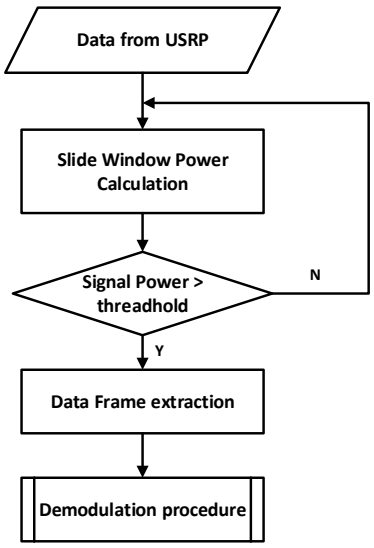

Figure 40: Valid data frame detection procedure.

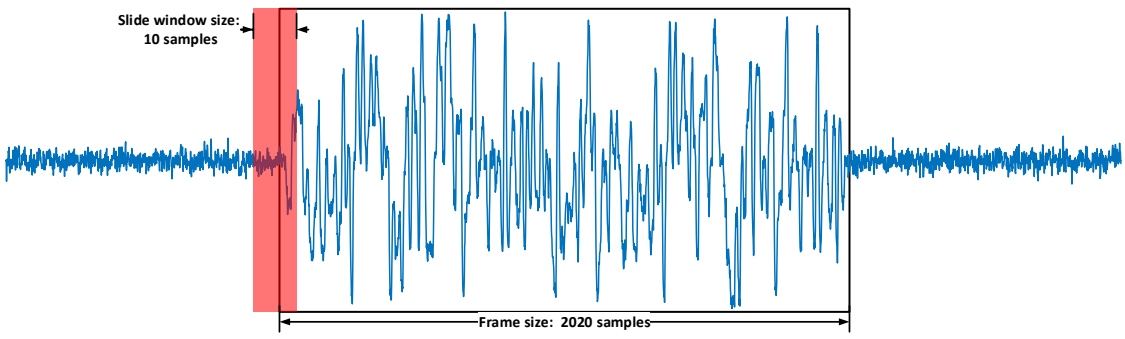

Figure 41: Rx baseband frame detection.

3.3 Point to Point Links: Signal Processing

In loosely coupled regions, the MI channel response can be regarded as a time invariant channel, since the variance of the coupling coefficient between two coils mainly affects the amplitude of the received signal but won't introduce phase distortions. Therefore, the coherence modulation schemes including phase shift keying (PSK) and quadrature amplitude modulation (QAM) are good choices for MI communications. These method offer bandwidth efficiency, *i.e.*, more than one bits can be transmitted per symbol per Hertz of occupied bandwidth. However, the resonant circuit will introduce delays to the received signals. Also, the small carrier frequency offset between transmitter and receiver will cause phase shift of the received symbols. Therefore, before demodulation, the symbol and carrier synchronizations need to be performed. The over signal processing procedure is shown in Fig. 42.

3.3.1 Symbol Synchronization

The eye diagram of the received MI signal is shown in Fig. 43. Obviously, at different sampling point, we will have different demodulation results. It is very critical to make the decision on the right sampling point. Fig. 43 (b) shows that we can use slope as the criteria to find the optimal sampling point. Because at the optimum sampling position the slope of

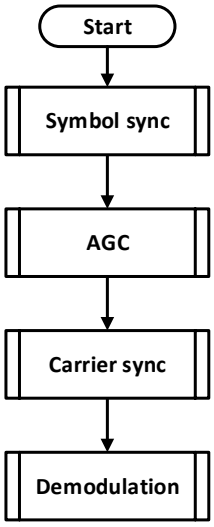

Figure 42: Rx signal processing procedure.

the received symbol pulse has nearly zero slope, while at other sampling points the slope is mostly non-zero. Thereby the symbol synchronization problem can be formulated as

$$\underset{k=1:sps}{\mathbf{argmin}} \quad \sum_{n=0}^{N-1} |x(10n+k) - x(10n+k+1)|. \tag{42}$$

Where, $x(\tau)$ is the sampling value, N is the number of symbols per data frame, k is the sampling position and *sps* stands for samples per symbol. Equation (42) will return the optimum sampling point. In each data frame, the optimum sampling point of each symbol won't change. In order to speed up the computation and save energy we don't need to compute the slope of all sampling points.

3.3.2 Automatic Gain Control

The AGC is designed to scale up the small received signal to a proper range such that the siganl can be correctly demodulated. Especially for QAM modulation scheme, the demodulation is sensitive to the amplitude of the received signal. The proper gain can be

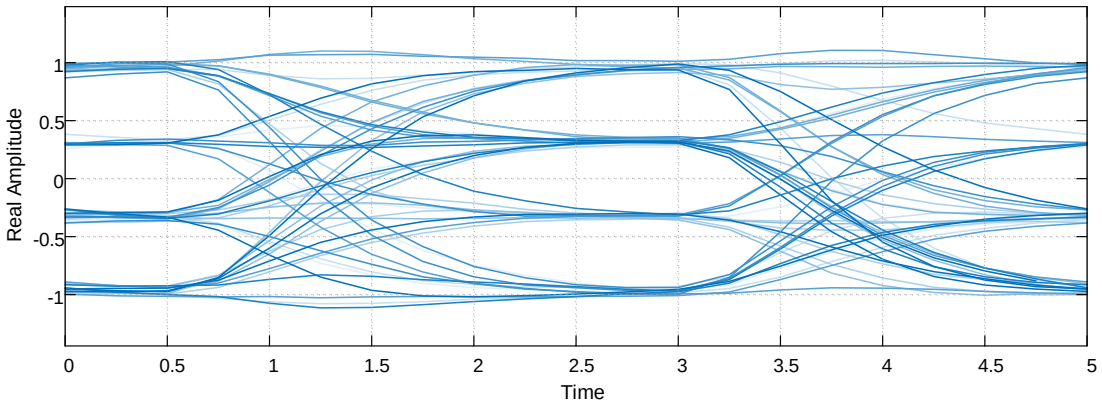

(a)

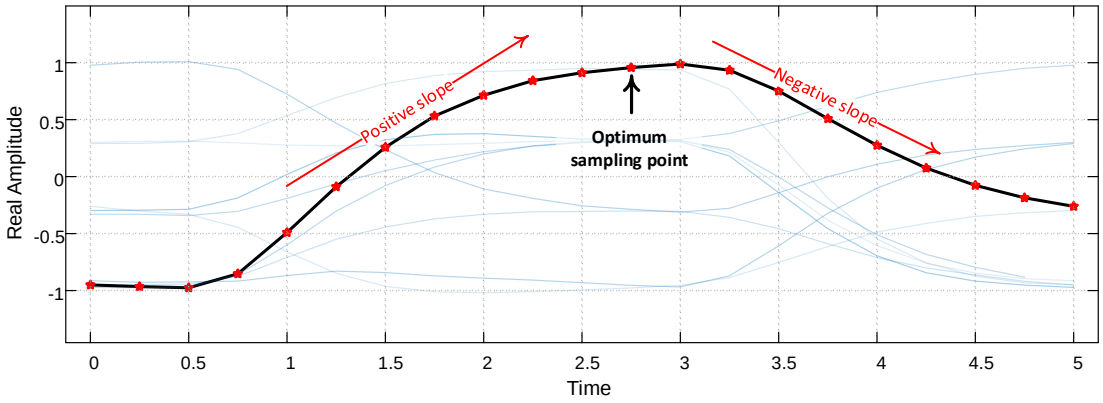

(b)

Figure 43: Eye diagram of received symbols.

determined by calculating the variance V of the received symbol $\mathbf{x}$.

$$V = \frac{1}{N-1}\sum_{i=1}^{N}|x_i - \mu|^2, \tag{43}$$

where μ is the mean of $\mathbf{x}$,

$$\mu = \frac{1}{N-1}\sum_{i=1}^{N}x_i. \tag{44}$$

Suppose the average reference power of the constellation is P_{ref} than the gain can be determined by

$$gain = \sqrt{\frac{P_{ref}}{V}}. \tag{45}$$

To speed up the computation and save energy, we can reduce the symbol number when calculating the variance V of the received data frame.

3.3.3 Carrier Synchronization

The symbol received directly from the receiving antanna during the kth signaling interval $(kT_s < t < (k+1)T_s)$ is

$$r(t) = G_a[a_I(k)p(t-kT_s)\cos(\omega_0 t+\theta) + a_Q(k)p(t-kT_s)\sin(\omega_0 t+\theta)] + w(t), \tag{46}$$

where G_a is the channel gain, $a_I(k)$, $a_Q(k)$ are the in-phase and quadrature amplitude of the transmitted symbol, respectively, $p(t-kTs)$ is the pulse shape, and $w(t)$ is the noise. After digital down conversion, the in-phase and quadrature component are separated as follows:

$$I(t) = G_a[a_I(k)\cos(\theta-\hat{\theta}) - a_Q(k)\sin(\theta-\hat{\theta})]p(t-kT_s) + w_I(t) \tag{47a}$$

and

$$Q(t) = G_a[a_I(k)\sin(\theta-\hat{\theta}) + a_Q(k)\cos(\theta-\hat{\theta})]p(t-kT_s) + w_Q(t). \tag{47b}$$

At the optimum sampling point, $p(t-kT_s) \approx 1$, so the discrete version of the received symbol is

$$\begin{bmatrix} I(k) \\ Q(k) \end{bmatrix} = \begin{bmatrix} \cos(\theta-\hat{\theta}) & -\sin(\theta-\hat{\theta}) \\ \sin(\theta-\hat{\theta}) & \cos(\theta-\hat{\theta}) \end{bmatrix} \begin{bmatrix} a_I(k) \\ a_Q(k) \end{bmatrix} + \begin{bmatrix} w_I(k) \\ w_Q(k) \end{bmatrix}, \tag{48}$$

where $\theta-\hat{\theta}$ is the phase difference between the transmitter and receiver carrier. Therefore, the received symbol can be regarded as the rotated version of the transmitted symbol. To correctly demodulate the symbol, such rotation must be corrected. Apparently we first need to estimate the phase error $\theta-\hat{\theta}$, which can be done in the following two ways.

Preamble Assisted Carrier Synchronization Since the symbols in the preamble are deterministic, it can be used to correct the phase error. Suppose the first symbol in the

preamble is $a_I(1) + ja_Q(1)$, and the first received symbol is $I(1) + jQ(1)$ as

$$\theta - \hat{\theta} = angle\ (a_I(1) + ja_Q(1))(I(1) + jQ(1))^*). \tag{49}$$

Then the carrier synchronization can be easily performed by

$$[I(k) + jQ(k)]e^{j(\theta - \hat{\theta})}. \tag{50}$$

Carrier Synchronization by PLL If there exists a carrier frequency offset (CFO), denoted as Δf, between the Tx and Rx, then $\theta - \hat{\theta} = 2\pi\Delta f t$. In this case PLL need to be implemented to compensate the CFO. The block diagram of the PLL is shown in Fig. 44. The phase error can be defined as [79]

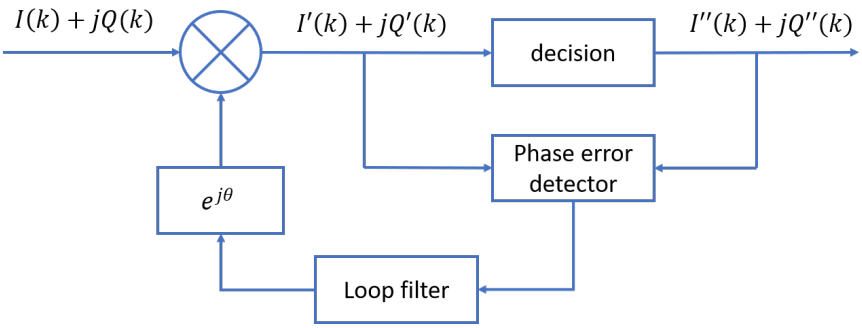

Figure 44: The block diagram of the carrier phase PLL.

$$e(k) = Q''(k)I'(k) - I''(k)Q'(k). \tag{51}$$

Here $I''(j) + jQ''(k)$ is the closet constellation point of $I'(k) + jQ'(k)$.

Since MI communication working within LF (30 - 300 kHz) range, the CFO can be very small. Within one data frame the phase error caused by CFO can be ignored. For example, suppose the crystal accuracy of the transceiver is 20 PPM, and the frame period is 50 mS, then the phase error caused by CFO is 0.02 π. Therefore, PLL may not be necessary, which will simplify the receiver design.

3.3.4 Pulse Shaping

For MI communications, due to the non-radiation and fast attenuation properties, we do not need to worry about the spectrum interference. Therefore, the natural rectangular pulse shape is a good choice, because it has no inter symbol interference and require no additional signal processing. Since the coil antenna can be regarded as a low pass filter, the rectangular pulse will be smoothed out at the receiver size and the received pulse shape is shown in Fig. 43.

3.4 Simulations and Experiments

The block diagram of the proposed MI transceiver is shown in Fig. 45. The parameters of the coil antenna and the resonant capacitor are shown in Table 4. The carrier frequency

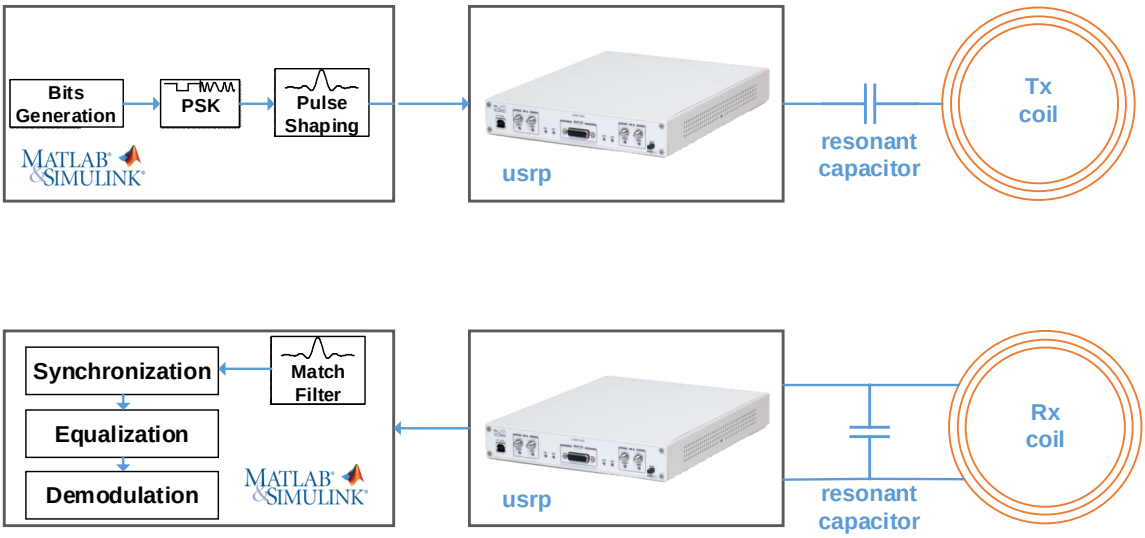

Figure 45: MI transceiver block diagram.

is set to 102.8 kHz which is the self-resonant frequency of the coil antenna. The baseband signal processing is handled using Matlab, which includes bit generation, modulation, and pulse shaping on the transmitter side, as well as match filtering, synchronization (including symbol synchronization and frame synchronization), equalization, and demodulation on the receiver side. The USRP is responsible for digital up/down conversion, analog to digital,

Table 4: System parameters.

Parameter	Value	Description
$L_1,\ L_2$	400 μH	self inductance of coil antenna
$C_1,\ C_2$	6 nF	resonant capacitor
$r_1,\ r_2$	4 Ω	intrisic resistor of coil antenna @100 kHz
U	1 V	input voltage

and digital to analog conversion.

3.4.1 Simulation Results

The overall Simulation model is shown in Fig. 46. For a better illustration, we divided the system into three parts namely the transmitter part, receiver part, and MI channel part. For the simulation of MI channel, we use a mutual inductance to simulate the coupling between two coils, and use a controlled voltage source to couple the modulated signals into the resonant circuit. The circuit parameters strictly follow the values in Table 4. It is worthy pointing out that we adopt freeload receiver design here and just measure the capacitor voltage as MI input signals. Such a receiver design will benefit us with the highest SNR.

The transmitter and receiver design follow the standard PSK and QAM modulation and demodulation procedures. We just emphasize some key parameters here which have significant impacts on the communication performance. The first one is the noise power added on the receiver side. The measured noise power of our testbed is -67 dBW. Another key parameter is the maximum power gain of the automatic gain controller (AGC), since it will determine the maximum transmission range of the MI system. Consider that in weakly

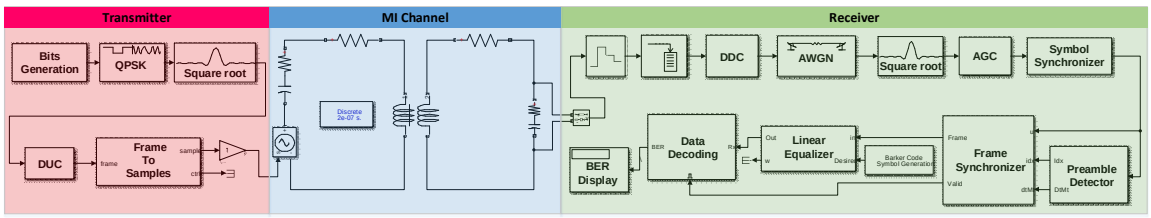

Figure 46: Simulation model of the MI wireless communication system.

coupled region, the received MI signal strength is proportional to the coupling coefficient k, and the received signal power reaches its maximum at $k = \frac{1}{Q} = 0.015$. To guarantee that the system works when $k \geq 10^{-4}$, we set the maximum power gain of AGC to 40 dB.

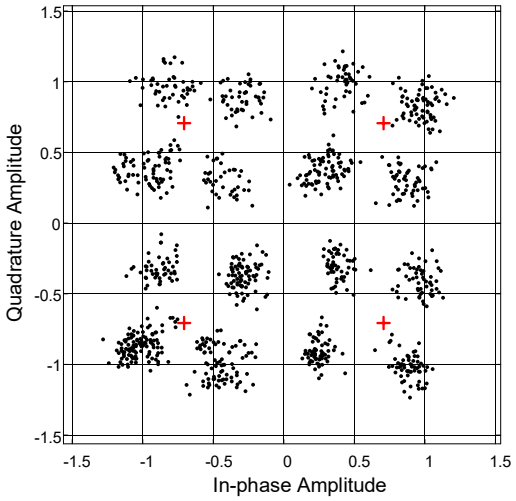

(a) demodulation results @ k=0.0001 with symbol rate of 3200 sps

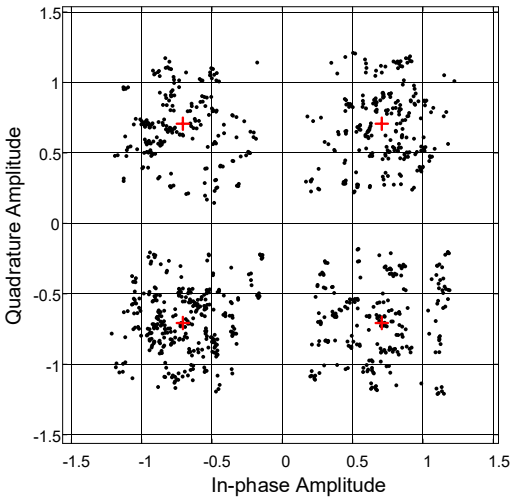

(b) demodulation results @ k=0.04 with symbol rate of 8000 sps

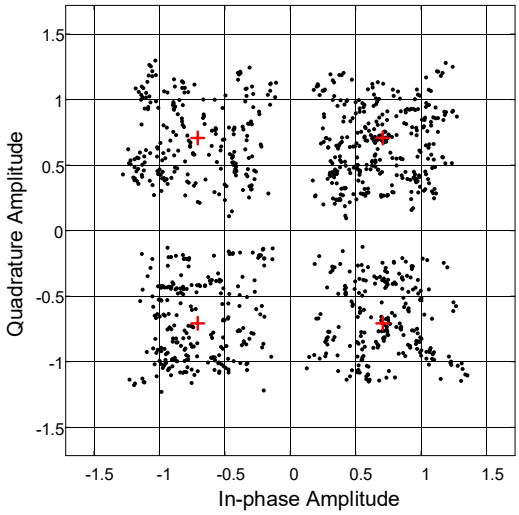

(c) demodulation results @ k=0.06 with symbol rate of 10667 sps

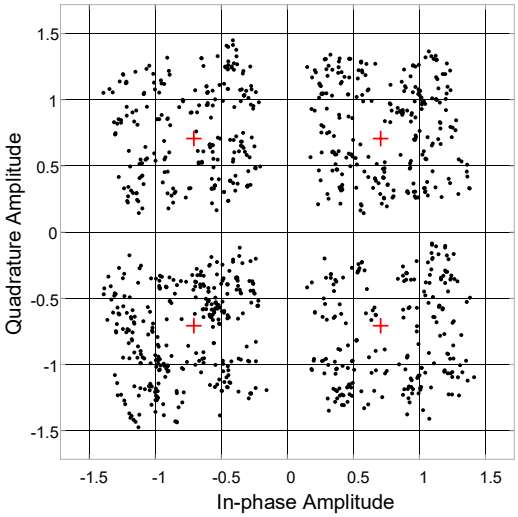

(d) demodulation results @ k=0.08 with symbol rate of 8000 sps

Figure 47: Mobility impacts to the demodulation results of the MI wireless communication system with maximum achievable symbol rate and zero BER under different coupling coefficients.

Since our purpose here is to verify the available bandwidth of an MI wireless communication system under different coupling conditions, we do not apply any equalizer on the receiver side in our simulation, such that the demodulation results will be directly determined by the MI channel conditions. In other words, we bypass the equalizer module in Fig. 46 and directly demodulate the output frame of the carrier synchronizer. Fig. 47 shows the constellation plot of the output of the carrier synchronizer when the maximum symbol rate was achieved with zero BER under different coupling conditions. The simulation results agree with our previous analysis. Specifically, the maximum symbol rate remains 3200 symbols per second (sps) within the loosely coupled region where $0.0001 < k < 0.01$. Within strongly coupled region, the maximum symbol rate increases as coupling coefficient k increases and reaches its maximum at $k = 0.06$. If we further increase the coupling coefficient, when $k > \frac{4}{Q}$ the maximum symbol rate will decrease.

3.4.2 Experiment Results

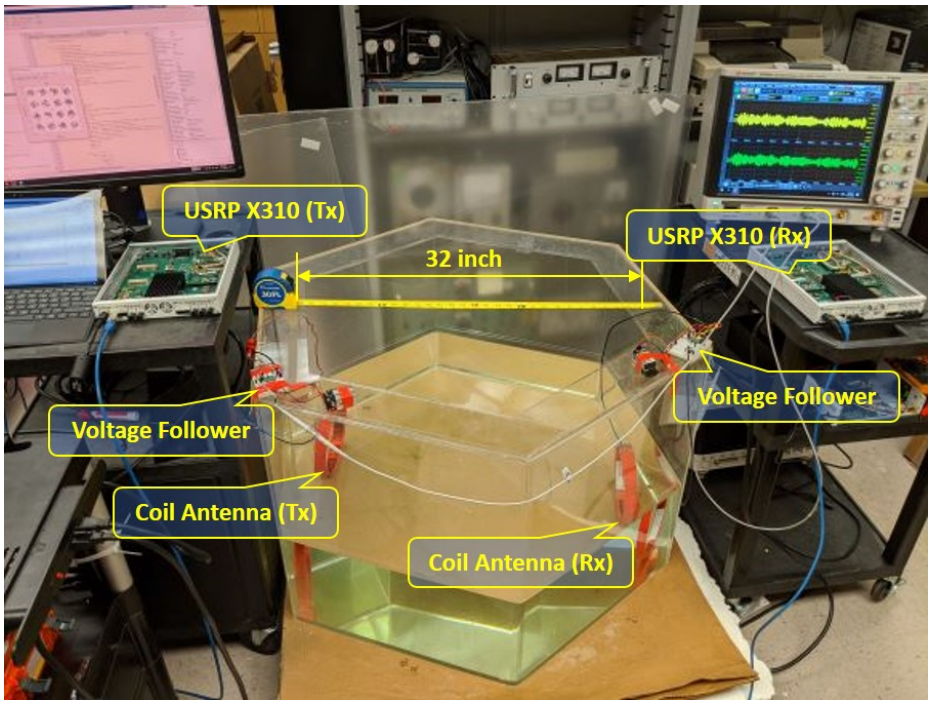

Figure 48: Underwater MI testbed.

Our underwater MI testbed is shown in Fig. 48. Two coil antennas with radius $r = 10$

cm are submerged into a water tank with the maximum distance at 32 inch. Between the coil antenna and USRP X310, a voltage follower is applied to isolate the impedance impact on the resonant conditions from LFTX and LFRX USRP daughter board (DC-30 MHz) which has a built-in input and output resistance of 50 Ω. Actually, this is the key step to realize the free-load condition and guarantee that the coil resonator has a high-quality factor. For example, our coil antennas have similar parameters as shown in Table 4 with $Q = 65$ at resonant frequency. If we directly connect the LFTX daughter board to the Tx coil antenna, the quality factor will decrease dramatically to $Q = 5$. With such a low Q factor, the whole system even cannot work within 10 inch in the air. With our free-load design, we can achieve the maximum MI receiver sensitivity.

When we submerged the coil antenna into the water, the coil impedance changed dramatically if the enameled wire directly contacts the water. To solve this problem, we sealed the coil with electric tape. The impedance of the coil antenna before and after sealing is shown in Fig. 49.

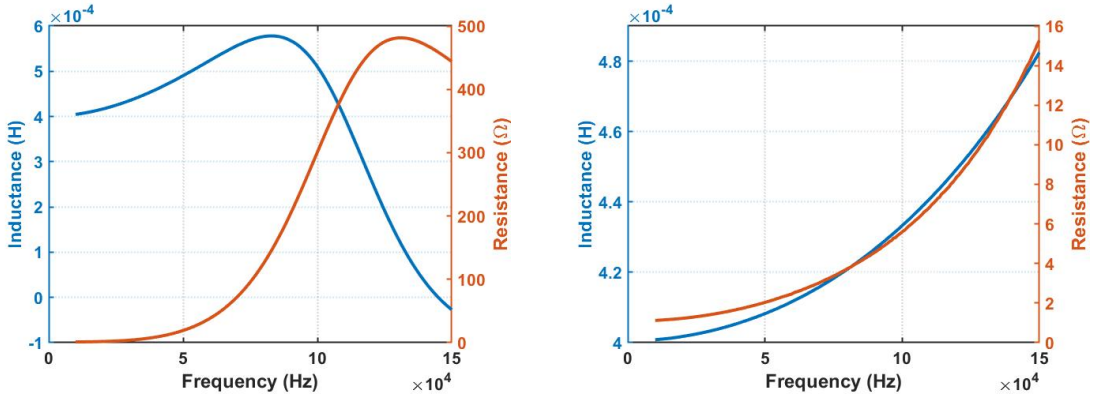

(a) underwater coil impedance in contact with water

(b) underwater coil impedance sealed with electric tape

Figure 49: The impedance of a underwater coil antenna.

A 5 nF capacitor is in series with the Tx coil and in parallel with the Rx coil. Hence the self resonant frequency of the MI transceiver is $f_0 = 110$ kHz. The self resistance of the capacitor is around 0.7 Ω, and the quality factor of the underwater MI transceiver is $Q = 36$. The distance between the Tx coil and the Rx coil is 32 inch. The coupling

coefficient between these two coil antennas would be $k < 0.001$ which indicates that these two MI coil antennas are loosely coupled. Therefore the 3 dB bandwidth can be estimated as $\Delta\omega = \frac{1}{Q} f_0 = 3$ kHz.

After figuring out the available bandwidth, our underwater MI testbed is ready to evaluate the communication performance. The procedure is as follows. We modulate some text message using different modulation scheme (QPSK and 16 QAM) with center frequency of 113kHz which is the self-resonant frequency of the coil antenna. Then we gradually increase the symbol rate until the message cannot be demodulated correctly on the receiver side. The peak amplitude of the output passband signal is set to 0.1 V. Since the overall resistance of the transmitter is around $r_c + r_L \approx 8\ \Omega$, the transmitting power can be estimated as $p_T \leq 1.25$ mW. The signal processing procedure is shown in Fig. 46. Some key parameters are summarized in Table 5. The QPSK demodulation results without equalization are shown in Fig. 50 (a) and (b) when the symbol rate is 3 ksps and 6 ksps, respectively. By applying the linear equalizer we can successfully demodulate the results at the symbol rate of 6 ksps and the experiment results for QPSK and QAM are shown in Fig. 50 (c) and (d).

Table 5: Key parameters for signal processing.

Function Block	Parameters	Values
RRC filter	Rolloff factor	0.6
	Filter span in symbols	10
	Samples per symbol	$40 \sim 80$
Carrier synchronizer	Damping factor	0.707
	Normalized loop bandwidth	0.1
Linear equalizer	Algorithm	LMS
	Number of taps	3
	Reference tap	1
	Step size	0.008

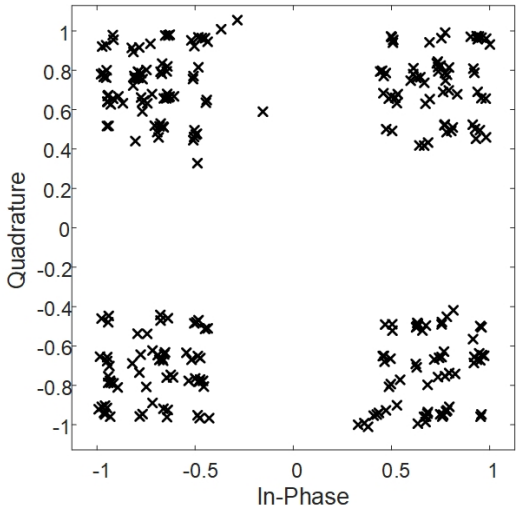

(a) QPSK demodulation results with symbol rate of 3 Ksps and 0 BER, without equalization

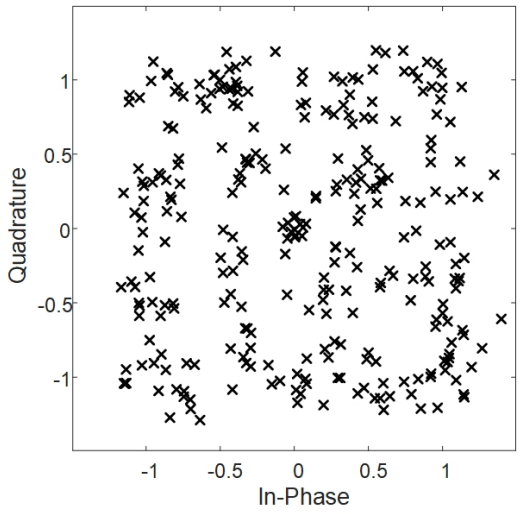

(b) QPSK demodulation results with symbol rate of 6 Ksps, without equalization

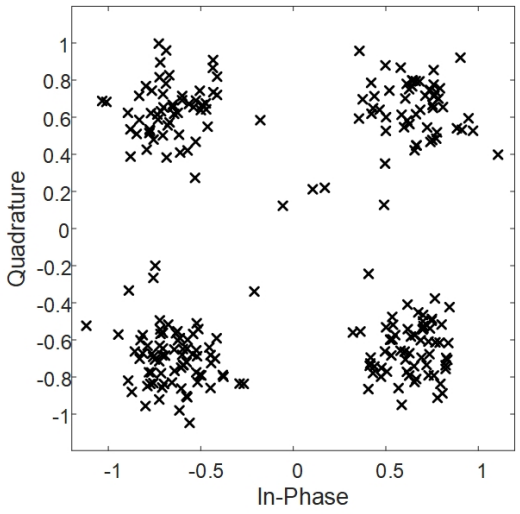

(c) QPSK demodulation results with symbol rate of 6 Ksps and 0 BER, with equalization

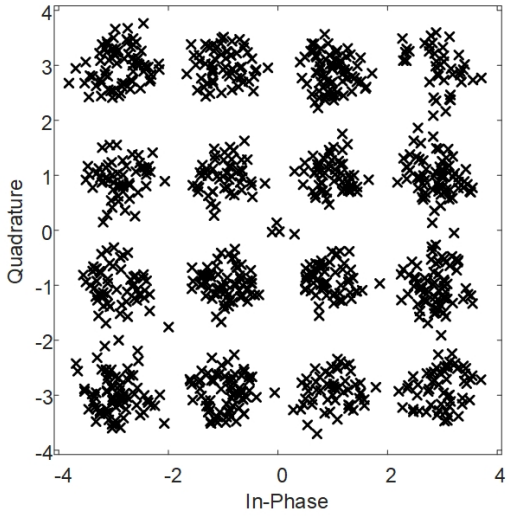

(d) QAM demodulation results with symbol rate of 6 Ksps and 0.0137 BER , with equalization

Figure 50: Experiment results for underwater MI wireless communications with transmission power $P_T \leq 1.25$ mW and transmission distance of 32 inch. The transmitted message is "Hello world through underwater MI wireless communications!".

4 Underwater Stress Wave Communications

Stress wave has many applications, such as structural health monitoring (SHM) on the pipeline, underground exploration, and communication in the oil drilling process [119, 113]. Stress wave is commonly used for Non-Destructive Testing (NDT) and Structure Health Monitoring (SHM) [5, 85] since 1940. The propagation characteristics of stress wave along buried pipelines have been presented in [59]. The fundamental principle for NDT is analyzing the echo of impulse signal to detect the location of structure defects, *e.g.*, cracks, which is different from communication technologies.

As early as 1972, Johnson [44] had demonstrated seismic communications at a distance of 760 ft through hard rocks with a data rate of 2 pulse per second. In comparison to RF wireless communications, such a poor communication performances make it barely useful in the area where RF technology is applicable. The studies on acoustic wave propagating in the solid material (stress wave) have demonstrated good transmission performances [110, 33]. The stress wave communication is promising thanks to its high propagation speed and small attenuation in solid material [118].

A couple of researchers have demonstrated stress wave communicatins (SWC) on some other solid mediums with different titles of this technology. Johnson [44] had demonstrated seismic communications with a data rate of 2 pulses per second at a distance of 760 ft through hard rocks back in 1972. Lawry *et al.* [56] present a system capable of high data-rate transmission through solid metal barriers using ultrasound. The proposed prototype has realized 12.4 Mbps transmission data rate by using the orthogonal frequency-division multiplexing (OFDM) modulation scheme. But the communication media of their system is a 2-inch metal wall which is completely different from a long pipe. In 2012 Kailaswar *et al.* propose ConcreteComm using stress wave and successfully demonstrate a 10 kbps wireless link on a concrete block with dimension of $60 \times 12.5 \times 8''$ [46]. Later on Siu *et al.* investigate a specific concrete channel model for stress wave communications in [90, 91]. The impulse response for a 60-inch concrete channel is tested by experiments. The maximum data rate that can be achieved by this specific channel is also evaluated based on experiment results.

Ji *et al.* investigated the time reversal based pulse position modulation for SWC in concrete structures in [40]. Wu *et al.* propose a stress wave based pulse position modulation (PPM) communication system in [110]. He *et al.* demonstrate a stress wave communication system based on BPSK in [34].

The similar communication approach had been applied to the high-rate acoustic logging while drilling (LWD) telemetry through drill-strings since 1948. The propagation analysis of acoustic waves along drill-strings can be found in [24] back in 1989. It was concluded that the attenuation is surprisingly low, less than 4 dB/1000 ft; and the difficultly is suppressing the echo and background noise. The drill-string channel consists of pipes and joints periodically, which results in a comb-filtering-like channel transfer functions. The corresponding channel capacity of an LWD acoustic telemetry system under drilling conditions is calculated in [26], which concludes that the practical data rate is around 500 bps for the 6000 ft drill-string channel. The adaptive OFDM is regarded as the promising modulation scheme for such comb-filtering-like channels as shown in [33, 62, 68]. The most significant different between pipeline channel and drill-string channel is that the pipeline is well welded during the deployment. Hence, more flat channel transfer function would be expected for pipeline channels. Furthermore, the background noise for pipeline channels is much lower than the drill-string channel. Therefore, much better communication performances could be expected for a pipeline stress wave communication system compared with a drill-string LWD acoustic telemetry system.

In recent years, wireless sensor networks (WSNs) are considered to be a compelling platform for SHM [61, 36]. Since concrete structures are usually planted underground or immersed underwater, the signal is shielded by the environment and it's not realizable to use the long distance radio communication. Therefore, stress wave communication may find its applications in WSN for SHM.

4.1 Stress Wave Propagation Analysis

The stress wave propagation in an elastic or viscoelastic medium is governed by Navier's equation, which is in the form of

$$\mu\nabla^2\mathbf{u} + (\lambda+\mu)\nabla(\nabla\cdot\mathbf{u}) = \rho\left(\frac{\partial^2\mathbf{u}}{\partial t^2}\right), \tag{52}$$

where λ and μ are Lamé constants, which determine the bulk wave velocity of the material. $\mathbf{u}$ is the displacement vector and ρ is the material density. To simplify this problem, Helmholtz's decomposition is applied to the displacement vector in (52). The displacement vector then is decomposed by a combination of the scalar potential, Φ, and vector potential, $\mathbf{\Psi}$,

$$\mathbf{u} = \nabla\Phi + \nabla\times\mathbf{\Psi}. \tag{53}$$

Substituting (53) into (52) and using calculus identities for simple algebra, (52) can be decomposed into two equations as follows:

$$\left(\frac{\partial^2\Phi}{\partial t^2}\right) - \left(\frac{\lambda+2\mu}{\rho}\right)\nabla^2\Phi = 0 \tag{54}$$

and

$$\left(\frac{\partial^2\mathbf{\Psi}}{\partial t^2}\right) - \left(\frac{\mu}{\rho}\right)\nabla^2\mathbf{\Psi} = 0. \tag{55}$$

Equation (54) and (55) fall into the scalar Helmholtz equation and vector Helmholtz equation, respectively. Two additional constants c_l and c_s are defined as

$$\begin{cases} c_l = \sqrt{\dfrac{\lambda+2\mu}{\rho}} \\ c_s = \sqrt{\dfrac{\mu}{\rho}} \end{cases}, \tag{56}$$

where c_l denotes the longitudinal bulk wave velocity and c_s is the shear bulk wave velocity. With the assumption that the hollow cylinder is elastic isotropic and infinity long, the boundary condition at two ends can be ignored. On the inner and outer surfaces of the

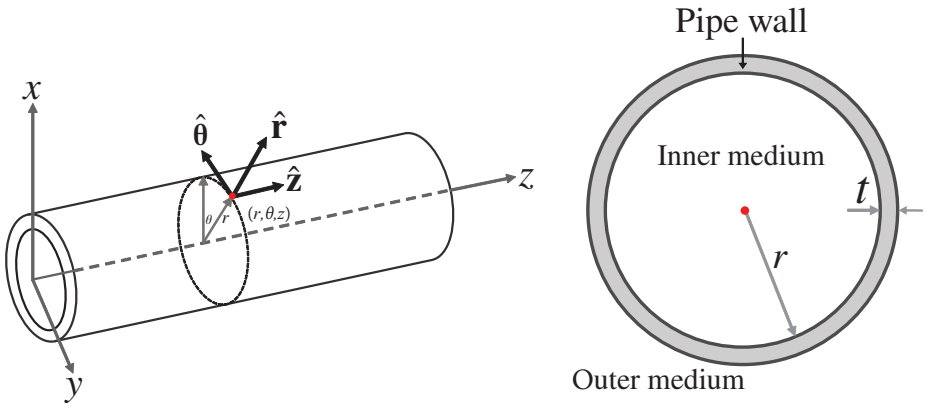

Figure 51: Hollow acoustic waveguide in cylindrical coordinate and its cross section.

pipe, the traction-free boundary condition is considered. In cylindrical coordinate as shown in Fig. 51, the Laplacian terms in (54) and (55) have the following formats,

$$\begin{cases} \nabla^2\Phi = \frac{\partial^2\Phi}{\partial r^2} + \frac{1}{r}\frac{\partial\Phi}{\partial r} + \frac{1}{r^2}\frac{\partial^2\Phi}{\partial\theta^2} + \frac{\partial^2\Phi}{\partial z^2} \\ \nabla^2\boldsymbol{\Psi} = \left(\nabla^2\Psi_r - \frac{1}{r^2}\Psi_r - 2\frac{1}{r^2}\frac{\partial\Psi_\theta}{\partial\theta}\right)\hat{\mathbf{r}} \\ + \left(\nabla^2\Psi_\theta - \frac{1}{r^2}\Psi_\theta - 2\frac{1}{r^2}\frac{\partial\Psi_r}{\partial\theta}\right)\hat{\theta} + \nabla^2\Psi_z\hat{\mathbf{z}} \end{cases} . \tag{57}$$

Combining (54), (55) and (57), Rose *et al.* presented the solutions for the scalar and vector potentials in [80] as

$$\begin{cases} \Phi = f(r)\, e^{im\theta}e^{i(kz-\omega t)} \\ \Psi_r = \psi_r(r)\, e^{im\theta}e^{i(kz-\omega t)}, m = 0, 1, 2... \\ \Psi_\theta = \psi_\theta(r)\, e^{im\theta}e^{i(kz-\omega t)} \\ \Psi_z = \psi_z(r)\, e^{im\theta}e^{i(kz-\omega t)} \end{cases} \tag{58}$$

where the integer m is known as the circumferential order of a wave mode and k is the wave number. f, ψ_r, ψ_θ and ψ_z are Bessel functions as follows:

$$f(r) = \begin{cases} A_1 J_0(|\alpha|r) + B_1 Y_0(|\alpha|r) & \omega^2/c_l^2 - k^2 \geq 0 \\ A_1 I_0(|\alpha|r) + B_1 K_0(|\alpha|r) & \omega^2/c_l^2 - k^2 < 0 \end{cases}, \tag{59}$$

$$\psi_r(r) = \begin{cases} A_2 J_1(|\alpha| r) + B_2 Y_1(|\alpha| r) & \omega^2/c_s^2 - k^2 \geq 0 \\ A_2 I_1(|\alpha| r) + B_2 K_1(|\alpha| r) & \omega^2/c_s^2 - k^2 < 0 \end{cases}, \tag{60}$$

$$\psi_\theta(r) = \begin{cases} A_3 J_1(|\alpha| r) + B_3 Y_1(|\alpha| r) & \omega^2/c_s^2 - k^2 \geq 0 \\ A_3 I_1(|\alpha| r) + B_3 K_1(|\alpha| r) & \omega^2/c_s^2 - k^2 < 0 \end{cases}, \tag{61}$$

and

$$\psi_z(r) = \begin{cases} A_4 J_0(|\alpha| r) + B_4 Y_0(|\alpha| r) & \omega^2/c_s^2 - k^2 \geq 0 \\ A_4 I_0(|\alpha| r) + B_4 K_0(|\alpha| r) & \omega^2/c_s^2 - k^2 < 0 \end{cases}. \tag{62}$$

In the above equations, (59) - (62), A_i and B_i, $i = 1, 2, 3$ and 4, are arbitrary constants. J_ν and I_ν are first kind Bessel functions, Y_ν and K_ν are second kind Bessel functions, ν is the order of Bessel function, $\alpha^2 = \frac{\omega^2}{c_l^2} - k^2$ and $\beta^2 = \frac{\omega^2}{c_s^2} - k^2$.

4.2 Stress Wave Channel Characteristics

4.2.1 Dispersion

In a wave guide such as a pipe, partial bulk wave reverberating between boundaries along the pipe. There are a bunch of wave forms with different propagation characteristics, which are known as "modes". For pipe geometry, stress waves are generally divided into three groups, namely the torsional (T), longitudinal (L) and flexural (F) waves. These modes are labeled as $L(0,\ m)$, $T(0,\ m)$ and $F(n,\ m)$, where n and m are integers. The number of modes increases as the operating frequency is exceeding the cut-off frequency which is the lowest frequency for which a mode can propagate in the pipe [76]. The propagation velocity of different modes depends on frequency, which is known as dispersion. Every mode has its cut-off frequency, dispersion characteristic and attenuation. Dispersion will cause ISI to the stress wave channel from the perspective of wireless communications.

Based on the solution of governing equation, Rose *et al.* derived the phase and group

velocities as [80]

$$\begin{cases} c_p = \omega/k \\ c_g = \frac{\partial \omega}{\partial k} \end{cases}, \tag{63}$$

where c_p and c_g are phase and group velocity, respectively. They are both the function of wave number, k. To investigate the dispersion, the open source package GUIGUW [11] is used to simulate the modes distribution. GUIGUW utilizes a Semi-Analytical Finite Element (SAFE) approach to model ultrasonic propagation in cylindrical, plate, and arbitrary cross section waveguides. Group velocities, which describe the propagating speeds of guided wave packets with components of different frequencies, are calculated by GUIGUW. They are very critical in guided wave applications as the measured velocities by transducers are usually group velocities. Group velocity dispersion curves allow us to identify guided wave modes in guided wave tests. Group velocities of different modes are calculated and shown in Fig. 52. In the simulation, the inner and outer diameters of the steel hollow pipe are set to 2 inches and 2.12 inches, respectively, so the thickness of pipe wall is 0.06 inches. The density of the steel pipe is 7800 kg/m^3. The Young's modulus of the steel at room temperature is 200 GPa.

To simplify the interpretation of the received signals in the experiment, it is desirable to excite a single mode. Especially, in a long-range communication, it is practically essential exciting a single mode to maximize the signal-to-noise ratio (SNR) and decrease the power dissipation. The group velocities give us insight into the mode distribution on the frequency spectrum. Much attention should be paid to the green curve, *i.e.*, $T(0,\ 1)$ mode. It indicates that the velocity is a constant in the entire frequency range. $T(0,\ 1)$ mode is considered as the best one as it is non-dispersive. While, $T(0,\ 1)$ is slow compared with $L(0,\ n)$ and $F(1,\ 3)$ in feasible frequency ranges. The propagation speed of $T(0,\ 1)$ mode is a limitation in high-data-rate transmission. $L(0,\ 2)$ mode at a frequency between 40 kHz to 120 kHz is an alternative one that is conducive to communication. As shown in Fig. 52, the group

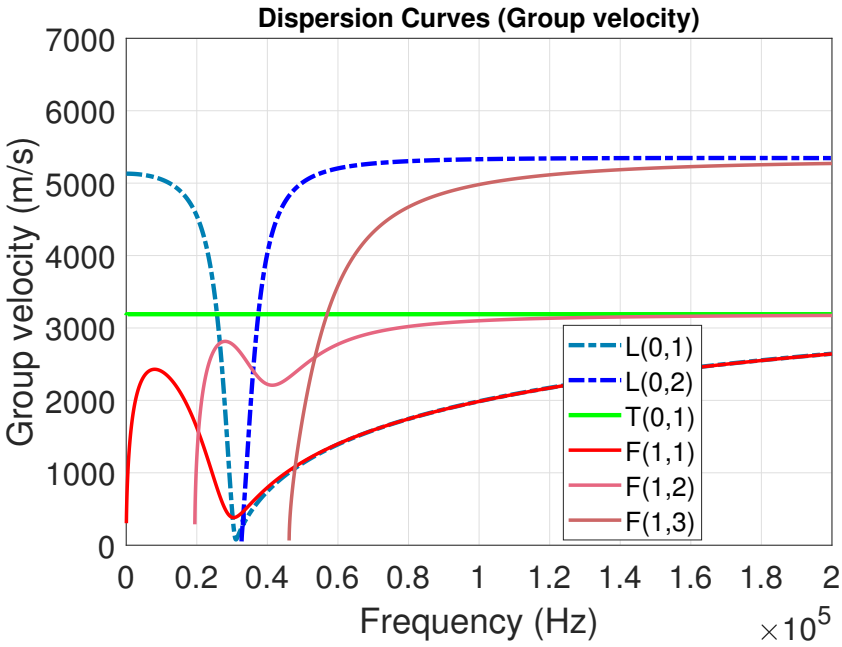

Figure 52: Group velocities vs frequency. $L(0,\ n)$ is the longitudinal mode, $T(0,\ n)$ is the transverse mode, and $\mathrm{F}(m,\ n)$ is the flexural mode. m is the order of cyclic variation, and n is a counter index.

velocity of $L(0,\ 2)$ from 40 kHz to 120 kHz is almost a constant, thus approximately non-dispersive and the mode shape remains unchanged while propagation. Furthermore, $L(0,\ 2)$ is the fastest mode among those modes coexisting in the entire frequency range. Therefore, post-processing algorithms can be applied to eliminate the undesirable slower modes.

Multimode Dispersion As shown in Fig. 52, the propagation of stress wave in a pipe exhibits different modes. Moreover, different modes propagate in different velocities. As a consequence, the delay spread of the stress wave channel is distance related. For example, according to Fig. 52, suppose the transmitted symbol was dominated by $L(0,\ 2)$ and $T(0,\ 1)$ mode. If not considering the reflection the delay spread can be estimated as

$$\tau = \frac{d}{v_T} - \frac{d}{v_L}, \tag{64}$$

where d is the distance between the transmitter and receiver, v_L and v_T are the propagation velocity of $L(0,\ 2)$ mode and $T(0,\ 1)$ mode respectively. As shown in Fig. 52, $v_L \approx 5000$ m/s

and $v_T \approx 3000$ m/s, so the delay spread for $d = 100$ m is around 13.3 ms. Such a huge delay spread implies that the symbol rate of stress wave communication must be slow to avoid the inter symbol interference (ISI).

4.2.2 Attenuation

The Navier's equation as shown in (52) does not consider the propagation loss. This means that the displacement field obtained from it will propagate without attenuation. Obviously, such a mathematical model is too ideal to be suitable for stress wave channel modeling. The main reason that (52) is lossless is that it adopts lossless medium constitutive relations that are

$$\begin{cases} \sigma_{11} = (\lambda + 2\mu)\varepsilon_{11} + \lambda\varepsilon_{22} + \lambda\varepsilon_{33} \\ \sigma_{22} = \lambda\varepsilon_{11} + (\lambda + 2\mu)\varepsilon_{22} + \lambda\varepsilon_{33} \\ \sigma_{33} = \lambda\varepsilon_{11} + \lambda\varepsilon_{22} + (\lambda + 2\mu)\varepsilon_{33} \\ \sigma_{23} = 2\mu\varepsilon_{23} \\ \sigma_{31} = 2\mu\varepsilon_{31} \\ \sigma_{12} = 2\mu\varepsilon_{12} \end{cases}, \tag{65}$$

where σ_{ij} is the stress tensor, ε_{ij} is the strain field, and i, j indicate different dimensions in different coordinate systems.

In order to model the attenuation of stress wave propagation, we need to modify (65). One way is by adding a viscous damping term. For example, we change $\sigma_{12} = 2\mu\varepsilon_{12}$ to $\sigma_{12} = 2\mu\varepsilon_{12} + \eta_{12}\frac{\partial\varepsilon_{12}}{\partial t}$, where η_{ij} can be regarded as the viscosity constant.

From the dispersion curves Fig. 52, we can see that $T(0,\ 1)$ mode does not have dispersion, and $L(0,\ 2)$ barely has dispersion when the frequency is over 60 kHz. Therefore, they are two potential modes that can be utilized for stress wave communications. Correspondingly, we will focus on the attenuation analysis of these two modes.

Attenuation of $L(0,\ 2)$ mode Since longitudinal modes do not have the tangential displacement component, we can assume the displacement fields as

$$\begin{cases} u_r = f(r)e^{i(kz-\omega t)} \\ u_\theta = 0 \\ u_z = ig(r)e^{i(kz-\omega t)} \end{cases} . \tag{66}$$

The corresponding strain and stress fields are as follows:

$$\begin{cases} \varepsilon_{rr} = f'e^{i(kz-\omega t)} \\ \varepsilon_{\theta\theta} = \frac{1}{r}fe^{i(kz-\omega t)} \\ \varepsilon_{zz} = -kge^{i(kz-\omega t)} \\ \varepsilon_{\theta z} = 0 \\ \varepsilon_{zr} = \frac{1}{2}i(kf+g')e^{i(kz-\omega t)} \\ \varepsilon_{r\theta} = 0 \end{cases} \tag{67}$$

and

$$\begin{cases} \sigma_{rr} = [(2\mu+\lambda)f' + \lambda(\frac{1}{r}f - kg)]e^{i(kz-\omega t)} \\ \sigma_{\theta\theta} = [(2\mu+\lambda)\frac{1}{r}f + \lambda(f' - kg)]e^{i(kz-\omega t)} \\ \sigma_{zz} = [-(2\mu+\lambda)kg + \lambda(f' + \frac{1}{r}f)]e^{i(kz-\omega t)} \\ \sigma_{\theta z} = 0 \\ \sigma_{zr} = i\mu(kf+g')e^{i(kz-\omega t)} \\ \sigma_{r\theta} = 0 \end{cases} . \tag{68}$$

According to the equilibrium equation $\nabla \cdot \sigma = \rho\frac{\partial^2 u}{\partial t^2}$, we have

$$g'' + \frac{1}{r}g' + \frac{\rho\omega^2 - (2\mu+\lambda)k^2}{\mu}g + \frac{k(\mu+\lambda)}{\mu}(f' + \frac{1}{r}f) = 0 \tag{69}$$

and

$$f'' + \frac{1}{r}f' - \frac{1}{r^2}f + \frac{\rho\omega^2 - \mu k^2}{\lambda+2\mu}f - \frac{k(\lambda+\mu)}{\lambda+2\mu}g' = 0. \tag{70}$$

The solution to (69), (70) yields

$$\begin{cases} f(r) = F_1 r + F_2 \frac{1}{r} \\ g(r) = G \\ \rho\omega^2 - \mu k^2 = 0 \\ kG = 2F_1 \end{cases}, \tag{71}$$

where F_1, F_2 and G are three constants, which are determined by the boundary conditions. Substituting μ for $\mu - i\omega\eta$, and k for $k + i\alpha$ in $\rho\omega^2 - \mu k^2 = 0$ yields

$$\mu(k^2 - \alpha^2) + 2\alpha k\omega\eta = \rho\omega^2 \tag{72}$$

and

$$i((k^2 - \alpha^2)\omega\eta - 2\alpha k\mu) = 0. \tag{73}$$

By solving (72), (73) we can obtain the attenuation factor α as

$$\alpha^2 = \frac{\rho\omega^2}{2\mu}\left(\sqrt{\frac{\mu^2}{\mu^2 + \omega^2\eta^2}} - \frac{\mu^2}{\mu^2 + \omega^2\eta^2}\right). \tag{74}$$

Considering $\mu \gg \omega\eta$, expression (74) reduces to

$$\alpha = \frac{\omega^2\eta}{2\mu}\sqrt{\frac{\rho}{\mu}}. \tag{75}$$

Attenuation of $T(0,\ 1)$ mode The $T(0, 1)$ mode only has the tangential displacement component. Therefore, the displacement fields are

$$\begin{cases} u_r = 0 \\ u_\theta = h(r)e^{i(kz - \omega t)} \\ u_z = 0 \end{cases}. \tag{76}$$

Following the similar procedure as previous subsection, we have

$$\mu(h'' + \frac{1}{r}h' - \frac{1}{r^2}h - k^2 h) = -\rho\omega^2 h. \tag{77}$$

Substituting μ by $\mu - i\omega\eta$, and k by $k + i\alpha$, where α is the attenuation factor, yields

$$\begin{aligned} &\mu[h'' + \frac{1}{r}h' - \frac{1}{r^2}h - (k^2 - \alpha^2)h] - 2\alpha k\omega\eta h + \rho\omega^2 h - \\ &i\left\{\omega\eta[h'' + \frac{1}{r}h' - \frac{1}{r^2}h - (k^2 - \alpha^2)h] + 2\alpha k\mu h\right\} = 0. \end{aligned} \tag{78}$$

The solution to (78) is

$$h(r) = AZ_1(\beta r) + BW_1(\beta r), \tag{79}$$

where $\beta = \sqrt{\frac{\mu\rho\omega^2}{\omega^2\eta^2+\mu^2} - (k^2 - \alpha^2)}$, Z_1 and W_1 are the first order Bessel functions. The boundary conditions are $\sigma_{r\theta} = 0$ at $r = a$ and $r = b$, where a, b are the inner and outer radius of the pipe, respectively. Since $\sigma_{r\theta} = \mu(h' + \frac{1}{r}h)e^{i(kz-\omega t)}$, we have

$$\begin{bmatrix} Z_1'(\beta a) - \frac{Z_1(\beta a)}{a} & W_1'(\beta a) - \frac{W_1(\beta a)}{a} \\ Z_1'(\beta b) - \frac{Z_1(\beta b)}{b} & W_1'(\beta b) - \frac{W_1(\beta b)}{b} \end{bmatrix} \begin{bmatrix} A \\ B \end{bmatrix} = 0. \tag{80}$$

By solving (80), we can obtain β. Finally, we can solve the wave number k, and attenuation factor α as follows:

$$k^2 - \alpha^2 = \frac{\mu\rho\omega^2}{\omega^2\eta^2 + \mu^2} - \beta^2 \tag{81}$$

and

$$2\alpha k = \frac{\eta\rho\omega^3}{\omega^2\eta^2 + \mu^2}. \tag{82}$$

By eliminating k from (81) and (82), we obtain

$$2\alpha^2 = \frac{1}{2}\frac{(\eta\rho\omega^3)^2}{(\mu^2 + \eta^2\omega^2)(\mu\rho\omega^2 - \beta^2(\mu^2 + \eta^2\omega^2))}. \tag{83}$$

Considering $\rho\omega^2 \gg \mu \gg \omega\eta$ and $\beta \approx 1$, expression (83) reduces to

$$\alpha = \frac{\omega^2\eta}{2\mu}\sqrt{\frac{\rho}{\mu}}. \tag{84}$$

Comparing (75) with (84) reveals that longitudinal modes and torsional modes share the same attenuation rate which is proportional to the square of the frequency.

Path Loss Since stress wave only propagates along the pipe, it does not suffer from geometry spreading loss. The stress wave channel path loss only determined by the attenuation factor α, and can be calculated as

$$PL\ (dB/meter) = 20(\log e)\alpha \approx 8.686\alpha. \tag{85}$$

Combining (84) and (85) we can evaluate the path loss of the stress wave channel. The typical value of shear modular μ of steels is in the order of 10, *e.g.*, 8.24×10^{10} newtons/m^2. β is approximately equal to 1, which is determined by the inner and outer radius of the pipe. The density of stainless steel is around 7850 kg/m^3. The only uncertain parameter in (84) is the viscosity constant used to model the propagation loss of stress wave. Suppose η is around 1, then the path loss of stress wave is approximately equal to 0.006 dB/m if the operation frequency is 100 kHz. The path loss under different viscosity η is shown in fig. 53.

We can also estimate the frequency dependent attenuation (FDA) characteristics based on (84). The attenuation between two frequencies f_1 and $f_2 > f_1$ can be calculated by $e^{-\gamma(f_1-f_2)}$, where $\gamma = 4\pi^2 d\frac{\eta}{\mu}\sqrt{\frac{\rho}{\mu}}f_c$, d is the transmission distance, and $f_c = \frac{f_2+f_1}{2}$ is the carrier frequency. Similarly, the FDA can be estimated by

$$\text{FDA}\ (dB/Hz) = 20(\log_{10} e)\gamma \approx 8.686\gamma. \tag{86}$$

The path loss and FDA curves of the stress wave channel are plotted in Fig. 53. Generally speaking, the viscosity constant of metals is a small number, $\eta \ll 1$. Therefore,

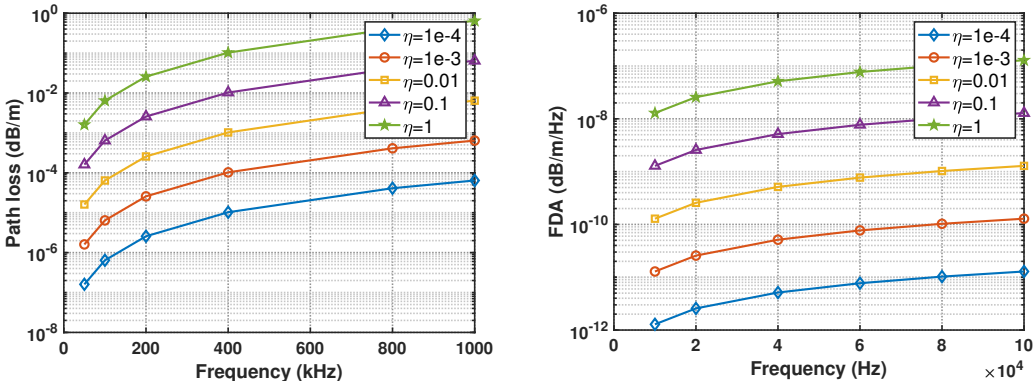

(a) Path loss (b) Frequency-dependent attenuation

Figure 53: Path loss and frequency-dependent attenuation of the stress wave channel.

the propagation loss of the stress wave along a hollow cylindrical pipe would be extremely small. From this point of view, the stress wave channel of a pipe with infinite length can be regarded as a flat fading channel if the operation frequency is under MHz level.

4.2.3 Multipath

The propagation of stress wave along a pipe will suffer from strong reflections from both ends of the pipe. As shown in Fig. 54 the propagation delay of each reflection path can be determined by the length of the pipe and the position of transmitter and receiver. If we only consider the first reflection from both ends, path 5 would be the longest path which is 265 inch. Since the propagation velocity of $T(0,\ 1)$ mode is 3.2 km/s, the propagation delay would be 2.1 ms.

The channel response can be estimated by transmitting pilot symbols denoted as $\mathbf{t}[n]$.

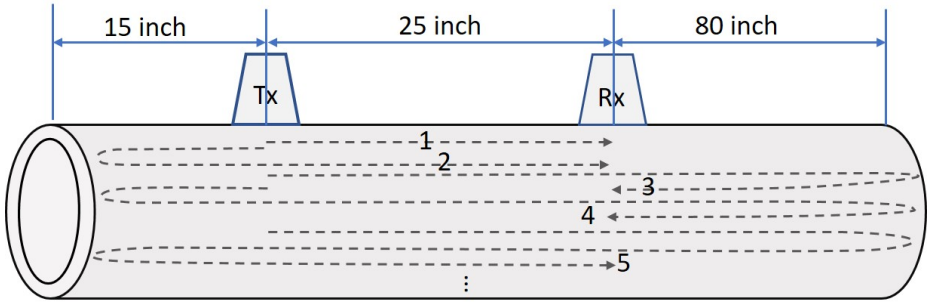

Figure 54: Reflections of the stress wave along a pipe.

Suppose the channel impulse response is $\mathbf{h}[m]$. Then the received symbols denoted as $\mathbf{r}[n]$ is

$$\mathbf{r} = \mathbf{t} * \mathbf{h}. \tag{87}$$

The matrix form of (87) is

$$\mathbf{r} = \mathbf{T}\mathbf{h}, \tag{88}$$

where, $\mathbf{T}$ is the transmission matrix as

$$\mathbf{T} = \begin{bmatrix} \mathbf{t}[0] & \mathbf{t}[-1] & \cdots & \mathbf{t}[1-m] \\ \mathbf{t}[1] & \mathbf{t}[0] & \cdots & \mathbf{t}[2-m] \\ \vdots & \vdots & \vdots & \vdots \\ \mathbf{t}[n-1] & \mathbf{t}[n-2] & \cdots & \mathbf{t}[n-m] \end{bmatrix}. \tag{89}$$

The number of transmitted pilot symbols n is normally much larger than the number of taps of channel impulse response m. Therefore, we can apply least square method to solve (88) and the solution can be expressed as

$$\mathbf{h} = (\mathbf{T}^{\mathsf{T}}\mathbf{T})^{-1}\mathbf{T}^{\mathsf{T}}\mathbf{r}. \tag{90}$$

In our experiments, the pilot symbols were modulated by BPSK, the amplitude of which is either 1 or -1. Before we apply (90), we need to obtain the received symbol vector $\mathbf{r}$. The corresponding signal processing process is shown as in Fig. 55.

Figure 55: Received symbol determination process.

The transmitted symbols and the corresponding received symbols are shown in Fig. 56 (a). The symbol rate of the experiment is 1 kBd (1000 sps), which means the symbol period is 1ms. According to our previous analysis, the propagation delay is around 2.1 ms, which implies that the current symbol may be contaminated by its previous three symbols.

Therefore, the channel response can be expected as a four tap FIR filter, which is verified by the experiment result as shown in Fig. 56 (b).

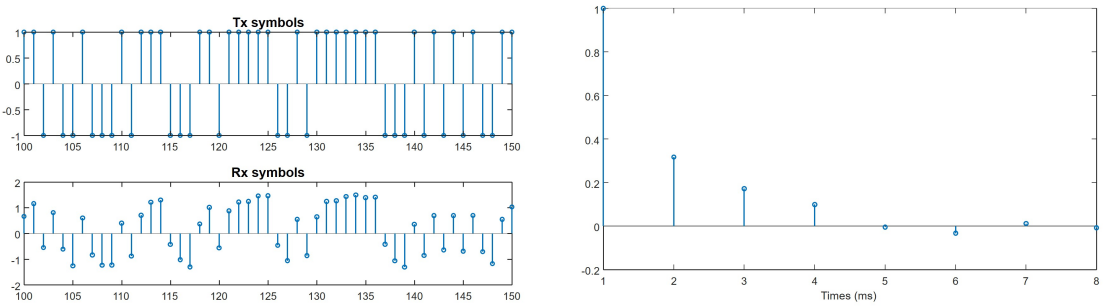

(a) Transmitted and received symbols

(b) Channel response

Figure 56: Channel response of the stress wave channel.

4.3 Laboratory Experiments

Although the theoretical analysis suggests that the single mode stress wave channel of a infinite length pipe can be treated as a flatting fading channel, a finite length pipe will suffer from strong distortion caused by the reflection from both ends as well as multi-mode dispersion. Moreover, the piezoelectric transducer that converses electrics signal into pressure or stress is quite frequency selective. Therefore, the practical stress wave channel would be much more complicated. In this section, we will first set up a stress wave testbed. Then we will measure the practical stress wave channel response. Finally, we will evaluate the practical stress wave communication performances.

4.3.1 Stress Wave Communication Testbed

The testbed is build on two galvanized steel pipes with length of 10 feet and diameter of 2 inch. The pipes are weld together to form a "T" shape, such that we can investigate the reflection when the stress wave propagates through a joint. The piezoelectric transducer was applied on the surface of the pipe for the conversion between electric signals and mechanical vibrations. The transmitted signal is generated by a signal generator (Keysight 33500B) while the received signal is captured and recored by a oscilloscope (Keysight MSOS604).

The schematic of the testbed and real testbed are shown in Fig. 57, 58. Before we can apply any wireless communion schemes, we need to figure out the available bandwidth of the aforementioned testbed. We will first design an appropriate OFDM training symbol sequence to estimate the frequency response. Then, we will evaluate the real stress wave communication performances both in the air and in the underwater environments.

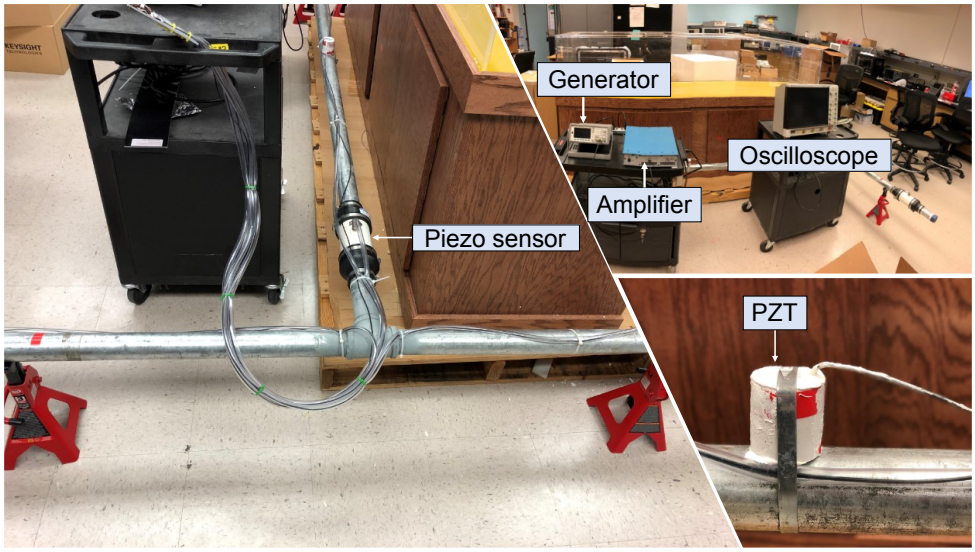

Figure 57: Lab testbed of stress wave communication.

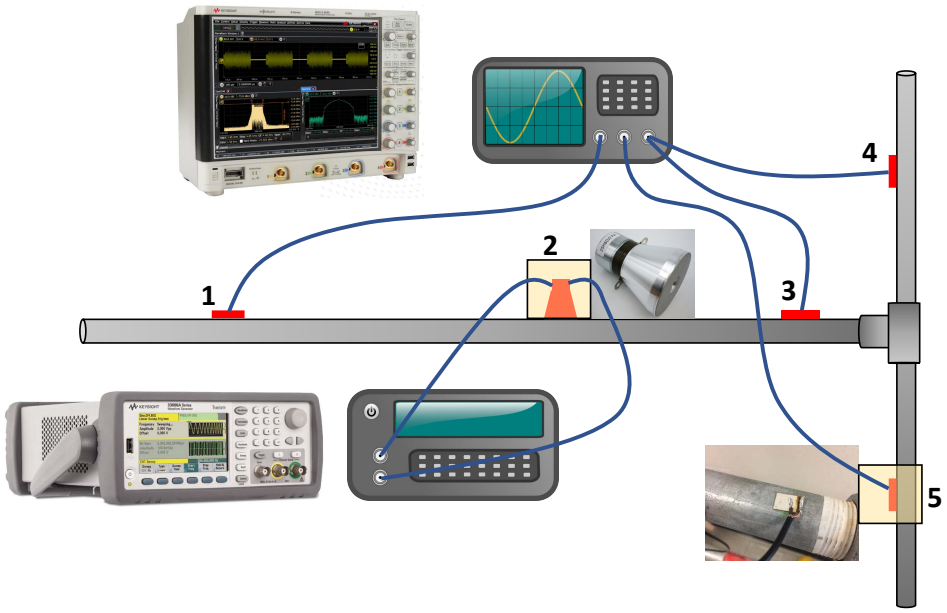

Figure 58: Schematic of the Lab Testbed.

4.3.2 Transducer Characteristics

PZT, or lead zirconate titanate, is one of the world's most widely used piezoelectric ceramic materials. PZTs have strong piezoelectric effect which is the ability to generate electric charge in response to applied mechanical stress. Therefore, the PZT transducer has been widely used as an stress wave actuator or sensor in the field of structure health monitoring [53, 42, 39, 113]. In this paper, we also use PZT transducers to generate and detect stress waves. There are two different types of the PZT transducer used in our testbed as shown in Fig. 57. Node 5 shows a single patch PZT transducer. Node 2 shows a PZT stack with multiple layer of PZT materials, which have much higher output power capability in comparison with the single PZT patch. Actually, the system operation frequency and the available bandwidth are highly related to the frequency response of the PZT transducer.

Carazo *et al.* discussed the piezoelectric transducer in detail in [103]. A equivalent circuit model, including the effects of the sensor's mechanical construction and other non-idealities, is shown in Fig. 59. The inductance L_m is due to the seismic mass of the sensor itself. C_e is inversely proportional to the mechanical elasticity of the piezo material. C_0 denotes the static capacitance of the transducer, resulting from stack structure. R_i is the input resistance of the transducer element. By tuning L_m, C_e, C_0 and impedance matching, the resonance can be established and thus maximize the energy transfer efficiency.

The resonant equivalent circuit of the PZT sensor implies that the frequency response would be quite frequency selective. The input impedance of the transducer is measured as

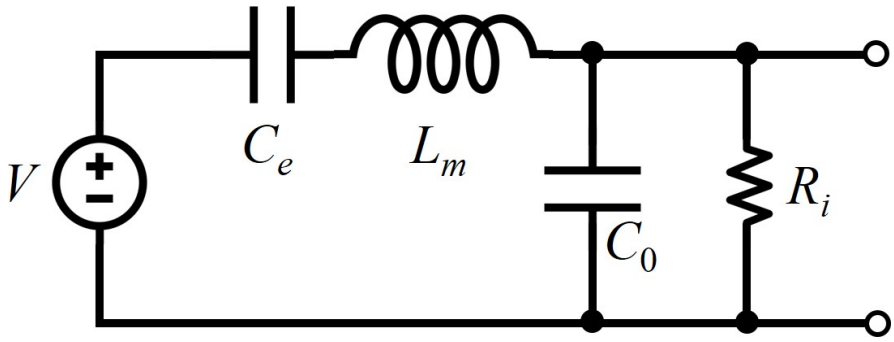

Figure 59: Equivalent circuit model of piezoelectric transducer.

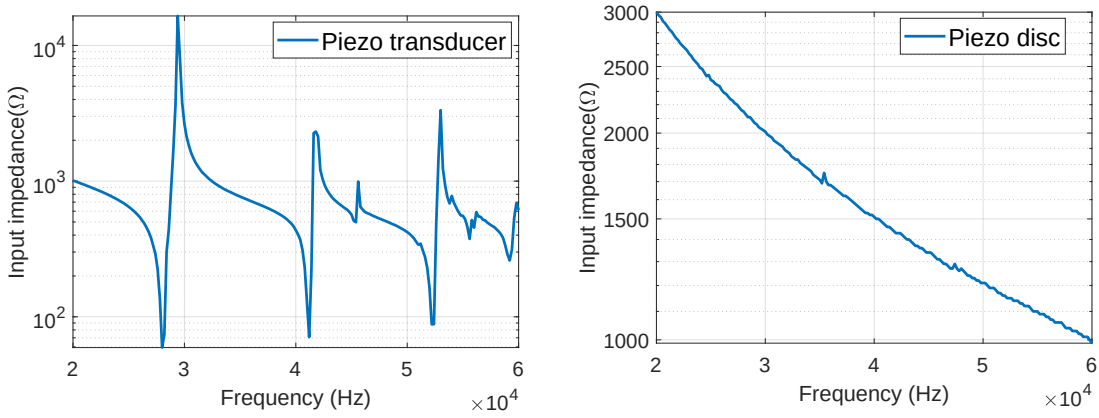

(a) PZT stack (b) PZT disc

Figure 60: Input impedance of piezoelectric elements.

shown in Fig. 60. In Fig. 60 (a), multiple peaks are observed, while Fig. 60 (b) is smooth with no peak present. The smaller impedance means the higher energy transfer efficiency.

4.3.3 Experiment Results

We first experiment to verify the linear time-invariant (LTI) property of the system. In this experiment, we transmit two tones at different center frequencies simultaneously from the transmitter PZT. An oscilloscope has been utilized to record and analyze the signal from the receiver PZT. Subsequently, We perform FFT amplitude analysis. The result is shown in Fig. 61. The frequency of the received signal, which is converted from stress wave generated by transducer PZT, is the same as the input. What is more, PZT transducers along with stress wave propagation over the pipeline is a linear channel since it follows scaling and additivity properties. As a result, such a linear channel enables various linear modulation schemes like BPSK, QPSK, QAM, OFDM, *etc.* A channel frequency response (CFR) estimator based on the OFDM training symbol has been developed to estimate frequency response using the basic least square algorithm (LS). The formula is the same as (89). However, in this case, the matrix $\mathbf{T}$ is a diagonal matrix, whose every diagonal element is a modulated symbol for its corresponding subcarrier.

We investigate the stress wave channel by transmitting OFDM symbols, whose duration is 10 ms, and the sampling rate is 1 MHz. Notice that these OFDM parameters are specially

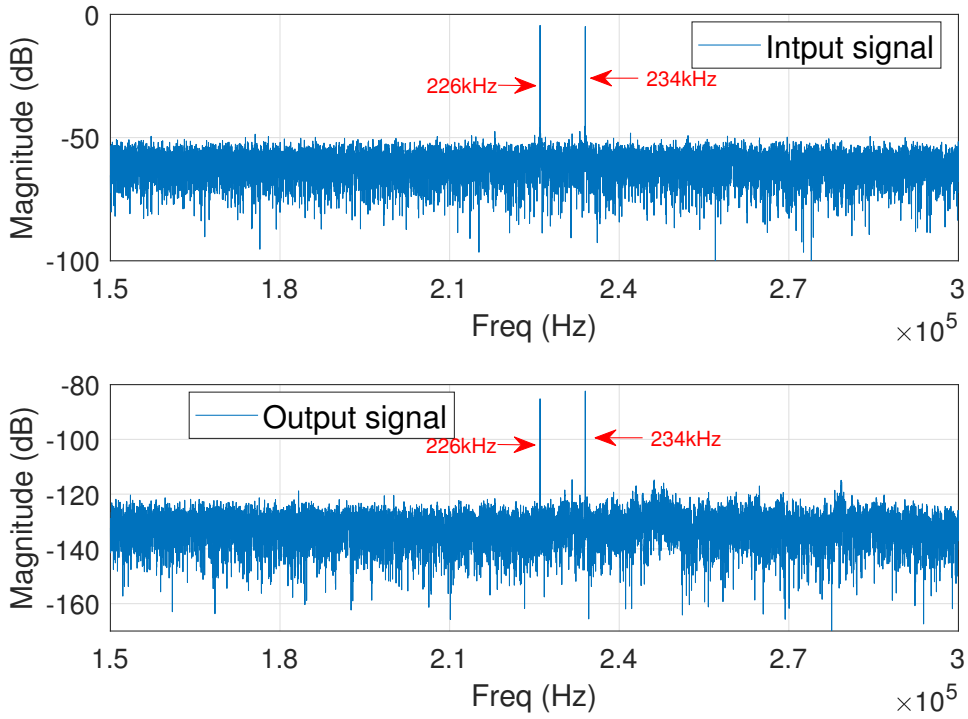

Figure 61: Absolute value of the Fourier transform of the amplitude when transmitting two sinusoidal signals simultaneously at 226 kHz and 234 kHz, respectively.

designed to test the stress wave channel properties, so we adopt the narrow subcarrier spacing of 100 Hz to obtain the high frequency resolution to precisely reflect the real stress wave channel. The cyclic prefix (CP), as the guard interval, is expected to compensate for the delay spread. In this case, we set the CP length to be 2 ms based on the fact that the theoretical delay spread is 2.1 ms. The experimental channel impulse response also suggests that the delay spread should be between 2 to 3 ms. In addition, we apply the robust QPSK modulation scheme to each subcarrier, which can tolerate a significant amount of noise (normally 12 dB SNR for 0.1% BER) for precise channel estimation. Using the parameters above, we finally show the frequency response in Fig. 62, whose bandwidth of interest is from 10 kHz to 230 kHz. It needs to be pointed out that, although we use a conservative 100 Hz subcarrier spacing to extract the channel information, large subcarrier spacing such as 500 Hz is acceptable during channel estimation and data transmission. As a result, each subcarrier channel may be less "flat" but the symbol duration and the number of Fast

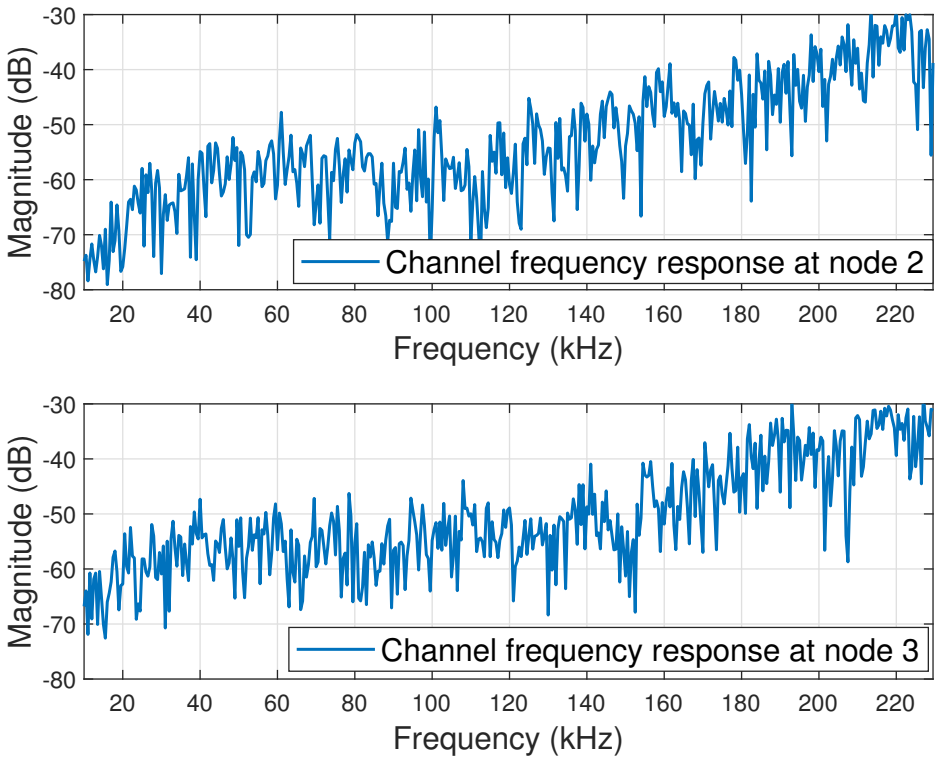

Figure 62: Frequency responses of the stress wave testbed.

Fourier Transform will decrease. We can derive two important conclusions from Fig. 62. First, channel frequency response follows the trend of the frequency response of the PZT transducer as shown in Fig. 60 (b) since higher frequency has higher energy conversion efficiency. Second, the frequency responses periodically experience some peak and trough, which is mainly due to the multimode and multipath propagation of the stress wave along a finite-length pipe. Specifically, if all the reflected waves are in phase with the original wave, we will observe a peak on the amplitude frequency response curve. On the other hand, the superposition of all the reflected waves and the original wave may cancel out with each other at some positions, which results in a trough on the amplitude frequency response curve.

To demonstrate the effectiveness of OFDM for stress wave communications, we choose 18 subcarriers based on Fig. 62 and perform 16-QAM for each subcarrier. The CP length is set to 2 ms to avoid the ISI, and the symbol duration is set to 10 ms (much greater than the CP length to increase the time efficiency). The received signal and the demodulation results

at node 3 are shown in Fig. 63 and Fig. 64, respectively. The overall data transmission rate is $\frac{1}{12} \times 4 \times 18 = 6$ kbps.

Figure 63: Transmitted and received OFDM symbols.

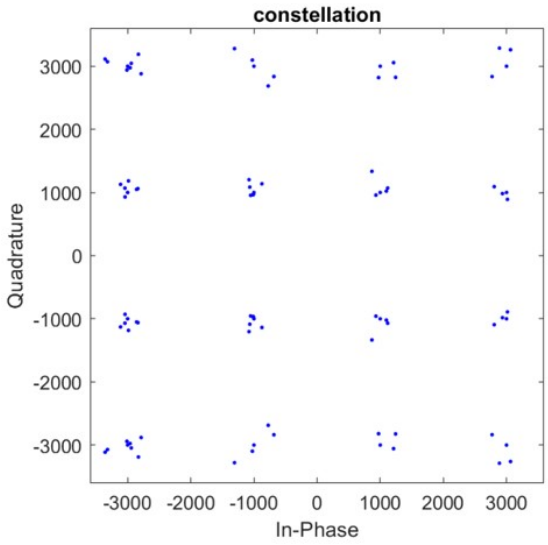

Figure 64: OFDM demodulation results.

We also transmitted some QPSK symbols at node 2 and demodulate the received signal at node 1, 3, 4, and 5 to evaluate the stress wave communication performances. We use a PZT stack as the transmission transducer with self resonant frequency of 40 kHz. The PZT patches were attached to the surface of the pipe as receiving nodes.

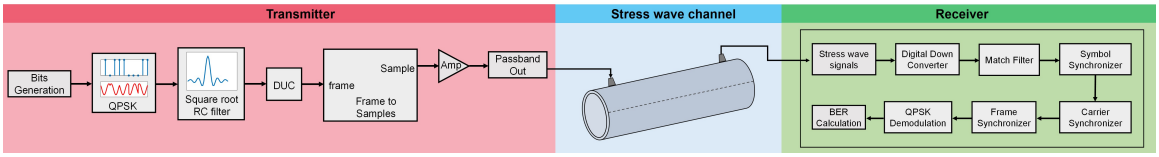

Figure 65: Block diagram of the stress wireless communication system.

The signal processing block diagram is shown in Fig. 65. Where the DUC stands for digital up converter which convert the baseband signals to passband signals with center frequency of 40 kHz. The transmission symbol rate is 1380 symbols per second. The demodulation results in the lab are shown in Fig. 67. It is shown that the BER increased dramatically after stress wave signals propagating through a join between node 3 and node 4. This is mainly due to the reflection. Specifically, when stress wave signals propagates from one pipe to another pipe, due to the impedance mismatch in the join, most of the stress wave signals will be reflected back. For this reason, the SNR on node 4 would be much lower than node 3 resulting in a worse BER performance.

The subsea experiment setup is shown in Fig. 66. We directly submerged the testbed into the sea water. Then we repeated the same testing procedure as what we did in the lab. The testing results are shown in Fig. 68. It turned out that the subsea performances were much better than the lab testing results. Specifically, the error vector magnitude (EVM) in the underwater environment is much smaller than in the lab. To analyze the possible reasons, we show the received signal spectrum in Fig. 69.

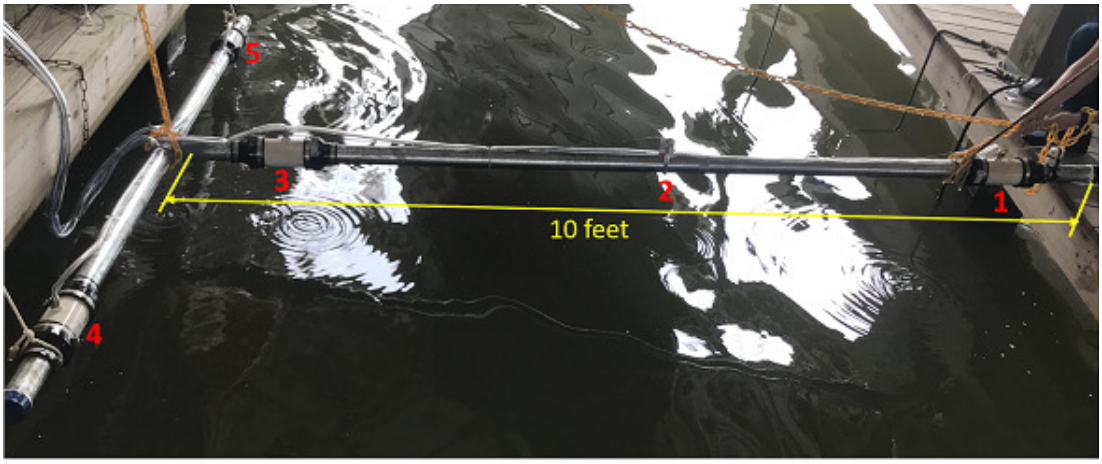

Figure 66: Subsea testing setup.

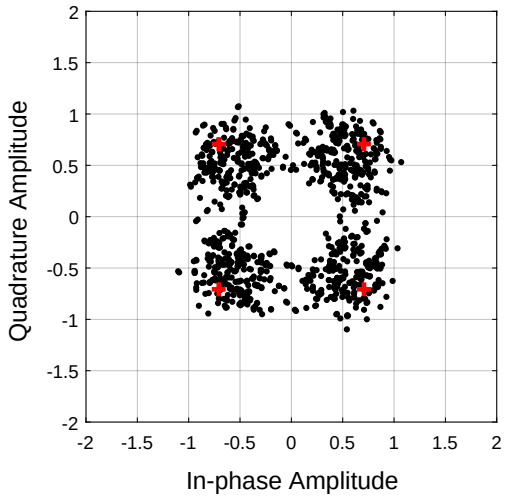

(a) Demodulation results at node 3, BER=0.0783 @ symbol rate = 1380 Bd

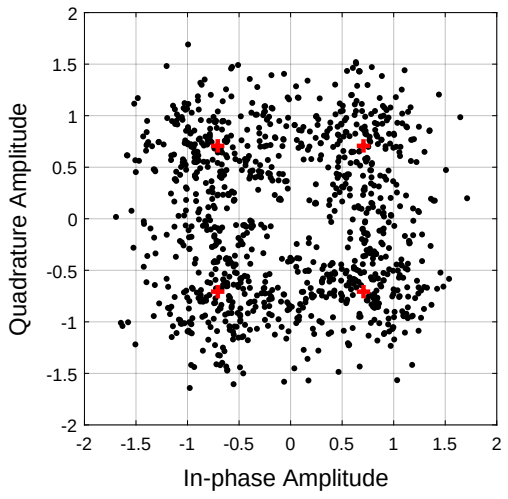

(b) Demodulation results at node 4, BER=0.2366 @ symbol rate = 1380 Bd

Figure 67: Demodulation results in the lab.

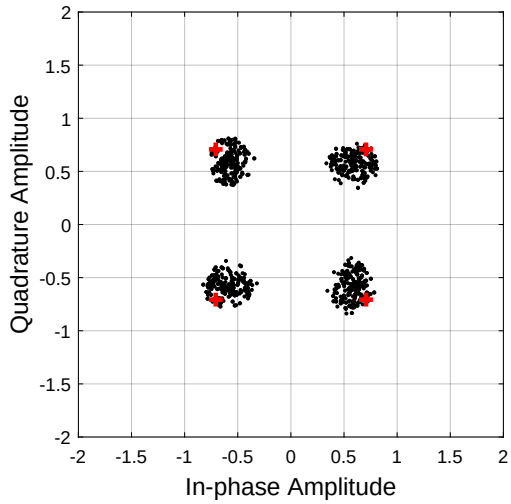

(a) Demodulation results on node 3, BER=0 @ symbol rate = 1380 Bd

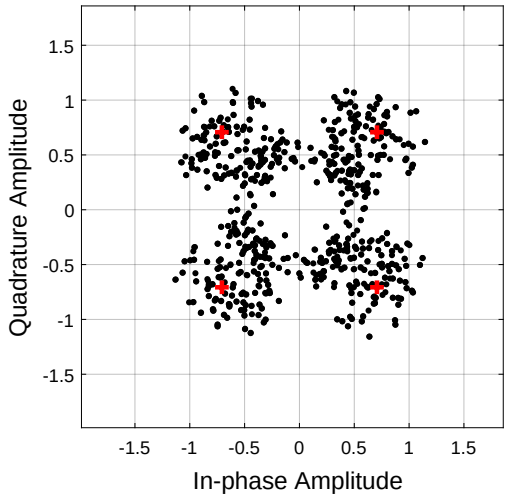

(b) Demodulation results on node 4, BER=0.1127 @ symbol rate = 1380 Bd

Figure 68: Demodulation results subsea.

The noise in the lab is several dB higher than subsea at node 4, if we scale the signal strength to the same level. One possible reason could be that the electromagnetic environment in the lab is much more complicated than the subsea environment. The PZT transducer could also act like an EM antenna that may induced some noise into the system.

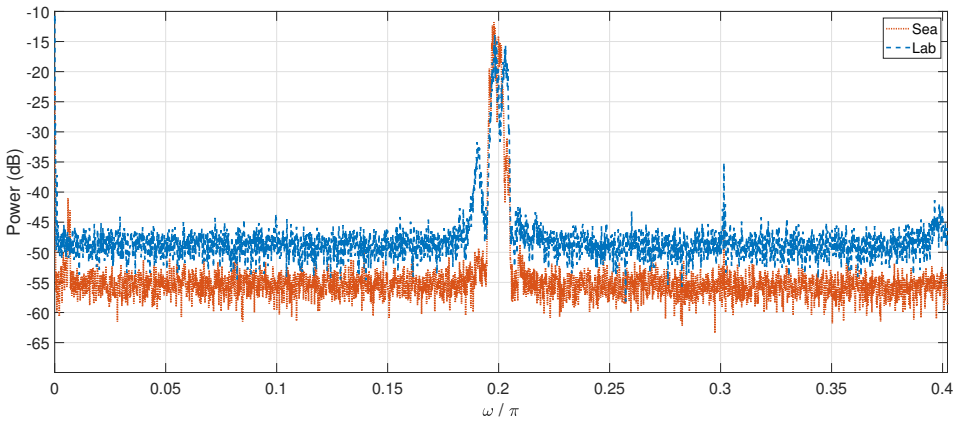

(a) Node 4

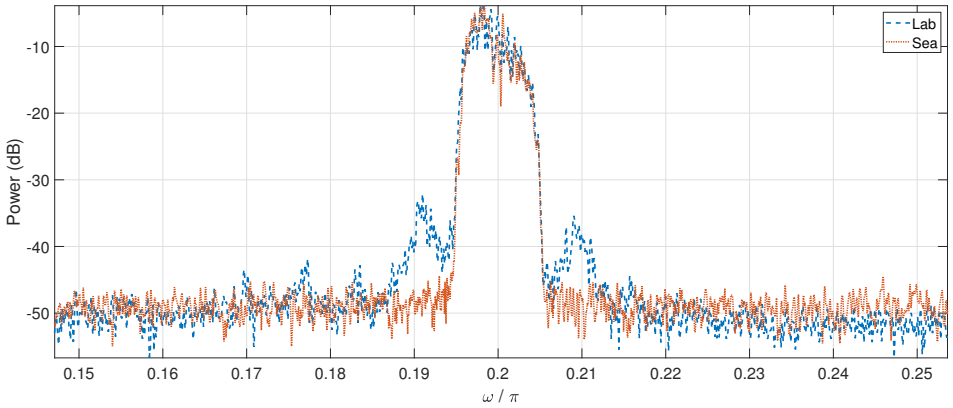

(b) Node 3

Figure 69: Power spectrum of the received signal at node 3 and node 4.

On the other hand, EM waves almost cannot propagate in the sea water. Hence, the subsea EM environment is much more clean than in the lab. Therefore, the SNR of the subsea stress wave signal could be higher than the one in the lab, especially when the received signal is weak.

The noise power at note 3 is quite similar both in the lab or subsea. But there are significant side lobes in the lab environment. One possible reason is that the stress wave reflection in the underwater testbed could be different from the lab testbed. So the channel frequency response would be different. Since subsea performances is better and the power spectrum is smoother than that in the lab, the reflection in the underwater environment may be smaller than in the air.

5 Underwater Hybrid Networking

Underwater acoustic communication is good at long-range data transmission but has limited data rate. With the assistance of AUVs, high-efficiency high-data rate wireless communications such as underwater MI and optical communications can be utilized for short-range data collection. Therefore, combining different types of underwater wireless communication technologies, we could achieve more power-efficient underwater sensor networks. However, due to cost there are many sensor nodes but few AUVs, so it is impractical for AUVs to directly collect data from all the sensor nodes. Different data collection strategies will have significant impacts to the overall network performances. In this section, we investigate a AUV data collection strategy for maximizing the network lifetime of Underwater MI Acoustic hybrid sensor networks.

There exist different definitions for network lifetime [20], *e.g.*, when the first node is drained of its energy, when the first cluster head is drained of its energy, when the fraction of surviving nodes drops below a threshold. In this paper, we define the network lifetime as the time when the first node is drained of its energy, considering that the underwater sensor nodes may be loosely deployed and every node is important for the network. Also, through optimal network flow routing, the energy consumption of all sensor nodes can be balanced.

5.1 System Model of MI-Acoustic Hybrid Underwater Wireless Sensor Networking

The system under consideration is a static two dimensional UWSN on the sea floor (Fig. 70). The sensor nodes can forward their data among each other through long range acoustic communications. The AUV periodically visits a subset of the sensor nodes to collect the sensing data through high-efficiency MI wireless communications. The key challenge is that the travel distance of an AUV is limited. Hence it can only visit a small subset of the sensors in the network, which are denoted as anchor nodes. Suppose that during each round the AUV must collect all the sensing data of the whole network. Then all the sensing data must

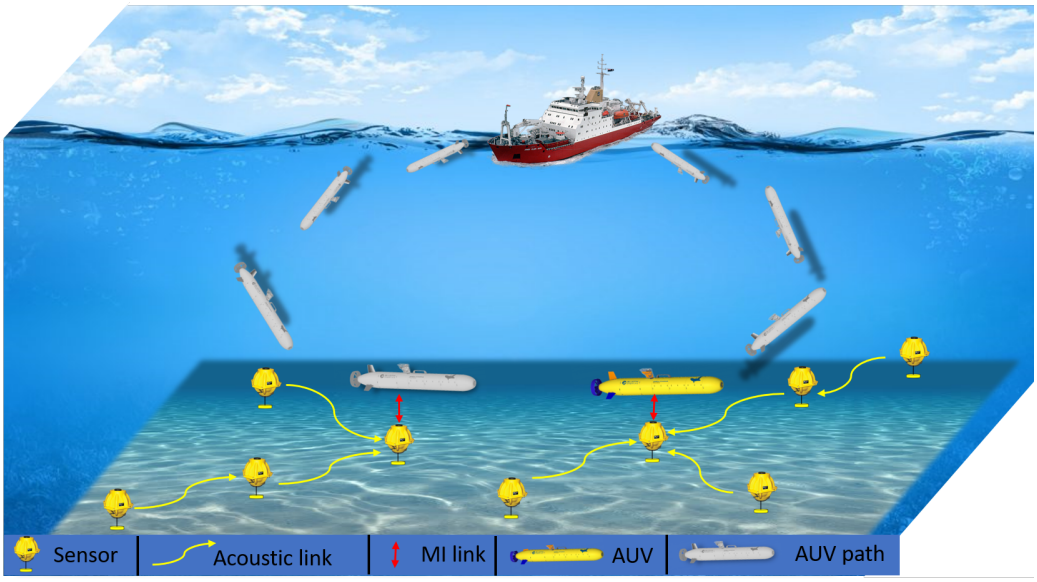

Figure 70: MI-Acoustic hybrid underwater wireless sensor network.

be forwarded to the anchor nodes through one-hop or multi-hop acoustic communications. The challenge is to determine which sensor nodes need to be selected each round as anchor nodes such that the network lifetime can be maximized.

Such kind of a problem can be formulated as a MILP model to determined the optimal multi-hop routing among sensor nodes and the optimal anchor nodes selection. The variables used in the problem formulation are given in Table 6. According to different networking settings and different metrics of network lifetime, we can have different mathematical formulations.

5.2 Static Anchor Nodes Model

In this model, we have a set of deterministic anchor nodes. Normally, these anchor nodes are evenly distributed in the target sensing area. An AUV will periodically visit these anchor nodes as an data mule to gather the sensing data. All the sensor nodes will forward their sensing data to its nearby anchor nodes through multi-hop communication. The optimization problem of the minimum energy consumption of each AUV data collection

Table 6: Notation of the variables used in mathematical formulation.

Symbol	Definition
$\mathcal{N}$	Set of sensor nodes
$\mathcal{A}$	set of anchor nodes
$\mathcal{E}$	Set of acoustic links
$\mathcal{K}$	Set of pipelines leveraged as stress wave links
d_{ij}	Distance between node i and node j
$f_{ij}(f_e)$	Data flow rate from node i to node j
$\epsilon_{ij}(\epsilon_e)$	Energy required to transmit 1 bit from node i to j
γ	Energy required to receive 1 bit through acoustic
μ	Energy required to transmit 1 bit through MI
g_i	Data generation rate of node i
E_i	Initicial battery energy of node i
ρ_i	Round energy consumption of node i

circle is formulated as

$$\min_{f_e} \quad \sum_{e\in\mathcal{E}} f_e(\epsilon_e+\gamma) \tag{91a}$$

$$\text{s.t.} \quad \sum_{j\in\mathcal{N}} f_{ij} = \sum_{k\in\mathcal{N}} f_{ki} + g_i \quad \forall i \in \mathcal{N}-\mathcal{A}, \tag{91b}$$

$$f_{ij} = 0 \qquad \forall i \in \mathcal{A}, \forall j \in \mathcal{N}, \tag{91c}$$

$$f_{ij} \geq 0 \qquad \forall i \in \mathcal{N}-\mathcal{A}, \forall j \in \mathcal{N}. \tag{91d}$$

5.2.1 Minimize Overall Acoustic Energy Consumption

The objective function of (91) only considers the acoustic communication energy consumption, since the MI communications at the anchor nodes will not affect the acoustic multi-hop routing. The flow conservation condition (91b) states that, for normal sensing node, the sum of the incoming data and its own generating data should be equal to the outgoing data. Constraint (91c) states that for anchor nodes, the outgoing data should be zero, since their data will be collected by the AUV through MI links.

Formulation (91) is a greedy method. It tries to use the minimum energy to deliver the sensing data of the whole network, which may result in an unfair battery depletion rates. In other worlds, some sensor nodes may deplete their battery more quickly than the others. This might not be a problem in some application scenarios where the failure of one or few sensor nodes will not affect the network performances. However, in some scenarios all sensor nodes are important. Especially in underwater environments the deployment of every sensor node is difficult and expensive. Therefore, if the balancing of battery depletion rate is important we can use the following problem formulation.

5.2.2 Minimize the Maximum Energy Consumption over All Sensor Nodes

Suppose E_j is the residual battery power of node j at the beginning of each data collection period. ρ_j is the energy consumption during the period, which is due to the acoustic or MI transmission and reception. Then the residual battery power at the end of the collection period would be $E_j - \rho_j$. So the objective could be maximizing the minimum residual battery power of all sensor nodes, which yields

$$\max \quad \min_{j \in \mathcal{N}} \ (E_j - \rho_j) \tag{92a}$$

$$\text{s.t.} \quad \sum_{j \in \mathcal{N}} f_{ij} = \sum_{k \in \mathcal{N}-\mathcal{A}} f_{ki} + g_i \qquad \forall i \in \mathcal{N} - \mathcal{A}, \tag{92b}$$

$$m_i = \sum_{k \in \mathcal{N}-\mathcal{A}} f_{ki} + g_i \qquad \forall i \in \mathcal{A}, \tag{92c}$$

$$\rho_i = \sum_{j \in \mathcal{N}} f_{ij}\epsilon_{ij} + \sum_{k \in \mathcal{N}-\mathcal{A}} f_{ki}\gamma_{ki} \quad \forall i \in \mathcal{N} - \mathcal{A}, \tag{92d}$$

$$\rho_i = \sum_{k \in \mathcal{N}-\mathcal{A}} f_{ki}\gamma_{ij} + \mu m_i \quad \forall i \in \mathcal{A}, \tag{92e}$$

$$\rho_j \leq E_j \qquad \forall j \in \mathcal{N}, \tag{92f}$$

$$f_{ij} = 0 \qquad \forall i \in \mathcal{A}, \forall j \in \mathcal{N}, \tag{92g}$$

$$f_{ij} \geq 0 \qquad \forall i \in \mathcal{N} - \mathcal{A}, \forall j \in \mathcal{N}, \tag{92h}$$

$$m_i \geq 0 \qquad \forall i \in \mathcal{A}. \tag{92i}$$

Constraints (92b), (92c),(92g) and (92h) have similar interpretation as in the previous case. Constraint (92f) stipulates that the total energy consumption of each node during one data collection circle should not exceed the available battery power.

The only nonlinear term in (92) is the objective function. By introducing an additional variable $z \leq E_j - \rho_j$, the minimax problem can be alternatively expressed by maximizing z as

$$\max \quad z \tag{93a}$$

$$\text{s.t.} \quad \sum_{j\in\mathcal{N}} f_{ij} = \sum_{k\in\mathcal{N}-\mathcal{A}} f_{ki} + g_i \qquad \forall i \in \mathcal{N} - \mathcal{A}, \tag{93b}$$

$$m_i = \sum_{k\in\mathcal{N}-\mathcal{A}} f_{ki} + g_i \qquad \forall i \in \mathcal{A}, \tag{93c}$$

$$\rho_i = \sum_{j\in\mathcal{N}} f_{ij}\epsilon_{ij} + \sum_{k\in\mathcal{N}-\mathcal{A}} f_{ki}\gamma_{ki} \quad \forall i \in \mathcal{N} - \mathcal{A}, \tag{93d}$$

$$\rho_i = \sum_{k\in\mathcal{N}-\mathcal{A}} f_{ki}\gamma_{ij} + \mu m_i \quad \forall i \in \mathcal{A}, \tag{93e}$$

$$z \leq E_j - \rho_j \qquad \forall j \in \mathcal{N}, \tag{93f}$$

$$f_{ij} = 0 \qquad \forall i \in \mathcal{A}, \forall j \in \mathcal{N}, \tag{93g}$$

$$f_{ij} \geq 0 \qquad \forall i \in \mathcal{N} - \mathcal{A}, \forall j \in \mathcal{N}, \tag{93h}$$

$$m_i \geq 0 \qquad \forall i \in \mathcal{A}. \tag{93i}$$

5.3 Dynamic Anchor Nodes Model

In previous models anchor nodes are pre-selected which can simplify the optimum flow routing problem and reduce the computational complexity. However, in some scenarios every sensor node can be potentially chosen as an anchor node. Furthermore, the anchor nodes in different data gathering rounds could be different. Therefore, anchor nodes selection could be very complicated. Next, let us handle the dynamic anchor nodes selection problem.

5.3.1 Battery Power Based Anchor Nodes Selection (BPBANS)

Considering that the anchor nodes do not need to transmit data through acoustic communications, the power consumption may be smaller than the normal nodes. Therefore, the anchor node selection may be based on the current battery residual energy of all the sensor nodes. The specific steps for anchor nodes selection are as follows. First, select k sensor nodes with the lest battery residue energy as candidate anchor nodes. Second, calculate the shortest path χ that passing through all the candidate anchor nodes once, which is typically a traveling salesmen problem (TSP). Third, compare χ with the maximum AUV traveling distance X. If $\chi > X$ reduce $k = k - 1$, otherwise increase $k = k + 1$. Finally, based on $\chi(k)$ and $\chi(k+1)$ we can determine the maximum number of anchor nodes with the lowest battery energy level. The details of the minimum battery residue energy anchor nodes selection policy are summarized in Algorithm 1.

The shortest path calculation between k candidate nodes is the typical TSP, which can be solved by Miller–Tucker–Zemlin formulation as

$$\min \quad \sum_{i=0}^{k}\sum_{j=0}^{k} d_{ij}x_{i,j} \tag{94a}$$

$$\text{s.t.} \quad \sum_{i=1,i\neq j} x_{ij} = 1 \qquad \forall j = 0,\cdots,k, \tag{94b}$$

$$\sum_{j=1,i\neq j} x_{ij} = 1 \qquad \forall i = 0,\cdots,k, \tag{94c}$$

$$u_i + 1 \leq u_j + k(1 - x_{i,j}) \qquad \forall i,j = 1,\cdots,k, \quad i \neq j, \tag{94d}$$

$$x_{ij} \in \{0,1\} \qquad \forall i,j = 1,\cdots,k, \quad i \neq j, \tag{94e}$$

$$u_i \geq 0 \qquad \forall i = 1,\cdots,k. \tag{94f}$$

Where $i = 0$ represents the node of base station. $x_{i,j}$ is the binary variable to indicate whether there is a path between node i and j. $d_{i,j}$ is the distance between node i and node j. Constraint (94b) and (94c) make sure that there is only one path coming in or going out of one node. Constraint (94d) and (94f) eliminate the sub-tour.

Algorithm 1: Minimum Battery Level Anchor Nodes Selection Algorithm

Result: Anchor node set $\mathcal{A}$

Initialize maximum AUV traveling distance X;
Sort sensor nodes by battery level in ascending order;
Select top k nodes and calculate the shortest length $\chi(k)$ of AUV traveling path by solving the TSP problem (94);
while $(\chi(k) - X)(\chi(k+1) - X) > 0$ **do**
    if $\chi(k) > X$ **then**
        $k = k + 1$;
    else
        $k = k - 1$;
    end
    update $\chi(k), \chi(k+1)$;
end
Return $\mathcal{A} = \mathcal{A}_k$

5.3.2 Alternating Anchor Nodes Selection and Flow Routing (AANSFR)

Based on the previous analysis, we know that in order to determine the best data collection strategy, two problems, acoustic flow routing and optimal AUV travel path, need to be solved simultaneously. Generally speaking, these two problems are coupled together, which complicates the problem formulation. Previously, we use battery residue energy to decouple these two problems. However, under some circumstance, *e.g.*, when most of the sensor nodes have similar battery energy level, BPBANS may not yield the best anchor nodes selection result.

Recall Algorithm 1, we find that the key parameter for decoupling the flow routing problem and the anchor nodes selection problem is the number of anchor nodes k. Inspired by this, we come up with the AANSFR algorithm. We first preset the size of anchor node set $\mathcal{A}$. Then, determine the element of set $\mathcal{A}$. Third, calculate the shortest TSP path between anchor nodes in $\mathcal{A}$. Fourth, compare the calculated shortest path with the maximum travel path of AUV and determine whether to increase or decrease the size of $\mathcal{A}$ until the optimal $\mathcal{A}$ was found. The whole process is shown in Algorithm 2. Here, we introduce a binary variable x_j to indicate the anchor node selection. $x_j = 1$ means node j is selected as an anchor node. k is the preset total number of anchor nodes. m_i is the MI data flow of node

i. The best anchor nodes selection problem can be formulated as

$$\max \quad \min_{j\in\mathcal{N}} \ (E_j - \rho_j) \tag{95a}$$

$$\text{s.t.} \quad \sum_{j\in\mathcal{N}} f_{ij} = (1-x_i)(\sum_{k\in\mathcal{N}} f_{ki} + g_i) + x_i m_i \quad \forall i \in \mathcal{N}, \tag{95b}$$

$$\rho_j = (\mu_j x_j + \gamma_j) \sum_{i\in\mathcal{N}} f_{ij} + g_j \mu_j x_j + \sum_{k\in\mathcal{N}} f_{jk}\epsilon_{jk}, \tag{95c}$$

$$\rho_j \le E_j \qquad \forall j \in \mathcal{N}, \tag{95d}$$

$$x_i \in \{0,1\} \qquad \forall i \in \mathcal{N}, \tag{95e}$$

$$f_{ij} \ge 0 \qquad \forall i,j \in \mathcal{N}, \tag{95f}$$

$$\sum_{i\in\mathcal{N}} x_i = k. \tag{95g}$$

Besides the minimax objective function, there exist the product of a binary variable and a continuous variable $x_i f_{ij}$ and $x_i m_i$ in constraint (95b) and (95c), which need to be linearized before it can be solved by the optimization solver. The linearized form is

$$\max \quad z \tag{96a}$$

$$\text{s.t.} \quad m_i \ge 0 \qquad \forall i \in \mathcal{N}, \tag{96b}$$

$$m_i \le x_i C_{MI} \qquad \forall i \in \mathcal{N}, \tag{96c}$$

$$f_{ij} \ge 0 \qquad \forall i,j \in \mathcal{N}, \tag{96d}$$

$$f_{ij} \le C_{ij}(1-x_i) \qquad \forall i,j \in \mathcal{N}, \tag{96e}$$

$$\sum_{j\in\mathcal{N}} f_{ij} + m_i = \sum_{k\in\mathcal{N}} f_{ki} + g_i \qquad \forall i \in \mathcal{N}, \tag{96f}$$

$$\rho_j = \sum_{i\in\mathcal{N}} f_{ij}\gamma_{ij} + \mu x_j + \sum_{k\in\mathcal{N}} f_{jk}\epsilon_{jk} \quad \forall j \in \mathcal{N}, \tag{96g}$$

$$z \le E_j - \rho_j \qquad \forall j \in \mathcal{N}, \tag{96h}$$

$$x_i \in \{0,1\} \qquad \forall i \in \mathcal{N}, \tag{96i}$$

$$\sum_{i\in\mathcal{N}} x_i = k. \tag{96j}$$

Algorithm 2: Alternating Anchor Nodes Selection and Flow Routing (AANSFR)

Result: Anchor node set $\mathcal{A}$

Initialize maximum AUV traveling distance X;
Initialize minimum number of anchor nodes k;
Solve optimization problem (95) and obtain temporary anchor node set $\mathcal{A}_k$;
Based on $\mathcal{A}_k$ calculate the shortest length $\chi(k)$ of traveling path by solving the TSP problem (94);
while $\chi(k) < X$ **do**
    $k = k + 1$;
    repeat step 3 to update $\mathcal{A}_k$;
    repeat step 4 to update $\chi(k)$;
end
Return $\mathcal{A} = \mathcal{A}_k$

Where C_{MI} is the MI channel capacity and C_{ij} is the acoustic channel capacity between node i and node j.

5.4 Numerical Evaluation

5.4.1 Simulation Settings

We consider an underwater sensor network with 20 sensor nodes randomly deployed on the sea floor within a 2D area with dimensions of 1500 m $\times$ 1500 m as shown in Fig. 71. The depth of the sensor network is 150 m. Each sensor node is powered by a battery. An AUV is scheduled periodically (1h/round) to collect the data. Suppose the average speed of AUV is 1 m/s, so the maximum cruising range for each round is 3.6 km. The data generated in a period by each sensor nodes is randomly selected from 500 bytes to 2000 bytes. In Fig. 71 the red node is the surface base station (BS), blue integers indicate the sensor node number, and black integers are the data generation rate per round of different sensor nodes. Base on Equation (97), we can estimate the acoustic communication energy efficiency among different sensor nodes by

$$f(x) = ae^{bx}, \tag{97}$$

where, $a = 0.00054$, $b = 0.00067$, and x is the communication range in meter.

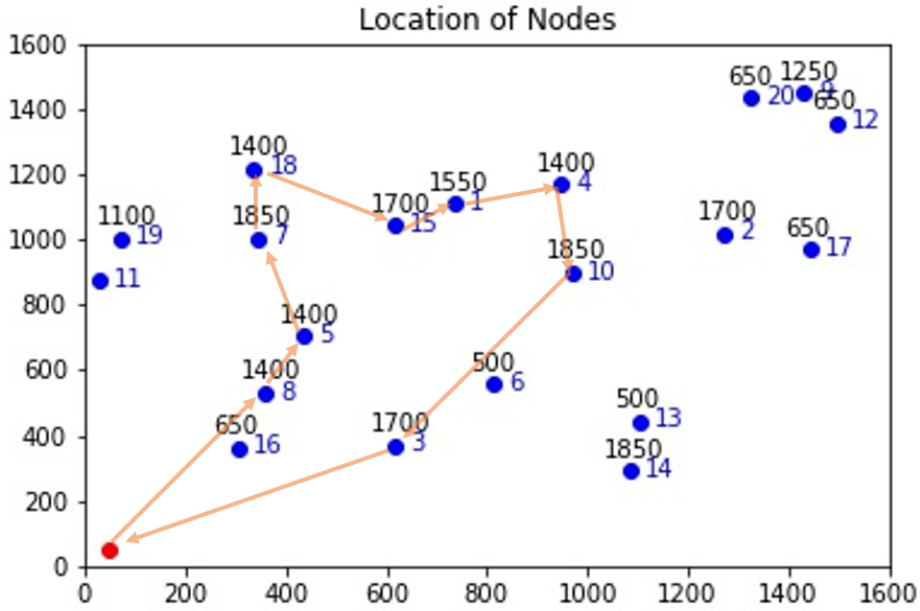

Figure 71: Network topology. The red dot is the surface base station. Blue dots are sensor nodes with node index on the right and sensing data rate (bytes/hour) above. The orange arrow is one of the possible AUV traveling path.

The network structure, including node locations, sensing data generation rate, transmission and reception power consumption, and battery residual energy, is implemented in Python. The constrained optimization problems (93, 94, and 96) can be solved by GUROBI (an optimization solver).

5.4.2 Simulation Results

Suppose all the batteries have the same initial battery capacity, randomly choose as 126 joules. Then we can estimate the network life time based on different data collection schemes. If all the sensor nodes directly communicate with surface base station through acoustic communications, the network life time will be determined by sensor node #2 considering the distance between sensor nodes and surface base station as well as sensing data generation rates. Specifically, node #2 needs the most significant power of 20 joules to transmit the collected data to the surface base station for 1 hour period. So the network

lifetime is no more than 6 hours.

However, if the sensing data was collected by the AUV with MI + acoustic hybrid networking the network life span can be significantly improved. Furthermore, the network life time is affected by the anchor nodes selection strategies. For BPBANS the life time is 14 hours while for AANSFR the life span is 18 hours. The anchor nodes selection results of these two algorithms are shown in Table 7. Neither algorithm BPBANS nor AANSFR can guarantee that the selected anchor nodes for every round is optimal. For example, for round 12 the anchor nodes selected by algorithm AANSFR are node 2 and node 14, however at least node 10 and node 16 can be included to further save the power. For practical applications, we can run both of the algorithm to select the anchor nodes for each round and choose the bigger anchor node set.

We can imagine that the network life span would be affected by the note location, surface base station location, and sensor data generation rates. So, to evaluate the performance of different anchor node selection schemes we alter the network parameters and the corresponding results are shown in Fig. 72. When the BS was located at the center of the network, we enlarge the network size to 2000 m $\times$ 2000 m just to limit the total number of selected anchor nodes. The simulation results show that under most of the situations algorithm AANSFR outperforms BPBANS. However, under some network settings algorithm BPBANS performs better (*e.g.*, case T2 in Fig. 72 (b)).

5.5 Summary

Using AUV for underwater data collection is a promising solution for underwater sensor networks, since it helps sensors to avoid transmitting data through long range acoustic communications which may deplete the battery very quickly. Furthermore, we can apply power efficient MI wireless communications between AUVs and sensor nodes to further save the energy. We have shown that the AUV assisted MI + acoustic hybrid networking can prolong the network lifespan for around 3 times compared with the traditional pure acoustic solution. To solve the problem of AUV path planing and optimal acoustic flow

Table 7: Anchor nodes selection statistics.

Round	BPBANS	AANSFR
1	7,10,14	7,1,10,14,3
2	8, 5, 1, 4, 2, 6, 3	2,5,15
3	19, 18, 1, 15, 7	16, 7, 18, 1, 10, 14
4	8, 5, 4, 6, 3	8, 4, 2, 3
5	3, 10	5, 7, 18, 15, 1, 10
6	7, 1, 13, 14, 3	8, 4, 2, 14, 3
7	1, 4, 2	7, 10
8	1, 10	5, 15, 10, 2, 14, 3
9	5, 7, 1, 4, 2, 3	7, 18, 1, 4, 8
10	6, 10, 13, 14	10, 2, 14
11	7, 1, 4, 5, 8	8, 5, 7, 18, 15, 1, 4, 10, 3
12	19, 18, 15, 1, 14	2, 14
13	4, 6, 3	7, 1, 10, 14, 3
14	7, 2, 3	5, 15, 2
15		7, 18, 1, 4, 10, 3
16		5, 15, 2, 14
17		8, 7, 18, 4, 10, 3
18		15, 1, 2, 14

routing, we use the number of selected anchor nodes to simplify the problem into two steps. Specifically, we first preset the number of anchor nodes and determined the corresponding optimal anchor nodes and the data flow of acoustic links. Then calculate the shortest path between anchor nodes. If the path is less than the maximum AUV traveling distance we increase the number of anchor nodes and iterate the process. Two dynamic anchor nodes selection strategies (BPBANS and AANSFR) are compared. Algorithm BPBANS selects the anchor nodes only based on the battery residue power, so it can run fast but may not guarantee the optimal solution. Algorithm AANSFR determine the optimal anchor nodes when the total number of anchor nodes is preset and yields longer network lifetime in most cases.

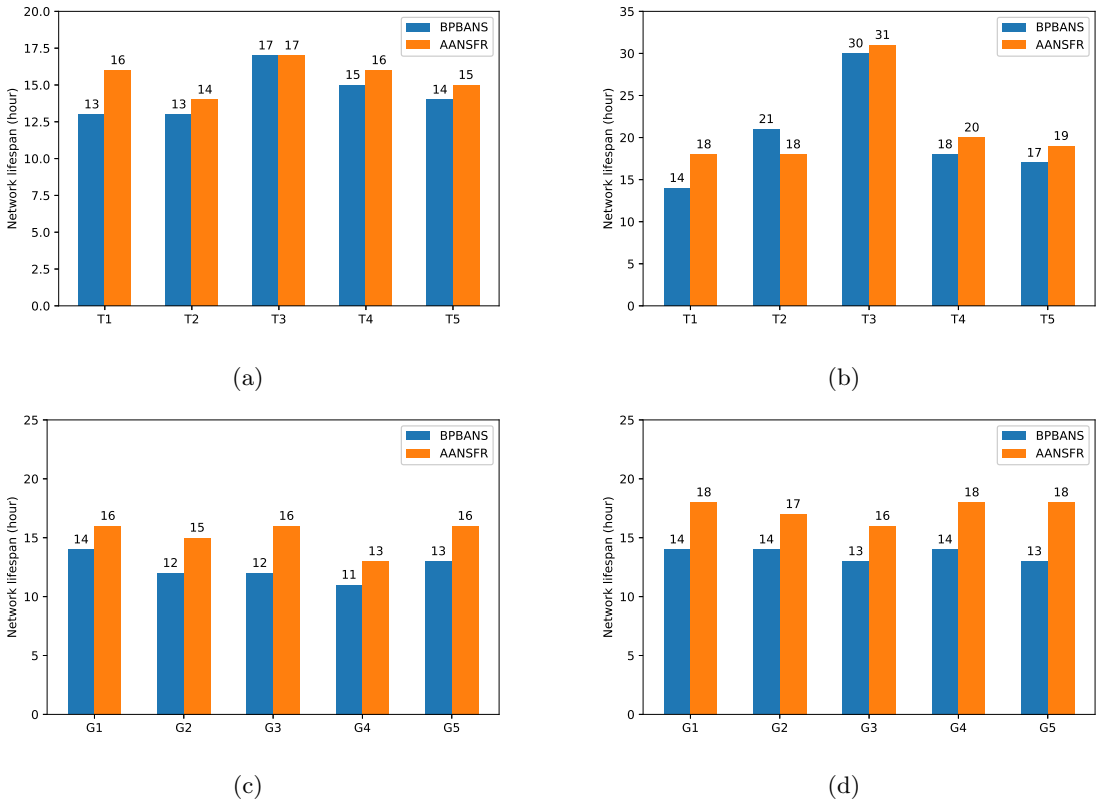

Figure 72: Network lifespan for different configurations.

6 Conclusions and Future Works

6.1 Conclusions

To overcome the drawbacks of underwater acoustic wireless communications and provide communication supports for various IoUT applications, two different kinds of underwater communication paradigms are investigated in this dissertation, namely underwater MI wireless communications and stress wave communications. MI is suitable for short range applications, especially for the scenario where AUVs are applied to access different underwater devices. Stress wave communications rely on offshore pipeline networks for data transmission. Thanks to the much more reliable stress wave channel conditions and much wider bandwidth, much better communication performances can be achieved compared with traditional underwater acoustic wireless communications.

MI wireless communications only rely on the near field component of magnetic fields to encapsulate the digital data. Due to the fast attenuation of EM waves in the conductive sea water, the effective communication range of underwater MI wireless communications is within 20 meters in the low frequency (LF) spectrum. The negligible propagation delay make it useful for the scenario where accurate synchronization is required. To apply the MI technology on an AUV, a ferrite assisted geometry-conformal coil antenna was proposed, which directly wrap the wire on the surface of an AUV such that the fluid dynamic body can be maintained. The MI channel response is sensitive to the distance between transmission and reception coil antennas which can be characterized by the coupling coefficient k. As the transmission distance increases k will decrease. When $k << \frac{1}{Q}$, Q is the quality factor of the coil antenna, the transmitter and receiver are loosely coupled. Otherwise, they are strongly coupled. For the loosely coupled MI communication system, the bandwidth is determined by Q, and k only affects the signal strength or pathloss. For strongly coupled situation, k will have strong impact to the system bandwidth due to the frequency-splitting phenomenon. To evaluate the underwater MI wireless communication performances, an underwater MI testbed was built based on USRP and SDR. An computational efficient synchronization

scheme was proposed to take advantage of the narrow bandwidth and deterministic MI channel response. An underwater MI link with data rate of 24 kbps and transmission power of 3 mW at the distance of 0.8 m was achieved in the lab.

Offshore pipelines will play more and more important roles in the IoUT applications. Because it not only requires regular health monitoring which will generate valuable sensing data that needed to be transmitted to the onshore base station. It can also serve as a signal propagation medium and provide a robust and fast stress wave channels for underwater communications. As shown in Section 4, the stress channel has negligible pathloss and deterministic channel responses. However, it suffer from multimode dispersion and reverberation distortion from both ends, which results in long delay spread. The zero forcing equalization as well as OFDM are adapted to tackle the ISI. The lab-scale experiments demonstrate that the received stress wave signal can be successful demodulated.

Different underwater communication technologies have their own advantages as well as drawbacks. Taking advantages of different communications to form a hybrid network is a promising solution to combat the harsh underwater environments. To enable the power efficient data collection for UWSNs and prolong the network lifetime, AUVs was introduced into the UWASN for data collection using MI wireless communications. The optimal AUV data collection strategy including anchor nodes selection, traveling path determination, and hybrid flow routing was formulated as a mix-integer linear programming problem. The number of anchor nodes is the key parameter to decouple the complex formulation. The proposed AANSFR algorithm can successfully solve the problem. The numerical evaluation shows that the network lifetime can be significantly improved (> 3 times) by the hybrid networking.

6.2 Future Works

Both MI wireless communications and wireless power transfer are based on the resonant coupling between two coils. Utilizing the existing MI communication system to perform

underwater wireless power transfer would be a potential solution that can resolve the underwater power limitation problem. For wireless power transfer the high Q coil would be preferred since power efficiency is determined by the Q value. However, for wireless communications, high Q also means narrow communication bandwidth. Therefore, how to design an intelligent coil antenna that can self-adapt to communication as well as power transfer requirements would be the first consideration.

Another interesting topic is the underwater acoustic cooperative beam-forming enabled by the underwater MI wireless communications. Thanks to the negligible propagation delay, accurate synchronization can be achieved among underwater devices such as an AUV swarm. Therefore, precise carrier phase control would be possible, which enables the acoustic cooperative beam-forming. The cooperative acoustic beam-forming will reduce the man-made acoustic noise pollution to the ocean environments. The key question is how to perform MI synchronization among many MI devices? Also, what is the minimum bandwidth requirement?

As an extension of the present work a full scale experiment implemented in an actual offshore pipeline is necessary to further validate the accuracy of the proposed stress wave channel model, and the effectiveness of the proposed PHY layer techniques. It should be based on the actual subsea field testing results to determined what kinds of the channel coding scheme should be adapted to improve the reliability. Especially, if the noise power of a running pipeline is small enough, the complex error correction channel coding might be unnecessary. How to evaluate the pipeline healthy conditions purely based on the stress wave channel information is also a very interesting and useful topic.

Bibliography

[1] Ahmed, N., Hoyt, J., Radchenko, A., Pommerenke, D., and Zheng, Y. R. A multi-coil magneto-inductive transceiver for low-cost wireless sensor networks. In *Underwater Communications and Networking (UComms), 2014* (2014), IEEE, pp. 1–5.

[2] Akyildiz, I. F., Pompili, D., and Melodia, T. Underwater acoustic sensor networks: research challenges. *Ad hoc networks 3*, 3 (2005), 257–279.

[3] Akyildiz, I. F., Wang, P., and Sun, Z. Realizing underwater communication through magnetic induction. *IEEE Communications Magazine 53*, 11 (2015), 42–48.

[4] Alippi, C., Camplani, R., Galperti, C., and Roveri, M. A robust, adaptive, solar-powered WSN framework for aquatic environmental monitoring. *IEEE Sensors Journal 11*, 1 (2010), 45–55.

[5] Alleyne, D., Pavlakovic, B., Lowe, M., and Cawley, P. Rapid, long range inspection of chemical plant pipework using guided waves. In *AIP conference proceedings* (2001), vol. 557, AIP, pp. 180–187.

[6] Anderson, C. M., and LaBelle, R. P. Update of comparative occurrence rates for offshore oil spills. *Spill Science & Technology Bulletin 6*, 5-6 (2000), 303–321.

[7] Bainbridge, S., Eggeling, D., and Page, G. Lessons from the field—two years of deploying operational wireless sensor networks on the great barrier reef. *Sensors 11*, 7 (2011), 6842–6855.

[8] Balanis, C. A. *Antenna theory: analysis and design*. John Wiley & Sons, 2016.

[9] Bansal, R. Near-field magnetic communication. *IEEE Antennas and Propagation Magazine 46*, 2 (2004), 114–115.

[10] Beaujean, P.-P., and LeBlanc, L. R. Adaptive array processing for high-speed acoustic communication in shallow water. *IEEE Journal of Oceanic Engineering 29*, 3 (2004), 807–823.

[11] Bocchini, P., Marzani, A., and Viola, E. Graphical user interface for guided acoustic waves. *Journal of Computing in Civil Engineering 25*, 3 (2010), 202–210.

[12] Casey, K., Lim, A., and Dozier, G. A sensor network architecture for tsunami detection and response. *International Journal of Distributed Sensor Networks 4*, 1 (2008), 27–42.

[13] Catipovic, J., Deffenbaugh, M., Freitag, L., and Frye, D. An acoustic telemetry system for deep ocean mooring data acquisition and control. In *Proceedings Oceans* (1989), vol. 3, IEEE, pp. 887–892.

[14] Cayirci, E., Tezcan, H., Dogan, Y., and Coskun, V. Wireless sensor networks for underwater survelliance systems. *Ad Hoc Networks 4*, 4 (2006), 431–446.

[15] Chitre, M. A high-frequency warm shallow water acoustic communications channel model and measurements. *The Journal of the Acoustical Society of America 122*, 5 (2007), 2580–2586.

[16] Davis, A., and Chang, H. Underwater wireless sensor networks. In *2012 Oceans* (2012), IEEE, pp. 1–5.

[17] Demirors, E., Sklivanitis, G., Santagati, G. E., Melodia, T., and Batalama, S. N. Design of a software-defined underwater acoustic modem with real-time physical layer adaptation capabilities. In *Proceedings of the international conference on underwater networks & systems* (2014), pp. 1–8.

[18] Desa, E., Madhan, R., and Maurya, P. Potential of autonomous underwater vehicles as new generation ocean data platforms. *Current science* (2006), 1202–1209.

[19] Diamant, R., Feuer, A., and Lampe, L. Choosing the right signal: Doppler shift estimation for underwater acoustic signals. In *Proceedings of the Seventh ACM International Conference on Underwater Networks and Systems* (2012), pp. 1–8.

[20] Dietrich, I., and Dressler, F. On the lifetime of wireless sensor networks. *ACM Transactions on Sensor Networks (TOSN) 5*, 1 (2009), 1–39.

[21] DNV, D. N. V. Recommended failure rates for pipelines. Tech. rep., Energy report, Det Norske Veritas DNV, 01 2010.

[22] Domingo, M. C. Magnetic induction for underwater wireless communication networks. *IEEE Transactions on Antennas and Propagation 60*, 6 (2012), 2929–2939.

[23] Domingo, M. C. An overview of the internet of underwater things. *Journal of Network and Computer Applications 35*, 6 (2012), 1879–1890.

[24] Drumheller, D. S. Acoustical properties of drill strings. *The Journal of the Acoustical Society of America 85*, 3 (1989), 1048–1064.

[25] Edelstein, K. Latest oil and gas incident in the Gulf of Mexico. `https://www.fractracker.org/2014/11/latest-incident-gulf-of-mexico/`, 2014. 2014-11-26.

[26] Gao, L., Gardner, W. R., Robbins, C., Johnson, D. H., and Memarzadeh, M. Limits on data communication along the drillstring using acoustic waves. *SPE Reservoir Evaluation & Engineering 11*, 01 (2008), 141–146.

[27] Ghoreyshi, S. M., Shahrabi, A., and Boutaleb, T. An efficient AUV-aided data collection in underwater sensor networks. In *2018 IEEE 32nd International Conference on advanced information networking and applications (AINA)* (2018), IEEE, pp. 281–288.

[28] Green, M. D., and Rice, J. A. Channel-tolerant FH-MFSK acoustic signaling for undersea communications and networks. *IEEE Journal of Oceanic Engineering 25*, 1 (2000), 28–39.

[29] Gulbahar, B. A communication theoretical analysis of multiple-access channel capacity in magneto-inductive wireless networks. *IEEE Transactions on Communications 65*, 6 (2017), 2594–2607.

[30] Gulbahar, B., and Akan, O. B. A communication theoretical modeling and analysis of underwater magneto-inductive wireless channels. *IEEE Transactions on Wireless Communications 11*, 9 (2012), 3326–3334.

[31] Guo, H., Sun, Z., and Wang, P. Channel modeling of MI underwater communication using tri-directional coil antenna. In *2015 IEEE Global Communications Conference (GLOBECOM)* (San Diego, CA, 2015), pp. 1–6.

[32] Guo, Y., and Liu, Y. Localization for anchor-free underwater sensor networks. *Computers & Electrical Engineering 39*, 6 (2013), 1812–1821.

[33] Gutierrez-Estevez, M. A., Krüger, U., Krueger, K. A., Manolakis, K., Jungnickel, V., Jaksch, K., Krueger, K., Mikulla, S., Giese, R., Sohmer, M., et al. Acoustic broadband communications over deep drill strings using adaptive OFDM. In *2013 IEEE Wireless Communications and Networking Conference (WCNC)* (2013), IEEE, pp. 4089–4094.

[34] He, S., Wang, N., Ho, M., Zhu, J., and Song, G. Design of a new stress wave communication method for underwater communication. *IEEE Transactions on Industrial Electronics* (2020), 1–1.

[35] Ho, M., El-Borgi, S., Patil, D., and Song, G. Inspection and monitoring systems subsea pipelines: A review paper. *Structural Health Monitoring 19*, 2 (2020), 606–645.

[36] Hoult, N., FIDLER, P., and Middleton, C. Wireless structural health monitoring of bridges: current challenges and future innovations. In *AUSTROADS BRIDGE CONFERENCE, 7TH, 2009, AUCKLAND, NEW ZEALAND* (2009).

[37] Huang, R., Zhang, B., Qiu, D., and Zhang, Y. Frequency splitting phenomena of magnetic resonant coupling wireless power transfer. *IEEE Transactions on Magnetics 50*, 11 (2014), 1–4.

[38] Ilyas, N., Alghamdi, T. A., Farooq, M. N., Mehboob, B., Sadiq, A. H., Qasim, U., Khan, Z. A., and Javaid, N. Aedg: AUV-aided efficient data gathering routing protocol for underwater wireless sensor networks. *Procedia Computer Science 52* (2015), 568–575.

[39] Ji, Q., Ding, Z., Wang, N., Pan, M., and Song, G. A novel waveform optimization scheme for piezoelectric sensors wire-free charging in the tightly insulated environment. *IEEE Internet of Things Journal 5*, 3 (2018), 1936–1946.

[40] Ji, Q., Ho, M., Zheng, R., Ding, Z., and Song, G. An exploratory study of stress wave communication in concrete structures. *Smart Structures and Systems 15*, 1 (2015), 135–150.

[41] Jia, Z.-g., Ren, L., Li, H.-n., Ho, S.-C., and Song, G.-b. Experimental study of pipeline leak detection based on hoop strain measurement. *Structural Control and Health Monitoring 22*, 5 (2015), 799–812.

[42] Jiang, T., Kong, Q., Patil, D., Luo, Z., Huo, L., and Song, G. Detection of debonding between fiber reinforced polymer bar and concrete structure using piezoceramic transducers and wavelet packet analysis. *IEEE Sensors Journal 17*, 7 (2017), 1992–1998.

[43] Jimenez, E., Quintana, G., Mena, P., Dorta, P., Perez-Alvarez, I., Zazo, S., Perez, M., and Quevedo, E. Investigation on radio wave propagation in

shallow seawater: Simulations and measurements. In *Underwater Communications and Networking Conference (UComms), 2016 IEEE Third* (2016), IEEE, pp. 1–5.

[44] Johnson, C. C. A seismic communications investigation employing a piezoelectric transducer. Tech. rep., SOUTHWEST RESEARCH INST SAN ANTONIO TX, 1972.

[45] Johny, J., Prabhu, R., Fung, W. K., and Watson, J. Investigation of positioning of FBG sensors for smart monitoring of oil and gas subsea structures. In *OCEANS 2016-Shanghai* (2016), IEEE, pp. 1–4.

[46] Kailaswar, S., Zheng, R., Kovitz, J., Phung, Q., Wang, H., Ding, Z., and Song, G. Concretecom: A new communication paradigm for building structural health monitoring. In *Proceedings of the Fourth ACM Workshop on Embedded Sensing Systems for Energy-Efficiency in Buildings* (2012), ACM, pp. 131–137.

[47] Kaiser, M. J. Offshore pipeline construction cost in the US Gulf of Mexico. *Marine Policy 82* (2017), 147–166.

[48] Kao, C.-C., Lin, Y.-S., Wu, G.-D., and Huang, C.-J. A comprehensive study on the internet of underwater things: applications, challenges, and channel models. *Sensors 17*, 7 (2017), 1477.

[49] Khaledi, S., Mann, H., Perkovich, J., and Zayed, S. Design of an underwater mine detection system. In *2014 Systems and Information Engineering Design Symposium (SIEDS)* (2014), IEEE, pp. 78–83.

[50] Khan, A., and Jenkins, L. Undersea wireless sensor network for ocean pollution prevention. In *2008 3rd International Conference on Communication Systems Software and Middleware and Workshops (COMSWARE'08)* (2008), IEEE, pp. 2–8.

[51] Khan, J. U., and Cho, H.-S. A distributed data-gathering protocol using AUV in underwater sensor networks. *Sensors 15*, 8 (2015), 19331–19350.

[52] Khan, M. T. R., Ahmed, S. H., and Kim, D. AUV-aided energy-efficient clustering in the internet of underwater things. *IEEE Transactions on Green Communications and Networking 3*, 4 (2019), 1132–1141.

[53] Kong, Q., Robert, R. H., Silva, P., and Mo, Y. Cyclic crack monitoring of a reinforced concrete column under simulated pseudo-dynamic loading using piezoceramic-based smart aggregates. *Applied sciences 6*, 11 (2016), 341.

[54] Kumar, P., Kumar, P., Priyadarshini, P., et al. Underwater acoustic sensor network for early warning generation. In *2012 Oceans* (2012), IEEE, pp. 1–6.

[55] Kurs, A., Karalis, A., Moffatt, R., Joannopoulos, J. D., Fisher, P., and Soljačić, M. Wireless power transfer via strongly coupled magnetic resonances. *science 317*, 5834 (2007), 83–86.

[56] Lawry, T. J., Saulnier, G. J., Ashdown, J. D., Wilt, K. R., Scarton, H. A., Pascarelle, S., and Pinezich, J. D. Penetration-free system for transmission of data and power through solid metal barriers. In *2011-MILCOM 2011 Military Communications Conference* (2011), IEEE, pp. 389–395.

[57] Lee, H. K., and Lee, B. M. An underwater acoustic channel modeling for internet of things networks. *Wireless Personal Communications 116*, 3 (2021), 2697–2722.

[58] Lee, K., and Cho, D.-H. Maximizing the capacity of magnetic induction communication for embedded sensor networks in strongly and loosely coupled regions. *IEEE Transactions on Magnetics 49*, 9 (2013), 5055–5062.

[59] Leinov, E., Lowe, M. J., and Cawley, P. Ultrasonic isolation of buried pipes. *Journal of Sound and Vibration 363* (2016), 225–239.

[60] Li, B., Zhou, S., Stojanovic, M., Freitag, L., and Willett, P. Multicarrier communication over underwater acoustic channels with nonuniform doppler shifts. *IEEE Journal of Oceanic Engineering 33*, 2 (2008), 198–209.

[61] Li, P., Gu, H., Song, G., Zheng, R., and Mo, Y. Concrete structural health monitoring using piezoceramic-based wireless sensor networks. *Smart Structures and Systems 6*, 5_6 (2010), 731–748.

[62] Ma, D., Shi, Y., Zhang, W., and Liu, G. Design of acoustic transmission along drill strings for logging while drilling data based on adaptive NC-OFDM. *AEU-International Journal of Electronics and Communications 83* (2018), 329–338.

[63] Magalhaes, F. A. d., Vannozzi, G., Gatta, G., and Fantozzi, S. Wearable inertial sensors in swimming motion analysis: a systematic review. *Journal of sports sciences 33*, 7 (2015), 732–745.

[64] Manjula, R., and Manvi, S. S. Coverage optimization based sensor deployment by using PSO for anti-submarine detection in UWASNs. In *2013 Ocean Electronics (SYMPOL)* (2013), IEEE, pp. 15–22.

[65] Marin-Perez, R., García-Pintado, J., and Gómez, A. S. A real-time measurement system for long-life flood monitoring and warning applications. *Sensors 12*, 4 (2012), 4213–4236.

[66] Mayer, L. A. Frontiers in seafloor mapping and visualization. *Marine Geophysical Researches 27*, 1 (2006), 7–17.

[67] Melodia, T., Kulhandjian, H., Kuo, L.-C., and Demirors, E. Advances in underwater acoustic networking. *Mobile ad hoc networking: Cutting edge directions* (2013), 804–852.

[68] Memarzadeh, M. *Optimal borehole communication using multicarrier modulation.* PhD thesis, 2007.

[69] Menon, K. U., Divya, P., and Ramesh, M. V. Wireless sensor network for river water quality monitoring in india. In *2012 Third International Conference on Computing, Communication and Networking Technologies (ICCCNT'12)* (2012), IEEE, pp. 1–7.

[70] Neasham, J. A., Goodfellow, G., and Sharphouse, R. Development of the "seatrac" miniature acoustic modem and usbl positioning units for subsea robotics and diver applications. In *OCEANS 2015-Genova* (2015), IEEE, pp. 1–8.

[71] Nguyen, H., Agbinya, J. I., and Devlin, J. FPGA-based implementation of multiple modes in near field inductive communication using frequency splitting and MIMO configuration. *IEEE Transactions on Circuits and Systems I: Regular Papers 62*, 1 (2015), 302–310.

[72] OECD. *The Ocean Economy in 2030*. OECD Publishing, Paris, 2016.

[73] Otnes, R., and Eggen, T. H. Underwater acoustic communications: long-term test of turbo equalization in shallow water. *IEEE Journal of Oceanic engineering 33*, 3 (2008), 321–334.

[74] Pal, A., and Kant, K. Nfmi: Connectivity for short-range IoT applications. *Computer 52*, 2 (2019), 63–67.

[75] Pallardy, R. Deepwater horizon oil spill. `https://www.britannica.com/event/Deepwater-Horizon-oil-spill`, 2010. 2010-04-21.

[76] Pozar, D. M. *Microwave engineering*, 4th ed. John Wiley & Sons, 2011.

[77] Qarabaqi, P., and Stojanovic, M. Statistical characterization and computationally efficient modeling of a class of underwater acoustic communication channels. *IEEE Journal of Oceanic Engineering 38*, 4 (2013), 701–717.

[78] Rauchenstein, L. T., Vishnu, A., Li, X., and Deng, Z. D. Improving underwater localization accuracy with machine learning. *Review of Scientific Instruments 89*, 7 (2018), 074902.

[79] Rice, M. *Digital communications: a discrete-time approach*. Prentice Hall, 2009.

[80] Rose, J. L. *Ultrasonic guided waves in solid media*. Cambridge university press, 2014.

[81] Saeed, H., Ali, S., Rashid, S., Qaisar, S., and Felemban, E. Reliable monitoring of oil and gas pipelines using wireless sensor network (WSN)—REMONG. In *2014 9th International Conference on System of Systems Engineering (SOSE)* (2014), IEEE, pp. 230–235.

[82] Scussel, K. F., Rice, J. A., and Merriam, S. A new MFSK acoustic modem for operation in adverse underwater channels. In *Oceans' 97. MTS/IEEE Conference Proceedings* (1997), vol. 1, IEEE, pp. 247–254.

[83] Shamonina, E., Kalinin, V., Ringhofer, K., and Solymar, L. Magneto-inductive waveguide. *Electronics letters 38*, 8 (2002), 371–373.

[84] Sharif, B. S., Neasham, J., Hinton, O. R., and Adams, A. E. A computationally efficient doppler compensation system for underwater acoustic communications. *IEEE Journal of oceanic engineering 25*, 1 (2000), 52–61.

[85] Sheard, M. Field experience of using long-range ultrasonic testing. *Insight 43*, 2 (2001), 73–83.

[86] Sherlock, B., Neasham, J. A., and Tsimenidis, C. C. Implementation of a spread-spectrum acoustic modem on an android mobile device. In *OCEANS 2017-Aberdeen* (2017), IEEE, pp. 1–9.

[87] Sherlock, B., Neasham, J. A., and Tsimenidis, C. C. Spread-spectrum techniques for bio-friendly underwater acoustic communications. *IEEE Access 6* (2018), 4506–4520.

[88] Sifferlen, J. F., Song, H., Hodgkiss, W. S., Kuperman, W., and Stevenson, J. M. An iterative equalization and decoding approach for underwater acoustic communication. *IEEE Journal of Oceanic Engineering 33*, 2 (2008), 182–197.

[89] Singh, S., Webster, S. E., Freitag, L., Whitcomb, L. L., Ball, K., Bailey, J., and Taylor, C. Acoustic communication performance of the whoi micro-modem

in sea trials of the nereus vehicle to 11,000 m depth. In *OCEANS 2009* (2009), IEEE, pp. 1–6.

[90] Siu, S., Ji, Q., Wu, W., Song, G., and Ding, Z. Stress wave communication in concrete: I. characterization of a smart aggregate based concrete channel. *Smart Materials and Structures 23*, 12 (2014), 125030.

[91] Siu, S., Qing, J., Wang, K., Song, G., and Ding, Z. Stress wave communication in concrete: Ii. evaluation of low voltage concrete stress wave communications utilizing spectrally efficient modulation schemes with PZT transducers. *Smart materials and structures 23*, 12 (2014), 125031.

[92] Socheleau, F.-X., Laot, C., and Passerieux, J.-M. Stochastic replay of non-wssus underwater acoustic communication channels recorded at sea. *IEEE Transactions on Signal Processing 59*, 10 (2011), 4838–4849.

[93] Srinivas, S., Ranjitha, P., Ramya, R., and Narendra, G. K. Investigation of oceanic environment using large-scale UWSN and UANETs. In *2012 8th International Conference on Wireless Communications, Networking and Mobile Computing* (2012), IEEE, pp. 1–5.

[94] Stojanovic, M. Underwater acoustic communication.

[95] Stojanovic, M. *Low complexity OFDM detector for underwater acoustic channels*. IEEE, 2006.

[96] Stojanovic, M., and Preisig, J. Underwater acoustic communication channels: Propagation models and statistical characterization. *IEEE communications magazine 47*, 1 (2009), 84–89.

[97] Sun, Z., and Akyildiz, I. F. Magnetic induction communications for wireless underground sensor networks. *IEEE Transactions on Antennas and Propagation 58*, 7 (2010), 2426–2435.

[98] Sun, Z., and Akyildiz, I. F. On capacity of magnetic induction-based wireless underground sensor networks. In *2012 Proceedings IEEE INFOCOM* (2012), IEEE, pp. 370–378.

[99] Suzuki, M., Sasaki, T., and Tsuchiya, T. Digital acoustic image transmission system for deep-sea research submersible. In *OCEANS 92 Proceedings@ m_Mastering the Oceans Through Technology* (1992), vol. 2, IEEE, pp. 567–570.

[100] Tao, J., Wu, Y., Han, X., and Pelekanakis, K. Sparse direct adaptive equalization for single-carrier mimo underwater acoustic communications. *IEEE Journal of Oceanic Engineering 45*, 4 (2019), 1622–1631.

[101] Tomasi, B., Zappa, G., McCoy, K., Casari, P., and Zorzi, M. Experimental study of the space-time properties of acoustic channels for underwater communications. In *OCEANS'10 IEEE SYDNEY* (2010), IEEE, pp. 1–9.

[102] Urick, R. J. Principles of underwater sound-2.

[103] Vázquez Carazo, A. *Novel piezoelectric transducers for high voltage measurements.* Universitat Politècnica de Catalunya, 2000.

[104] Waldmeyer, M., Tan, H.-P., and Seah, W. K. Multi-stage AUV-aided localization for underwater wireless sensor networks. In *2011 IEEE Workshops of International Conference on Advanced Information Networking and Applications* (2011), IEEE, pp. 908–913.

[105] Wan, L., Wang, Z., Zhou, S., Yang, T., and Shi, Z. Performance comparison of doppler scale estimation methods for underwater acoustic OFDM. *Journal of Electrical and Computer Engineering 2012* (2012).

[106] Wang, X., Wei, D., Wei, X., Cui, J., and Pan, M. Has4: A heuristic adaptive sink sensor set selection for underwater AUV-aid data gathering algorithm. *Sensors 18*, 12 (2018), 4110.

[107] Wang, Y., Dobbin, A., and Bousquet, J.-F. A compact low-power underwater magneto-inductive modem. In *Proceedings of the 11th ACM International Conference on Underwater Networks & Systems* (2016), ACM, p. 14.

[108] Wei, D., Soto, S. S., Garcia, J., Becker, A. T., Wang, L., and Pan, M. ROV assisted magnetic induction communication field tests in underwater environments. In *Proceedings of the Thirteenth ACM International Conference on Underwater Networks & Systems* (Shenzhen, China, 2018), p. 20.

[109] Wei, D., Yan, L., Huang, C., Wang, J., Chen, J., Pan, M., and Fang, Y. Dynamic magnetic induction wireless communications for autonomous-underwater-vehicle-assisted underwater IoT. *IEEE Internet of Things Journal 7*, 10 (2020), 9834–9845.

[110] Wu, A., He, S., Ren, Y., Wang, N., Ho, S. C. M., and Song, G. Design of a new stress wave-based pulse position modulation (ppm) communication system with piezoceramic transducers. *Sensors 19*, 3 (2019), 558.

[111] Wynn, R. B., Huvenne, V. A., Le Bas, T. P., Murton, B. J., Connelly, D. P., Bett, B. J., Ruhl, H. A., Morris, K. J., Peakall, J., Parsons, D. R., et al. Autonomous underwater vehicles (AUVs): Their past, present and future contributions to the advancement of marine geoscience. *Marine Geology 352* (2014), 451–468.

[112] Xin, X., Jackson, D. R., and Chen, J. Wireless power transfer along oil pipe using ferrite materials. *IEEE Transactions on Magnetics 53*, 3 (2017), 1–5.

[113] Xu, Y., Luo, M., Liu, Q., Du, G., and Song, G. PZT transducer array enabled pipeline defect locating based on time-reversal method and matching pursuit de-noising. *Smart Materials and Structures 28*, 7 (2019), 075019.

[114] Yan, H., Wan, L., Zhou, S., Shi, Z., Cui, J.-H., Huang, J., and Zhou, H. Dsp based receiver implementation for OFDM acoustic modems. *Physical Communication 5*, 1 (2012), 22–32.

[115] Yang, J., Wen, J., Wang, Y., Jiang, B., Wang, H., and Song, H. Fog-based marine environmental information monitoring toward ocean of things. *IEEE Internet of Things Journal 7*, 5 (2019), 4238–4247.

[116] Yang, W.-B., and Yang, T. High-frequency channel characterization for m-ary frequency-shift-keying underwater acoustic communications. *The Journal of the Acoustical Society of America 120*, 5 (2006), 2615–2626.

[117] Yoon, S., Azad, A. K., Oh, H., and Kim, S. Aurp: An AUV-aided underwater routing protocol for underwater acoustic sensor networks. *Sensors 12*, 2 (2012), 1827–1845.

[118] Zhang, J., Guan, X. D., Sun, Y., and Wei, X. J. Study on oil pipeline leakage detection based on stress wave detection technique and wavelet analysis. In *Advanced Materials Research* (2013), vol. 694, Trans Tech Publ, pp. 1368–1371.

[119] Zhu, J., Ren, L., Ho, S.-C., Jia, Z., and Song, G. Gas pipeline leakage detection based on PZT sensors. *Smart Materials and Structures 26*, 2 (2017), 25022.

[120] Zhuo, X., Liu, M., Wei, Y., Yu, G., Qu, F., and Sun, R. AUV-aided energy-efficient data collection in underwater acoustic sensor networks. *IEEE Internet of Things Journal 7*, 10 (2020), 10010–10022.